PROTECTIVE BARRIER COATINGS BETWEEN CATALYSTS AND CERAMIC SUPPORT STRUCTURES

by

Aida Kazagic

Thesis submitted for the degree

MASTER OF SCIENCE

MATERIALS, ENERGY AND NANOTECHNOLOGY

The Faculty of Mathematics and Natural Sciences

University of Oslo

June 2013

Preface

This thesis is written as a part of the master's degree in Materials, Energy and Nanotechnology at the Department of Physics, University of Oslo and is a collaboration between the Structure Physics research group and Yara International. The experimental work is carried out at the Centre for Materials Science and Nanotechnology and Yara Technology Centre in the period June 2012 - May 2013.

Completing this thesis and with that my master's degree represents a milestone in my life. I had a strong desire to write a thesis for an industrial company. I am very grateful that Alarga gave me this opportunity. I want to thank my supervisors Annette E. Gunnæs and David Waller for always patiently helping me when needed. I also want to thank other members of both research groups for showing interest for my work and for helping me out with various instruments. This especially includes Ole Bjørn Karlsen, Stefano Rubino, Annette Thøgersen, Marianne Grønvold and Nibal Sahli. On the social side I want to thank Helle Berg Bjørsom for making the working environment as pleasant as possible.

I want to thank my parents Alma and Nedžad Kazagić and my grandparents Hikmeta and Mirko Škrba for their support and for always encouraging me to do my best and my brother Sanjin Kazagić for dragging me out of the office for an occasional cup of coffee.

Last, but not least, the biggest thank goes to my dear Kristine for being such a wonderful person. Thank you for motivating me when my inspiration was low, for listening to my often unfounded concerns and tolerating long working hours for two years.

<div align="right">Aida Kazagić, Oslo, June 2013</div>

Abstract

N_2O is both a greenhouse gas and an ozone-depleting substance. Anthropogenic emissions in the chemical industry apply to adipic and nitric acid plants. Efforts are being made in order to reduce emission of N_2O from nitric acid plants by catalytic decomposition of N_2O. The catalysts are often supported and undesirable reactions at the catalyst-support interface occur under high temperature conditions. A barrier layer that physically separates and prevents/minimises the catalyst-support reactions may be deposited. Knowledge on which type of reactions occur at the interface can aid the selection of a barrier layer material.

In this work two de-N_2O catalysts were synthesised. The target catalyst phases were a $Co_{3-x}Mn_xO_4$ spinel and a $LaMnO_3$ perovskite catalyst. The $Co_{3-x}Mn_xO_4$ catalyst was synthesised by the coprecipitation method while the $LaMnO_3$ was synthesised by the sol-gel method. XRD of the catalyst powder synthesised by coprecipitation showed that two phases were formed, a cobalt rich phase $Co_{3-x}Mn_xO_4$, with cubic crystal lattice assigned by the space group $Fd\bar{3}m$ and a manganese rich phase $Mn_{3-x}Co_xO_4$, with a body-centered tetragonal crystal lattice with space group I41/amd. For simplicity, the powder is assigned as Co-Mn-O which is meant to indicate that more than one phase is present. XRD of the catalyst powder prepared by the sol-gel method showed that the phase $La_{0.969}Mn_{0.93}O_3$ had formed with a rhombohedral crystal lattice, space group $R\bar{3}c$ and cell parameters a = 5.5222A and c = 13.3317A.

Planar single crystals of aluminium oxide, α-Al_2O_3, and yttrium stabilised zirconia, YSZ, were chosen as supports for the two catalysts. Prior to catalyst deposition a reference layer of small platinum particles was deposited onto the single crystals to mark the original catalyst-support interface. This was achieved by depositing a 5nm platinum film by sputtering and sintering the film for 4h at 770°C. Catalyst inks were made and painted onto two single crystals of each support type. The samples were annealed at high temperature to simulate high temperature process conditions in a nitric acid plant. The samples painted with the Co-Mn-O ink were annealed at 1150°C for 75h, while the samples painted with the $La_{0.969}Mn_{0.93}O_3$ ink were annealed at 1500°C for 24h. After annealing, the catalyst-support interface was studied by SEM, XRD and TEM.

The phases formed at the $La_{0.969}Mn_{0.93}O_3$/α-Al_2O_3 interface were found to be $LaMnAl_{11}O_{19}$ with a hexagonal crystal lattice, space group P63/mmc and cell parameters a = 5.574A and c = 22.008A, and possibly also a modified perovskite of the form

$LaAl_{1-x}Mn_xO_3$ with a rhombohedral crystal lattice and space group R3m. The platinum reference layer could not be identified in the SEM, probably due to poor contrast between Pt and La. EDS measurements at two boundary positions, one close to the pure α-Al_2O_3 support and one close to the catalyst surface, show that there is diffusion of La and Mn into the α-Al_2O_3 support and diffusion of Al into the catalyst. The thickness of the $La_{0.969}Mn_{0.93}O_3/\alpha$-$Al_2O_3$ interface layer is estimated to $\approx$50-100μm.

The phase formed at the Co-Mn-O/α-Al_2O_3 interface was found to be a cobalt substituted $(Mn_{0.89}Al_{0.11})Al_2O_4$ with a cubic crystal lattice, Fd$\bar{3}$m space group and cell parameter a = 8.181A. EDS measurements on both sides of the reference layer show that there is a diffusion of Co and Mn into the α-Al_2O_3 support as well as diffusion of Al into the catalyst. The thickness of the Co-Mn-O/α-Al_2O_3 interface layer is estimated to $\approx$5-8μm.

A barrier layer between a catalyst and a support can be deposited by dip-coating the support into a dispersion containing barrier layer particles if the support and the barrier layer particles have opposite charges. Preliminary work on the deposition of a barrier layer between the support and the catalyst is also included in this work. The particle size should be in the nanometer range in order to avoid sedimentation during zeta potential measurements. α-Al_2O_3 particles have been downsized to 256nm and it is shown that particle agglomeration can be avoided if the pH of the dispersion is lowered to approximately 2.3. During downsizing the BET surface area increased from 5.18m^2/g to 30.4m^2/g.

Contents

CONTENTS

Chapter 1

Introduction

1.1 Motivation

In later years greater demands have been set on food production from agriculture due to the worlds growing population. Use of inorganic fertilizers can help farmers meet those needs through increased soil fertility. Nitric acid, HNO_3, is a common component in the production of inorganic fertilizers, where nitrous oxide, N_2O, is a byproduct. For a long time nitrous oxide was considered to be a relatively harmless species and was, for that reason, of little interest to scientists, engineers and politicians. The environmental impact of N_2O has, however, proven to be highly underestimated. Nitrous oxide is both a greenhouse gas and an ozone depleting gas. Global anthropogenic emission of greenhouse gases have increased with over 70% in the period 1970-2005 [1]. As a consequence, the surface temperature has increased with $0.74°C$ over the last 100 years. It is believed that this has had a negative impact on both the climate on Earth as well as the ecosystems. As an ozone-depleting substance, N_2O has many similarities with the CFCs [2]. Ravinshakara *et al.* have shown that the N_2O emissions are the largest of all the ozone-depleting substances and are projected to be the largest for the rest of the 21st century.

N_2O has both natural and anthropogenic sources. Table 1.1 gives an overview of the distribution of anthropogenic emissions of N_2O in the EU averaged for the period 1990-1998. Within human activities agriculture, through soil cultivation and the use of nitrogen-fertilizers, contributed to 57% of the total emission in the EU. Chemical

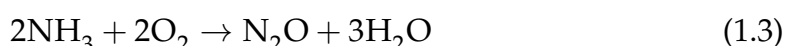| Sector	Relative emission
Agriculture	57%
Chemical industry	29%
Transport	5%
Energy industry	4%
Waste	1%
Other	4%

Table 1.1: The distribution of anthropogenic emission of N_2O in the EU avaraged for the period 1990-1998. Emissions from the chemical industry mainly applies to adipic acid and nitric acid plants. "Other" includes emission of HFCs, PFCs and SF_6. [3]

industries contributed with 29%. This emission mainly applies to adipic acid and nitric acid plants. Efforts are being made to reduce the emission of N_2O from nitric acid plants. This can be achieved by catalytic decomposition of N_2O to N_2 and O_2, but since the catalysts often are supported and used under high temperature conditions, undesirable reactions occur between the catalyst and the support. The focus of this work is to investigate the reactions that take place between two different catalysts and two different support materials under high temperature conditions. In the following, the production of nitric acid along with possible abatement options will be described in more detail. A more detailed project motivation will also be presented at the end of the chapter.

1.2 Nitric acid production

Nitric acid is one of the key elements in the production of inorganic fertilizers. The production of weak nitric acid (concentration of 50-65%) is based on the Ostwald process and consists of the following chemical operations [3, 4] :

1. Catalytic oxidation (combustion) of ammonia with air into nitric oxide.

$$NH_3 + 5O_2 \rightarrow 4NO + 6H_2O \tag{1.1}$$

$$4NH_3 + 3O_2 \rightarrow 2N_2 + 6H_2O \tag{1.2}$$

$$2NH_3 + 2O_2 \rightarrow N_2O + 3H_2O \tag{1.3}$$
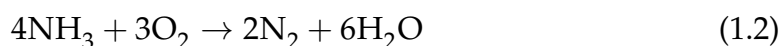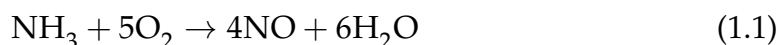
2. Oxidation of nitric oxide into nitrogen dioxide.

$$2NO + O_2 \rightarrow 2NO_2 \tag{1.4}$$

3. Absorption of nitrogen dioxide in water to produce nitric acid.

$$3NO_2 + H_2O \rightarrow 2HNO_3 + NO \tag{1.5}$$
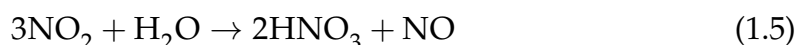
Catalytic oxidation of ammonia in air gives three possible reactions, reaction (1.1), (1.2) and (1.3). Reaction (1.1) leading to the formation of NO is the wanted reaction. However, reaction (1.2) leading to the formation of N_2 is thermodynamically the most favourable [3]. This means that without a catalyst, combustion of ammonia would exclusively lead to the formation of N_2. In industry, platinum-rhodium gauzes are used to catalyze reaction (1.1). In the presence of a catalyst the yields of N-products

with different oxidation degrees (N_2, N_2O and NO) can be controlled by controlling the temperature [3]. At low temperatures (423-473K), N_2 is the only N-containing product. The formation of the desired product, NO, starts at 573K and its yield continuously increases with increasing temperature. At higher temperatures N_2O formation starts, with a maximum at 675K.

Under optimized industrial conditions NO yields of 93-98 % can be achieved depending on the pressure and temperature. N_2 yield is in the range of 2-6% and N_2O yield is of about 1-2 % [5].

1.3 N_2O abatement options during nitric acid production

N_2O abatement systems are implemented in nitric acid plants in order to reduce the emission of N_2O. There are several different measures that can be taken into account. Figure 1.1 illustrates a simplified flowsheet of a nitric acid plant, with the position of different N_2O abatement options. The industry, research institutes and universities have identified four different abatement systems according to the position in the process [3]:

1. *Primary abatement* aims at removing N_2O that is formed in the ammonia burner.

2. *Secondary abatement* aims at removing N_2O directly under the ammonia oxidation catalyst.

3. *Tertiary abatement* aims at removing N_2O from the tail-gas leaving the absorption column prior to the expander.

4. *Quaternary abatement* aims at removing N_2O from the tail-gas after the expander.

The catalyst-support reactions studied in this work are a part of the secondary abatement system. However, in order to put the work in a proper context both primary and secondary abatement options are explained in detail in further sections. A more detailed review of all the abatement options is described in "Formation and control of N_2O in nitric acid production: Where do we stand today?" by Perez-Ramirez *et al* [3].

1.3.1   Primary abatement

During primary abatement either the catalytic oxidation of NH_3 can be optimized in terms of reactor design and operation or a more selective combustion catalyst can be

Figure 1.1: A simplified flowsheet of a nitric acid plant. The position of different abatement options are indicated as well as the formation route of HNO$_3$. Dotted lines indicate that there are further steps in the process that are not shown on this figure.

installed. In industry, platinum-rhodium-gauzes (Pt-Rh-gauzes) are used as unsupported combustion catalysts (see section 2.4 for an explanation of unsupported and supported catalysts). The Pt-Rh-gauzes can be knitted or woven and have several types of geometries. The type of geometry depends on the pressure regime utilized at the plant. High pressure plants operate at pressures higher than 8 bar, medium pressure plants operate at pressures between 3-8 bars, while atmospheric pressure plants operate at 1 bar. Usually, the gauze-pack consists of fewer gauzes and finer wire when installed in low and medium pressure plants and more gauzes and thicker wire when installed in high pressure plants. Figure 1.2 on the facing page shows two gauze-packs offered by the company Umicore. The figure on the left illustrates a gauze-pack used in low and medium pressure plants, while the figure on the right illustrates the gauze-pack used in high pressure plants.

The operating temperatures in the industry are often in the range of 1023-1123K. The platinum vaporization from the gauzes is substantial in this temperature range leading to a loss of activity and selectivity by thermal degradation and consequently reducing the NO yield and increasing the N$_2$O yield. The Pt-Rh-gauzes should therefore be replaced regularly to keep an optimum performance. The rate at which the gauzes should be replaced is dependent on the temperature and pressure used for ammonia conversion at the plant.
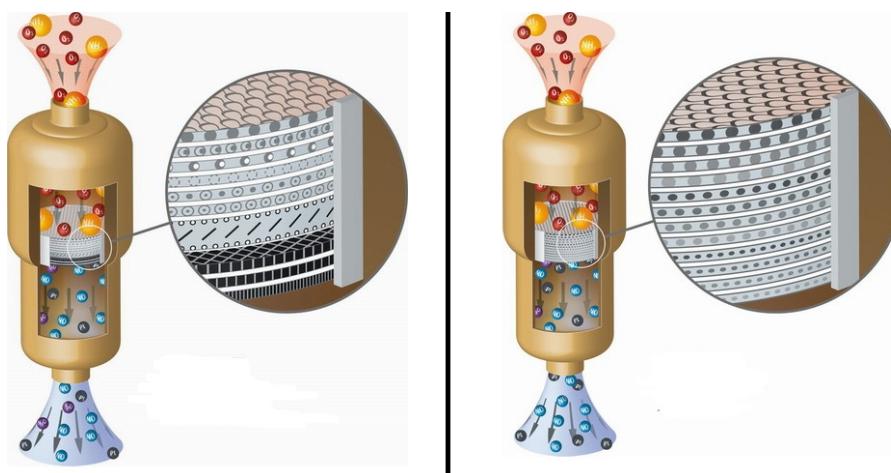
Figure 1.2: Two gauze-pack types offered by the company Umicore. The gauze-pack on the left is made for low and medium pressure plants, while the one on the right has a different composition and is made for high pressure plants. By comparing the two figures it can be seen that a denser gauze-pack structure is used for high pressure plants. [6]

1.3.2   Secondary abatement

The secondary abatement process can be divided in two types; homogeneous and catalytic decomposition in the burner. The reactions typically take place downstream of the ammonia burner. Both methods can be successful, but the homogeneous decomposition is only suitable for new plants.

Homogeneous decomposition in the burner

N_2O is metastable in the temperatures ranging from 1023-1223K and pressures of 1-13 bar [3]. This means that thermal decomposition of N_2O is possible under operational conditions of all three types of nitric acid plants. The decomposition is a relatively slow reaction in the ammonia burner, so in order for the decomposition to occur the ammonia burner needs to be redesigned to increase the residence time by extending the reactor chamber. This technology is developed and patented by Norsk Hydro [7]. Under testing conditions Norsk Hydro has documented a decomposition level of 84.8% for a residence time of 1s, and 97.3% for a residence time of 2s. The temperature corresponded to the operating temperature during ammonia combustion ($\approx$ 1175K).

Even though the method seems to be efficient, there are a few substantial disadvantages. The ammonia burner redesign is too expensive to be implemented in existing plants, so the method is only suitable for new plants. It is documented that high conversion levels (>90%) are difficult to achieve on a plant scale [3]. Moreover, the method

is not suited for atmospheric pressure plants .

Catalytic decomposition in the burner

Compared to the homogeneous decomposition, catalytic decomposition is a more cost-efficient option and can easily be applied in existing plants. The method implies no need for noticeable modifications to the existing burner.

The gauze-pack is usually supported by inert ceramic rings called Raschig rings. These rings can be replaced by a catalyst selective to decomposition of N_2O. The volume of the Raschig ring layer determines the available catalyst volume and thus also the N_2O reduction. This volume depends on the specific burner design. A typical catalyst bed height ranges from 5 to 20cm [3].

There are, however, challenges regarding the catalyst properties. Firstly, N_2O-decomposition catalyst should be inert towards the decomposition of NO, which is difficult to obtain since both NO and N_2O are thermodinamically unstable with respect to decomposition into N_2 and O_2. Secondly, the operation temperature is often between 1073 and 1223K and the process-gas consists of about 16 vol.% H_2O, 10 vol.% NO and 7 vol.% O_2 [3]. These conditions put severe demands on the catalyst.

1.4   Project motivation

The focus of this work is related to supported heterogeneous catalysts used for decomposition of nitrous oxide formed during nitric acid production (see section 2.1 for an explanation of heterogeneous catalysts and section 2.4.2 for an explanation of supported catalysts). The systems chosen are utilized in high-temperature applications and include a spinel catalyst $Co_{3-x}Mn_xO_4$ and a perovskite catalyst $LaMnO_3$ supported on aluminium oxide, α-Al_2O_3, and yttria stabilised zirconia, YSZ. Under high temperature conditions an interaction between the catalyst and support material can occur. This can lead to a loss of catalyst activity and selectivity as well as reduced lifetime. The interaction can be prevented if a barrier layer is deposited between the catalyst and the support. The objective of this project was to investigate the effectiveness of a barrier layer, and includes several milestones as described below.

1) The catalysts will to be synthesised by two different methods; the $Co_{3-x}Mn_xO_4$ catalyst will be synthesised by the coprecipitation method while the $LaMnO_3$ catalyst will be synthesised by the sol-gel method. **2)** Small platinum particles will be deposited onto the α-Al_2O_3 and YSZ surfaces in order to mark the original catalyst-support interface. This may be achieved by coating the single crystals with a thin platinum film (a few nm) and sinter at some temperature in order to form small metal particles on the surface. Required thickness of the deposited film and sintering temperature needed to form the desired small reference particles will be evaluated. **3)** An ink will be made out of the catalyst powders. The catalyst ink will be painted onto the platinum marked single crystals and annealed at high temperature to provoke a reaction at the catalyst-support interface. The catalyst-support interaction will be evaluated. **4)** Parallel to this, the work on barrier layer deposition will be carried out. A uniform barrier layer coating can be achieved by dip-coating the support single crystals in a dispersion containing barrier oxide particles where the support and the dispersion oxide particles have opposite charges at a common pH. For this purpose the surface charges of the single crystals and the barrier particles will have to be manipulated by polyelectrolyte adsorption. Chosen polyelectrolytes include polyacrylyc acid (cationic), PAA, and polyethylene imine (anionic), PEI. The surface charge of particles as a function of pH can be obtained by zeta potential measurements. The surface charge of solids cannot be measured directly, but can be investigated if the support materials are available in the form of nano-crystalline particles. A manufactured α-Al_2O_3 powder is available, but the particles will be downsized to the nano-range as to not sediment during zeta potential measurements. **5)** The optimum amount of poly-

mer needed, PAA and PEI, in relation to the surface area of the α-Al$_2$O$_3$ particles will be investigated. When this amount is established, the optimum amount of polymer according to the single crystal surface can be found if the specific surface area of the particles is known. The specific surface area of the particles will therefore be measured. **6)** The barrier layer- and YSZ-powders can either be purchased or, alternatively, synthesised by the sol-gel method. Polymer adsorption and surface area measurements will be carried out as outlined in point 5 above regarding the α-Al$_2$O$_3$ particles. **7)** The barrier coating can be deposited when the opposite charges between the supports and the barrier particles are generated. After deposition the barrier coating needs to be sintered at some temperature to form a monolayer of particles. The sintering temperature and coating thickness will be investigated. **8)** A catalyst ink will be painted onto the barrier coated and reference marked single crystals and annealed in the same way as the samples without the barrier layer. The catalyst-support interaction will be investigated.

Chapter 2

Background

2.1 Catalysts

Chemical reactions can have slow, rate-determining steps. A catalyst is a substance that accelerates a reaction by providing an alternative reaction path. The catalyst itself does not undergo a chemical change. A catalytic reaction is a cyclic process [8]. First, the reactant or reactants form a complex with the catalyst and the catalyst opens a new, thermodynamically favourable pathway upon which the product or products are formed. Afterwords, the product is released from the catalyst and the next cycle can proceed.

There are several types of catalysts. *Enzymes* are biological catalyst. They are very specific and can have a dramatic effect on the reactions they control [9]. As the name indicates, the main aim of *environmental catalysts* is environmental protection. Nitrogen oxides, NO_x, carbon monoxide, CO, and hydrocarbons are removed from vehicle exhaust by a so-called three-way catalyst. A *homogeneous catalyst* is a catalyst that is in the same phase as the reactants or their solution. An example is the decomposition of hydrogen peroxide in aqueous solution which is catalyzed by bromide ions [9]. A *heterogeneous catalyst* is in a different phase than the reactants. An example is the hydrogenation of ethene to ethane, a gas-phase reaction, which is catalyzed by a solid catalyst such as palladium, platinum, or nickel [9].

Catalysts must satisfy a variety of requirements including selectivity, activity, thermal and mechanical stability, poison resistance and, for industrial use, commercial feasibility [10]. Activity is defined as the specific rate of a reaction in numbers of product molecules per site per second. Selectivity is the tendency of one reaction occurring out of many possible reactions while lifetime is defined as the time of useful catalyst performance.

2.2 Development of the science of catalysis

Catalysis as a phenomenon was first recognized in 1835 by Berzelius [8]. From 1821 Berzelius summarized and reviewed scientific contributions world-wide in his Annual

Commercialization	Products	Catalyst
1939 - 1945	toluene from methylcyclohexane	$Pt-Al_2O_3$
	butadiene from n-butane	$Cr_2O_3-Al_2O_3$
1946 - 1960	fuels from high-boiling petroleum fractions	Ni-alumosilicate
	styrene from ethylbenzen	$Fe_2O_3-Cr_2O_3-KOH$
1961 - 1970	gasoline	bimetallic catalysts (Pt, Sn, Re, Ir)
	fructose from glucose (production of soft drinks)	enzymes immobilized on SiO_2
1971 - 1980	removal of NO_x, CO, CH_x	$Pt-Rh-CeO_2-Al_2O_3$
1981 - 1985	reduction of NO_x with NH_3 to N_2	V Ti (Mo, W)oxides (monoliths)
1986 -	acrylamid from acrylonitrile	enzymes

Table 2.1: The table shows a few important catalytic processes commercialized during and after World War II [8].

Report. In his report of 1835, a number of reactions that take place in the presence of a substance that is not affected were described [10]. However, Mitscherlich had already in 1834 identified several reactions which were caused by what he called contact. In fact, the term "contact catalysis" was still used into the middle of the 20th century.

The first major contribution to the understanding of catalysis was made by Ostwald during the beginning of the 19th century. Ostwald showed that a catalyst could not change the equilibrium of a reaction and he also identified a catalyst as a substance that cannot start but can accelerate a chemical reaction [8, 10]. For this work, Ostwald received the Nobel Prize in Chemistry in 1909.

The first industrial breakthrough was made in 1909 by Fritz Haber with the synthesis of ammonia over an osmium catalyst [8]. The process was commercialized in 1913 by the company BASF and their research team led by Carl Bosch. Today, the process is known as the *Haber-Bosch process*. Since that time, many industrial catalyst have been developed. Table 2.1 shows a few commercialized catalytic processes developed during and after World War II [8, 10].

2.3   Principles of catalysis

The principle of *active sites* is essential to the understanding of catalysis. Langmuir was the first to describe adsorption of a chemisorbed monolayer. In his model he assumed an array of sites, energetically identical and non-interacting where each site could adsorb just one molecule [8]. Not long after, experiments led to the conclusion that some modifications to the Langmuir model should be made. In 1925 Taylor identified that the active sites on the catalyst surface are heterogeneous. The atoms on the corners and edges of the catalyst surface have different coordination numbers and hence the corresponding sites have different activities [11]. In addition to variable coordination numbers, the composition of the catalyst surface can in many cases be quite different from that of the bulk [12]. The changes in the surface composition can be due to catalyst pretreatments like calcination and reduction, but also as a consequence of the catalytic reaction. At temperatures above the Tamman temperature, atoms in the bulk can migrate to the surface, while Hüttig temperature is enough to make atoms at the surface adequately mobile to undergo agglomeration and sintering (see section 4.3 for further explanation of Tamman and Hüttig temperature). This leads to a heterogeneity in the local environment of the surface atoms. Consequently, the surface composition is different for each crystallographic plane in multicomponent materials [8].

2.3.1   Modifiers in catalysis

Catalysts can be modified by promoters and poisons. These substances affect the activity, selectivity and lifetime of the catalyst [10]. A promoter enhances catalyst performance while a poison has undesirable effects. Identifying promoters and poisons in a given chemical reaction is of great importance in order to obtain efficient industrial operation.

Modifiers can be classified as either structural or bonding modifiers. Structural modifiers restructure catalyst surface and in this way also change the surface area of the catalyst. Bonding modifiers can bind to chemically reactive sites and change the electronic structure of adjacent sites due to charge transfer. In this way, the adsorption energies of the active sites are changed. For example, the two main additives in the promoted iron catalyst for ammonia synthesis are Al_2O_3 and K_2O. The effect of Al_2O_3 is to increase and stabilize the surface area of the catalyst, and Al_2O_3 is in this way acting as a structural promoter [13]. On the other hand, K_2O acts as a bonding promoter and affects the adsorption kinetics.

2.3.2 Deactivation and regeneration

During operation, catalysts are deactivated after a period of time. Some catalysts are deactivated after seconds or minutes while other remain active over several years. Deactivation is usually also followed by a loss of selectivity [10]. Main reasons for catalyst deactivation are:

1. **Poisoning**: Poisoning is the most common cause of catalyst deactivation and is a result of blocking of active sites. The active sites can be blocked either by chemisorption of unwanted elements/compounds or by formation of surface complexes.

2. **Fouling**: Most catalysts and catalyst supports are porous. Fouling is a result of blockage of pores/micropores by polymeric compounds.

3. **Thermal degradation**: There are several types of thermal degradation. Solid-solid reaction often occur at high temperatures (above 500°C). The rate of sintering also increases with increasing temperature. Moreover, phase changes can occur by thermal treatment.

4. **Volatization of active components** For example Cu, Ni, Fe and noble metals can escape from catalysts after conversion to volatile chlorides if traces of chlorine are present [8].

Whether or not catalyst regeneration is possible depends on the mechanism by wich the catalyst has been deactivated. Some catalyst deactivated by poisoning can be regenerated. Ni catalysts poisoned with CO or HCN can for example be regenerated by H_2 treatment at temperatures that allow formation of methane and NH_3 [8]. Regeneration of catalyst deactivated by fouling is also possible, while catalysts deactivated by thermal degradation are generally difficult to regenerate. Some $Pt-Al_2O_3$ catalyst deactivated by Pt sintering can be partly regenerated by chlorine treatment at elevated temperatures.

2.4 Unsupported and supported solid catalysts

2.4.1 Unsupported catalysts

Unsupported catalysts can for example include metal oxides, aluminium silicates and zeolites [14]. Transition metal oxides and complex multicomponent oxides like perovskites and spinels are particularly interesting due to the variability in oxidation

states as well as the possibility of forming mixed-valence and non-stoichiometric compounds. An overview of unsupported catalysts that decompose N_2O is given in section 2.5.

2.4.2 Supported catalysts

Many catalysts are supported, meaning that a thin catalyst layer (20-100μm) is deposited on a porous support material [8]. This enhances the effectiveness through increased surface area and minimize cost since the support structure is cheaper than the produced catalyst. Figure 2.1 shows two typical ceramic structures, a honeycomb and a sponge.

Many materials used as unsupported catalysts can also be used as support materials. α-Al_2O_3, SiO_2, MgO and ZrO_2 are among the most frequently used support materials [8]. Metallic support structures may also be used and they are usually formed from heat resistant stainless steels [14].

Often, the support material and catalyst interact. This is most crucial in high temperature processes where the catalyst is deactivated mainly by thermal degradation. In the case of ceramic support structures, interactions may include the formation of new phases at the catalyst-ceramic interface or by diffusion or inter-diffusion of catalyst and ceramic components [14]. A reaction between a large support and a thin catalyst layer may lead to a substantial change in the catalyst composition and furthermore have a negative effect on catalyst performance. In addition, the new phase can itself catalyse undesired reactions. One way of bypassing the problem is by physically separating the catalyst from the support. An important property of the intermediate/barrier layer is in this case that it does not react strongly with neither the catalyst nor the support. It is also important that the barrier layer conforms to the geometry of the support structure.

In this work, first a reaction between a catalyst and a support will be analysed. Knowledge on which type of reactions occur at the interface can aid the selection of a barrier layer material. The surface of the barrier particles and the surface of the support will be adjusted to be of opposite charge by polyelectrolyte adsorption. In this way the barrier layer can be deposited by dip-coating, and conformation of the barrier layer to the geometry of the support structure is assured.

Figure 2.1: An illustration of two types of typical support structures with large surface areas; a honeycomb structure on the left [15] and a sponge structure on the right [16].

2.5 Decomposition of N_2O

N_2O has a long history as a probe molecule in the study of catalysis and reaction kinetics. Early studies of decomposition of nitrous oxide focussed on metal catalysts, especially platinum. Already in 1924 Hinshelwood and Burk studied the homogeneous decomposition of nitrous oxide [17]. This study was followed up by studies on heterogeneous decomposition of nitrous oxide on the surfaces of platinum and gold published by Hinshelwood and Prichard in 1925 [18, 19]. Other metal catalysts include Pd, Ag and Ge [20].

Pure, unsupported, oxides were extensively studied by Winter [21, 22, 23, 24]. These studies showed that CuO and IrO_2 were particularly active towards decomposition of nitrous oxide. CaO, SrO and HfO_2 were reported to have high activities pr. surface area. La_2O_3 was found to be the most active rare earth oxide. Yamashita and Vannice studied the catalytic decomposition of N_2O over four different manganese oxides, MnO, Mn_3O_4, Mn_2O_3, MnO_2, and showed that valence of the element also is important [25]. The reported activity order is $MnO < MnO_2 < Mn_3O_4 < Mn_2O_3$. Moreover, some of the oxides were unstable under experimental conditions. MnO_2 was reduced to MnO. Other oxides, Cu_2O and CoO, have also been reported to be unstable, although CoO initially was reported to have a higher activity than CuO. [26, 27].

Due to instability issues and out of the desire to develop more active systems, research started to focus on doped oxide solid solutions [20]. Cimino *et al.* studied systematically the effect of decomposition of N_2O over MgO catalyst doped with NiO [28, 29]. The atomic nickel content ranged from 0.15 atomic% to 50 atomic%. Pure MgO was

found to show very low catalytic activity. Even small additions of NiO to MgO considerably enhanced the catalytic activity. The catalytic activity pr. nickel ion was also shown to be higher in more diluted ($\approx$1%) MgO-NiO solid solutions. Other studies confirmed a general trend where the catalytic activity strongly increases already when small amounts of a transition metal are added and that the catalytic activities pr. transition metal ion are higher in diluted solid solutions [30, 31, 32, 33]. Cimino and Indovina also demonstrated that Mn^{3+}-ions are more active than both Mn^{2+} and Mn^{4+}-ions dispersed in an MgO matrix [34]. This is consistent with the results on pure oxides [25]. Also, diluted catalysts with a given $[Mn^{3+}]/[Mn^{4+}]$ ratio were also more active than concentrated catalysts with a similar $[Mn^{3+}]/[Mn^{4+}]$ ratio [34].

Perovskites and other mixed oxides are often used as catalysts due to their wide composition range and stability. Figure 2.2 shows a model of a perovskite unit cell. Perovskites have a general formula ABX_3 where A and B are cations and X is an anion. The structure is often adopted by oxides, so X is often an oxygen atom. Cubic perovskites are described by the space group Pm$\bar{3}$m. Over 90% of the natural metallic elements are known to be stable in a perovskite structure [35]. Multicomponent perovskites can be synthesised by partial substitution of cations A and B, $(A_xA'_{1-x})(B_yB'_{1-y})O_3$, giving rise to a variety of compounds which can be used as catalysts. The size difference between A- and B-ions is important for the stability of the structure. In the perovskite structure the ionic radius of the A-atom should be much larger than that of the B-atom. For oxides, the lower limits for cationic radii are r_A>90pm and r_B>51pm [35]. The A-ion is often a rare earth element, mostly La, for catalysts used in decomposition of N_2O [20].

The catalytic activity of $LaMO_3$ for oxidation reactions is determined by the B-ion [35, 36]. Wang *et al.* studied the catalytic decomposition of N_2O over perovskites $LaMO_3$ (M=Cr, Mn, Fe, Co and Ni) and perovskite-like structures La_2MO_4 (M=Co, Ni and Cu) [37]. The reported results are summarized in figure 2.3 showing the catalytic activity of $LaMO_3$ and La_2MO_4 plotted against the sequence of transition elements. Table 2.2 summarizes the reported structures of the catalysts. The reported activity order was Cr < Mn < Fe < Ni < Co for the $LaMO_3$-structure and Cu < Ni < Co for the La_2MO_3 structure. Moreover, the activities of $LaCoO_3$ and La_2CoO_4 were substantially higher than of the other oxides studied in reference [37].

The specific surface areas of perovskites and perovskite-like catalyst are, in general, low (<10m^2/g) due to high temperature preparation methods [20]. Higher specific
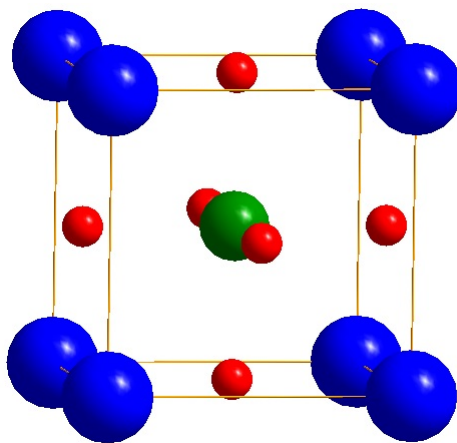
Figure 2.2: A unit cell models of a perovskite with a general formula ABX_3 and space groupe Pm$\bar{3}$m. Blue spheres represent A-ions, greene spheres B-ions and red spheres O-ions. Diamond software was used.

Catalyst	Structure
$LaCrO_3$	P(O)
$LaMnO_3$	P(R)
$LaFeO_3$	P(O)
$LaCoO_3$	P(O)
$LaNiO_3$	P(R)
La_2CoO_3	K(O)
La_2NiO_3	K(T)

Table 2.2: Catalyst structures reported by Wang *et al*. P: Perovskite, K:K_2NiF_4-type structure, O: Orthorhombic, R: Rhombohedral, T: Tetragonal [37].
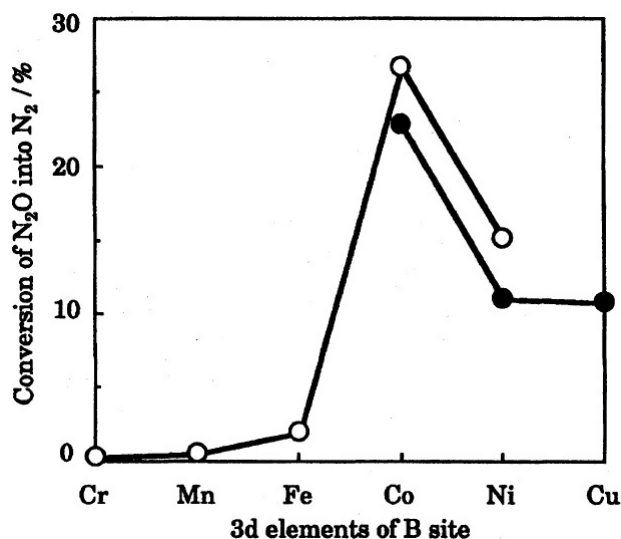
Figure 2.3: Activity profiles of N$_2$O decomposition over LaMO$_3$ (white circles) and La$_2$MO$_3$ (black circles) at 723K [37].

surface areas can be achieved by combination of the perovskite catalyst with a high surface area support. Often, the activities of supported oxides are compatible with the activities of the corresponding unsupported oxides [20]. For example, catalysts containing cobalt are generally very active towards N$_2$O decomposition [5]. Regarding supported catalyst, CoO is, for example, reported to be much more active than CuO and Fe$_2$O$_3$ when supported on SiO$_2$ [38]. Tuti *et al.* studied the decomposition of N$_2$O on CoO$_x$, CuO$_x$ and FeO$_x$ catalysts supported on ZrO$_2$ [39]. The reported activity pattern was Co>Cu≫Fe, which is in compliance with studies on pure oxides and SiO$_2$ supported oxides [26, 27, 38]. It is also shown that the support itself can act as a promoter for the catalytic reaction. Centi *et al.* found that Cu was more active on ZrO$_2$ than Cu on Al$_2$O$_3$, SiO$_2$ and TiO$_2$ [40]. Moreover, they also showed that the maximum specific activity per copper ion is reached for a copper loading corresponding to approximately one fourth of the amount required to form a complete monolayer coverage. This suggests that the zirconia surface itself has a catalytic role. The crystalline form of zirconia also plays a role. The tetragonal phase is reported to be more effective in enhancing the activity of copper phase than the corresponding monoclinic phase. These results are also supported by other publications [41, 42]. Often, interactions between the transition metals and support take place. For example, the formation of a spinel phase NiAl$_2$O$_4$ is reported when Ni^{2+}-ions are supported on γ- and η-Al$_2$O$_3$ [43]. For the system Co^{2+}/Al$_2$O$_3$ the phase CoAl$_2$O$_4$ is formed to approximately 2 atomic% Co and as the Co content increases the Co$_3$O$_4$ phase is formed [44]. Depending on the Mn content, Mn-ions supported on γ- and η-Al$_2$O$_3$ can form

α-Mn_2O_3, MnO or $MnAl_2O_4$ phases [45]. It is clear that the interaction depends on several factors like the nature of the ions and the support, the concentration and the experimental conditions.

2.5.1 Decomposition of N_2O on plant scale

Primary abatement

The high cost of Pt-Rh gauzes and subsequent metal loss has motivated the research towards substitution of Pt-Rh gauzes by oxide catalysts [3]. The most active simple transition metal oxides tested under operational conditions of a high-pressure nitric acid plant are Co_3O_4, MnO_2, Cr_2O_3 and CuO. Complex oxides with a perovskite type structure show a high selectivity towards NO at operating temperatures around 900°C, even when composing transition metal oxides such as copper and nickel oxides are not selective by themselves [46]. The activity and selectivity towards nitrous oxide usually correlate. Unfortunately there are also some substantial disadvantages of oxide-based catalysts. The most crucial aspect with regards to industrial process economics is the lower conversion rate of NH_3 to NO [3]. The contact time of the most active oxides is reported to range from 10^{-2} to 10^{-1}s, while the contact time on platinum gauzes is 10^{-4}s. Moreover, the oxide catalyst selectivity towards NO is always lower than that of platinum gauzes. Another disadvantage is the reduction of the oxides under operating conditions of a nitric acid plant. For example, pure Co_3O_4 is transformed to less selective CoO and MnO_2 is transformed to Mn_3O_4. Promoters can be introduced to increase the stability of the oxides, but this may also lead to a decrease in NO selectivity.

"State Institute of Nitrogen Industry in Russia" (GIAP) proposed a combined bed idea where an oxide catalyst is used with a fewer number of gauzes. In the 1950s a dual-bed system was installed in an atmospheric pressure plant. The dual-bed contained Pt-gauzes along with an iron-chromium catalyst. In the 1990s GIAP together with the Boreskov Institute of Catalysis developed an iron-aluminium oxide catalyst in the form of granules and honeycombs. Under optimized conditions the platinum metal loading and losses were reduced while the NO yield was the same as for standard loading of Pt-gauzes.

Secondary abatement

Several companies have made an intensive effort to develop and install a catalyst in the space available under the Pt-Rh gauzes [3]. Catalyst selectivity is an important issue since there is a potential loss of product due to catalytic decomposition of NO. Both NO and N_2O are thermodynamically unstable with respect to decomposition into N_2 and O_2. The research has focused on spinel- and perovskite-type materials [3]. In March and July 1999 the company BASF successfully installed a supported oxide catalyst CuO/Al_2O_3 in their commercial production plant. Norsk Hydro, now Yara International, have also been active in the development of a highly active, selective and stable catalyst [3]. Their research has mainly focused on Co_3O_4 as the baseline active phase [5]. Co_3O_4 is however reduced CoO under operational conditions of the plant. Stability can be increased by Co-substitution and the formation of a spinel type structure. Yara completed a successful plant test of a Co_2AlO_4 catalyst supported on CeO_2 in the period 2002-2004 and followed up by a commercialization of the catalyst in 2005/2006. Moreover, the company has patented a spinel catalyst with a general formula $Co_{3-x}M_xO_4$, where M = Fe, Al and x=0-2, supported on CeO_2 [47].

In the current project the selected catalysts include a spinel catalyst $Co_{3-x}Mn_xO_4$ and a perovskite catalyst $LaMnO_3$. The selected support materials include planar α-Al_2O_3 and YSZ single crystals. The main objective is to identify the effectiveness of a barrier layer that can prevent/minimize catalyst-support interaction. Prior to this, the catalyst-support interactions without a barrier layer will be investigated.

Chapter 3

Theory

3.1 Catalyst synthesis

Two catalyst materials will be prepared in this work. The $Co_{3-x}Mn_xO_4$ catalyst will be prepared by coprecipitation and the $LaMnO_3$ catalyst will be prepared by the sol-gel method. In general, there are many ways in which a catalyst active phase may be prepared. These include solid-state reactions, crystallization, freeze drying, coprecipitation and many more [48].

Surface area of a catalyst has an important effect on the reaction rate, so it is important that the catalyst end product has a high surface area. Specific surface area, SSA, is defined as the total surface area of a material pr. mass unit; $[\frac{m^2}{g}]$. SSA is related to particle size by [49]:

$$SSA = \frac{6}{\rho \cdot d} \tag{3.1}$$

where ρ is the density of the solid and d is the particle diameter of spherical particles or particle edge length of cubic particles.

3.1.1 Solid-state method

Many oxide catalyst materials contain more than one metal species. The oldest and still most common method of preparing multicomponent solid materials is by direct reaction of solid components at high temperatures [50]. This is commonly called *the solid-state reaction*.

The starting point of the reaction is two regions, A and B, in contact with each other. Figure 3.1 illustrates the A and B regions as well as as well as the formation AB- and BC-interfaces which arise as the product layers C is formed. When the product layer C is formed A and B ions must interdiffuse through the product layer to the new reaction interfaces in order for further reaction to occur. Diffusion is a thermally activated process. The higher the temperature, the faster the diffusion. The product layer becomes thicker as the reaction progresses leading to longer interdiffusion distances. Eventually, this results in slower reaction rates. The diffusion may not be equal in both directions.
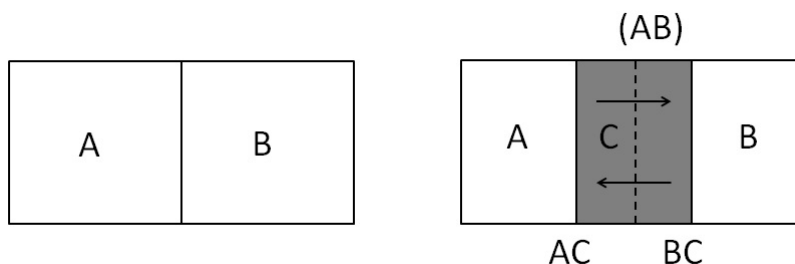
Figure 3.1: The figure on the left illustrates A and B regions as well as the AB-interface. The figure on the right illustrates the interdiffusion of A and B, the formation of product C as well as the formation of two new interfaces AC and AB. The initial AB-interface is also indicated. In this case the diffusion of both ions is assumed to be equal.

This method has several disadvantages with regard to preparation of mixed oxides. The most important one is that the high temperature also promotes grain growth, resulting in lower SSA by equation (3.1).

3.1.2   Coprecipitation method

The catalyst material may be synthesised by the coprecipitation method instead of the solid-state method. The coprecipitation method allows catalyst formation at lower temperatures then what is required in the solid-state method because the diffusion distance of the ions is reduced. In this way grain growth can be minimized. An acidic metal solution is usually precipitated with a basic solution for the synthesis of mixed oxides. Best results are obtained if the metal ions have similar ionic radii, the metal salts have similar solubility and the precipitation rate is similar [48, 50].

Preparation of a catalyst by coprecipitation includes many steps; precipitation, filtration, washing, drying, shaping, calcination, and sometimes activation [51]. The basic properties of a catalyst are established during precipitation, making it the most important step during catalyst preparation. Precipitation itself includes three steps: liquid mixing, nucleation and crystal growth, and aggregation.

There are three options on how to mix the two solutions. The base can be added to the acidic metal solution, *forward coprecipitation*, or the acidic metal solution can be added to the base, *reverse coprecipitation*, or both solutions can be mixed simultaneously [51]. The pH either rises (base to acid) or declines (acid to base) when the precipitation is carried out by the first two methods. This means that the product formed at the be-
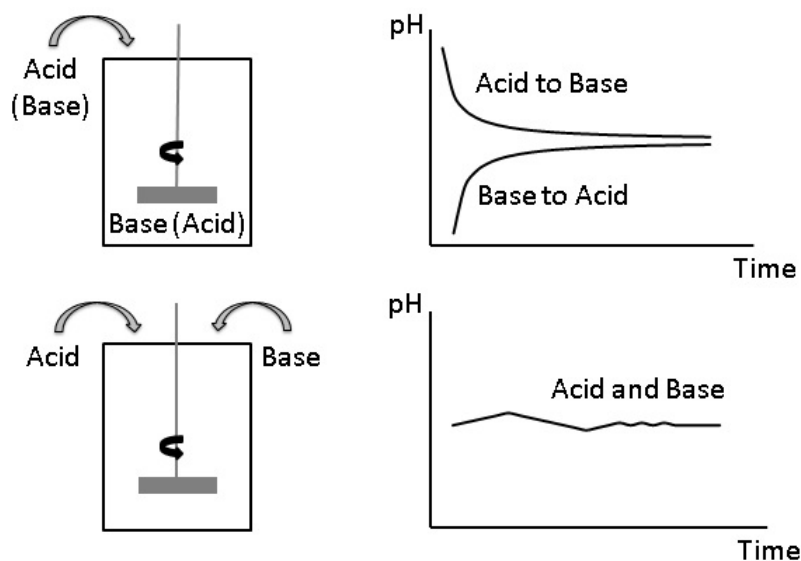
Figure 3.2: Precipitation processing routes: forward (base to acid) and reverse (acid to base) precipitation, continuous precipitation, and corresponding pH profiles.

ginning of the precipitation may not be the same as the one formed at the end of the precipitation. The least-soluble product will precipitate first leading to a sometimes undesirable sequential precipitation of ingredients [51]. The reactants can be mixed simultaneously to minimize the formation of mixed products. The pH throughout mixing will be approximately constant. Figure 3.2 illustrates the gradual pH change when the precipitation is carried out by forward and reverse coprecipitation as well as the more constant pH-value throughout the precipitation when the two solutions are mixed simultaneously.

Depending on the concentration and the rate of stirring, either nucleation or crystal growth is promoted. The desired small precipitate particles are obtained when nucleation is the favoured process. Variables that promote nucleation are high degree of supersaturation, i.e. high concentrations, rapid stirring and high temperature. Furthermore, high temperature also gives rapid precipitation kinetics. Often, one molar solutions of acid and base are precipitated at 60-70°C [48]. Precipitation from more dilute solutions at lower temperatures promotes crystal growth and favours production of fewer, larger crystals.

The precipitation is followed by aging. Aging is simply the stirring of the precipitate slurry for a period of time. This allows the maximum precipitation of the metal ions. Aging may also involve phase transitions in the slurry. Coprecipitation often results

in amorphous material as a first phase [51]. During aging, the amorphous phase may convert to a crystalline phase. After aging the precipitate may be separated from the liquid phase by filtration. The filter cake is washed to remove the precipitate liquor.

After filtration and washing, the precursor phase is calcined to produce the mixed oxide. The precursor phase is thermally decomposed producing small oxide particles. This allows the formation of the mixed oxide at a lower temperature than what would be needed in the solid-state method. In the most favourable case, the precipitated precursor phase will contain all the metal ions within its structure. This gives the shortest required diffusion distance to produce mixed oxides.

3.1.3   Sol-gel method

The sol-gel method, also called the Pechini or complexation method, is widely used for the preparation of solid catalytic materials [51]. This is due to the flexibility of the method where a variety of precursor chemical properties and preparation parameters can be adjusted depending on the desired catalytic material. This also introduces a complexity in the selection of the optimal chemical route and processing sequence and conditions. As the coprecipitation method, the sol-gel method includes several steps. These are illustrated in figure 3.3 [52].

If the sol-gel precursors are chemically inert, they need to be activated. For the preparation of a metal oxide this involves hydrolysis of metal ions in an aqueous solution. The activated precursors continue to react with each other to form an oligomeric colloidal solution. A polydentate chelating agent is added to the solution to form a metal cation complex. The metal cation complexes are randomly distributed throughout the solution. After chelation a polyfunctional alcohol is added. The resulting solution is heated to carry out a polyesterification reaction between the metal cation complex and the polyfunctional alcohol. After a period of time called the "gelation time" the sol is transformed into a gel. This is a result of the formation of an organic network, which consists of condensed colloidal clusters entrapping the solution [51]. The gel contains a random distribution of metal ions attached to the organic network. The gel structure is determined by the ionic character of the M-O bond, and the relationship between the activation/condensation rates [51]. During aging the structure and properties of the formed network continue to change up to the point that yields the target gel density. Further heating will result in an oxidation or decomposition of the organic network producing small oxide or mixed oxide particles. In the end, the produced powder is calcined to give the final catalyst end product.
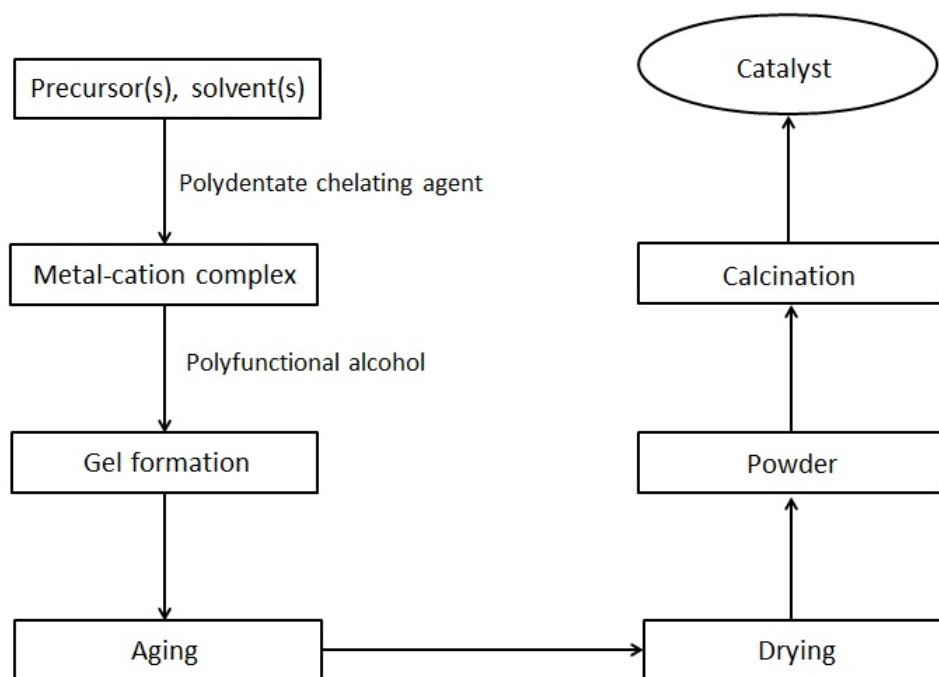
Figure 3.3: The sequence of steps included in the sol-gel method.

Typical chelating agents include citric acid, ammonium salt of ethylenediaminete-traacetic acid, EDTA, and glycine. A typical polyfunctional alcohol is ethylene glycol [48]. Variables in the process include the ratio of metal ions and chelating agent, and the ratio of chelating agent to polyfunctional alcohol.
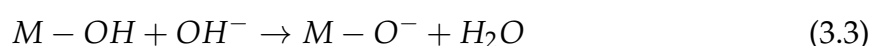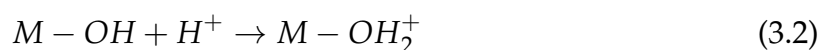
3.2 Surface charge

Many physical chemistry properties of materials are dependent on electrical charges of surfaces. The subject is broad, and will here be limited to the areas having direct implications for barrier layer and catalyst coating deposition. This includes dissociation of oxide surface groups as well as manipulation of surface charge by polyelectrolyte adsorption.

3.2.1 The origin of charges

The interface between different substances is (almost) always charged [53]. These charges can originate from several mechanisms:

1. Dissociation of surface groups.

2. Adsorption of ions.

3. Dissolution of ions.

4. Isomorphous substitution.

Dissociation of surface groups is a common mechanism for minerals (oxides) and biological surfaces. When dispersed in water, the surface of most oxides will become hydroxylated (M-OH). Depending on the chemistry of the oxide and the pH, the hydroxyl groups will have either acidic or basic properties. At a given pH the surface will have zero charge. This is referred to as *the point of zero charge*, PZC . If there is no adsorption of other ions than H^+ and OH^- the term *isoelectric point*, IEP, is used instead. In the absence of chemisorbed or physisorbed species PZC will be the same as IEP. Surface charge will be positive at a pH below IEP, and negative at a pH above IEP by reactions 3.2 and 3.3. However, in the presence of a specific adsorption PZC and IEP will in general have different values.

$$M - OH + H^+ \rightarrow M - OH_2^+ \tag{3.2}$$

$$M - OH + OH^- \rightarrow M - O^- + H_2O \tag{3.3}$$

Another important mechanism for generating surface charge is adsorption of ionic surface active substances. Adsorbed ionic surface active substances will usually determine the surface charge [53]. These can be anionic or cationic surfactants or polyelectrolytes[1]. Surfactants and polyelectrolytes may dissociate depending on pH in a

---

[1]Polyelectrolytes are charged polymers where the repeating monomer has a charged part.

(a) Steric stabilization of particles.

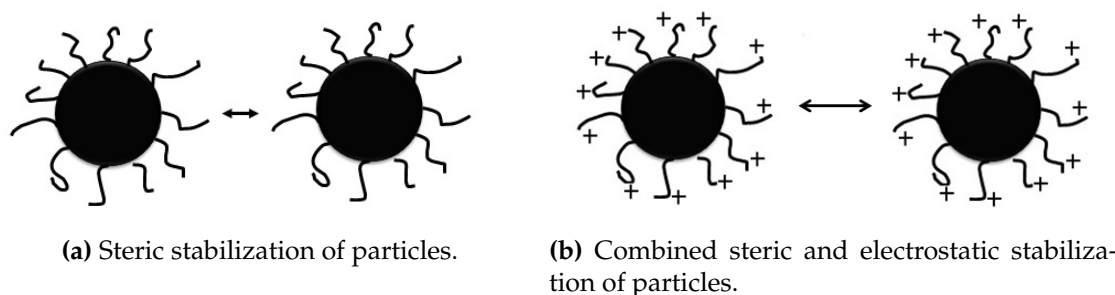**(b)** Combined steric and electrostatic stabilization of particles.

Figure 3.4: The figure illustrates polymer adsorption on uncharged particles with **a)** a neutral polymer and **b)** a charged polymer.

similar way as described in reactions 3.2 and 3.3. Examples of anionic polyelectrolytes are poly(acrylic acid), PAA, and gelatin, while examples of cationic polyelectrolyes are poly(vinyl pyrolidon), PVP, and poly(ethylenimin), PEI.

In addition to the surface charge effect, polymer adsorption in general may also lead to particle stabilization by steric effects. Here, interpenetrating polymer chains create a repulsive force between the particles. Neutral polymers will give a pure steric effect while polyelectrolytes will give a combined steric and electrostatic stabilizing effect, see figure 3.4. Unfortunately, predicting the effect of polymer adsorption on particle stability is difficult [53]. Depending on concentration, solvency and temperature polymers are often able to both stabilize and flocculate/coagulate dispersions. Bridging is the most common flocculation mechanism for both neutral polymers and polyelectrolytes. Bridging occurs because the surfaces often are only partially covered by the polymer. One polymer chain can adsorb to more than one particle and thus function as a bridge.

The last two mechanisms are not directly relevant for this work and will therefore only be explained briefly. Dissolution of ions corresponds to dissociation of insoluble salts. The cations and anions have different sizes and are bound with different strengths in the surface layer. In order to reach IEP or PZC an excess of one ion type is needed. In isomorphous substitution ions in the crystal lattice are substituted by other ions of similar size, but with a different charge. The crystal will have a charge excess or a charge deficit.

3.3 Particle characteristics

3.3.1 Particle size distribution

Particle size distributions can either be represented as a differential or a cumulative distribution. In a differential distribution all particles within an interval are counted. A cumulative distribution is a sum where the particles within an interval are counted in addition to the ones below the interval in question. Cumulative distributions are usually reported in percentages, also called percentiles. For example, a diameter at 10% means that 10% of the particles will be below this size. A diameter at 50% describes the median diameter.

An average particle size is calculated for particles in dispersions. Various particle properties can be measured to give the average value. It is important to notice that the calculated average value is dependent on the physical property that is measured. For example, the average particle size calculated by a volume average will, in general, be smaller than if the particle size was calculated by a weight average.

3.3.2 Surface area

The term *surface area* does not only cover the outer macroscopic surface area, but also the inner surface area of pores. Surface area of solid materials can be determined by adsorption measurements of a gas onto the surface of the solid [54]. There are two ways in which a molecule can adsorb to a surface. Chemisorption describes a process where a molecule is bound to the surface with the same kind of bonds as found in regular chemical bonds. The maximum number of molecules that can be adsorbed to the surface by chemisorption corresponds to a monolayer [2]. In contrary, physisorption describes the process where the molecule is bound to the surface by weak van der Waals bonds. Molecules adsorbed by physisorption can form multiple layers.

---

[2]A monolayer gives complete coverage of the adsorption sites on the surface.

Adsorption is usually described by isotherms. An adsorption isotherm is a function which describes the amount of adsorbed gas on a given surface as a function of partial gas pressure at constant temperature. Langmuir adsorption isotherm gives a good description of a chemisorbed monolayer [54]. The linearized Langmuir isotherm is:

$$\frac{p_A}{v} = \frac{1}{K_A v_{mono}} + \frac{1}{v_{mono}} \cdot p_A \qquad (3.4)$$

where p_A is the partial pressure of the gas, K_A the equilibrium constant and v_{mono} the STP [3] gasvolume needed to form a monolayer.

Multilayer physisorption is best described by the BET isotherm, named after Brunauer, Emmet and Teller [54]. The linearized form of the BET isotherm is:

$$\frac{p_{rel}}{v(1 - p_{rel})} = \frac{1}{c v_{mono}} + \frac{(c-1)}{c v_{mono}} \cdot p_{rel} \qquad (3.5)$$

where p_{rel} is the relative gas pressure $\left(\frac{p_A}{p_0}\right)$, v the STP volume of adsorbed gas, v_{mono} the STP volume of gas needed to form a monolayer and c is the equilibrium constant.

---

[3]Standard temperature and pressure

3.4 Crystallography and crystal structures

Crystalline materials are built up of a periodic arrangement of repeating units. The smallest repeating unit is called *the basis*. The basis can contain one atom or a group of atoms. Lattice points are descrete values in real space. If a lattice point is chosen as the origin, any other lattice point can be defined by a vector **R**:

$$\mathbf{R} = u\mathbf{a} + v\mathbf{b} + w\mathbf{c} \tag{3.6}$$

where vectors **a**, **b** and **c** are the lattice parameters.

A collection of lattice points defines a unit cell. There are four different types of unit cells:

1. Primitive, P, with only one lattice point (at the corner).

2. Body-centered, I, with an additional lattice point in the center of the cell.

3. Face-centered, F, with additional lattice points in the center of each face of the cell.

4. Base-centered, A, B or C, with additional lattice points at just one of the cells faces.

Together with 7 crystal systems, 42 combinations of unit cells are possible [55]. However, out of these 42 combinations only 14 are symmetrically unequivalent. These are called *Bravais lattices*. Figure 3.5 shows an overview of the 7 crystal systems and 14 Bravais lattices.

Since a crystal is periodic in all three dimensions, it can also be described by its symmetry. The classification of crystals is in fact based on the crystals symmetry elements. Symmetry elements that do not involve translation are inversion, mirror plane, and rotation [55]. These three symmetry elements give rise to 32 unique combinations and are called *crystallographic point groups*. Symmetry elements that include translation are screw axes and glide planes. Combined with the crystallographic point groups 230 unique combinations are possible. These are called *space groups*. Every crystal can be described by a space group.
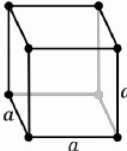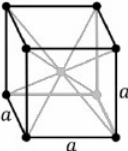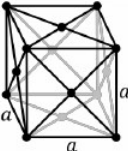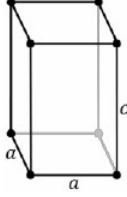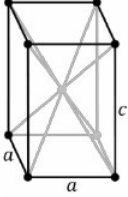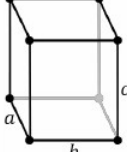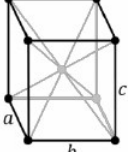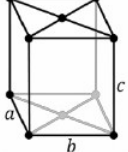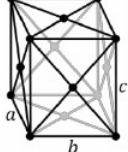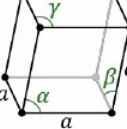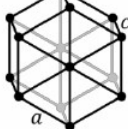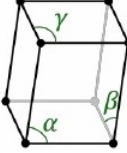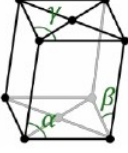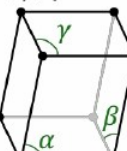
Figure 3.5: Overview of the 7 crystal systems and 14 unique Bravais lattices. P indicates a primitive unit cell, I a body-centered unit cell, F a face-centered unit cell and C a base-centered unit cell with a lattice point on the C-face.

Real space	Notation
Plane	(hkl)
Equivalent planes	{hkl}
Direction	[hkl]
Equivalent directions	⟨hkl⟩

Table 3.1: Notation for Miller indices in real space.

3.4.1 Crystal planes

In crystallography, Bravais lattice planes are specified in terms of Miller indices. Miller indices are denoted with integer values h, k, l. The values of h, k, l are given as the inverse of the plane's intersection with the lattice parameters **a**, **b** and **c**, meaning that $h = \frac{1}{a}$, $k = \frac{1}{b}$, and $l = \frac{1}{c}$. Values h, k, l, written in round brackets, (h k l), describe a plane. Negative h, k, l-values are indicated with a bar; for example ($\bar{1}$ 0 0). Equivalent planes are indicated with curly instead of round brackets. In cubic systems, {1 0 0} represents the set of planes (1 0 0), (0 1 0), (0 0 1), (1 1 0), (1 0 1), (0 1 1), as well as negative h, k, l variations of these.

Directions in a crystal are vectors pointing from the origin and to a point with coordinates (u, v, w). Square brackets are used, and as for vectors in general the vector [u v w] also represents all parallel directions like for example [2u 2v 2w] = 2[u v w]. If there are equivalent directions in the crystal due to symmetry, these are represented by the notation ⟨u v w⟩. In cubic systems ⟨1 0 0⟩ represents the six directions [1 0 0], [0 1 0], [0 0 1], [$\bar{1}$ 0 0], [0 $\bar{1}$ 0] and [0 0 $\bar{1}$]. Table 3.1 summarizes Miller indices notation for planes and directions in a crystal.

The term zone is used if there is a set of planes in the crystal which are all parallel to a single direction. Direction [u v w] is a zone axis if and only if [u v w] is orthogonal to the normal vectors of the planes in the zone.

3.4.2 Reciprocal space

Reciprocal space is a mathematical construction which is in crystallography used to analyse diffraction patterns of crystals. The reciprocal lattice is defined by the reciprocal lattice vectors $\mathbf{a}^*$, $\mathbf{b}^*$ and $\mathbf{c}^*$ which are related to the lattice vectors in real space by:

$$\mathbf{a}^* = \frac{\mathbf{b} \times \mathbf{c}}{V}; \mathbf{b}^* = \frac{\mathbf{c} \times \mathbf{a}}{V}; \mathbf{c}^* = \frac{\mathbf{a} \times \mathbf{b}}{V} \tag{3.7}$$

where V is the volume of the unit cell in real space given by $V = \mathbf{a} \cdot (\mathbf{b} \times \mathbf{c})$.

There is a close relation between the planes (h k l) in real space and the reciprocal space which is given by the vector $\mathbf{g}_{hkl}$:

$$\mathbf{g}_{hkl} = h\mathbf{a}^* + k\mathbf{b}^* + l\mathbf{c}^* \tag{3.8}$$

where *h, k, l* are the Miller indices of the plane in real space and $\mathbf{a}^*$, $\mathbf{b}^*$ and $\mathbf{c}^*$ are the reciprocal lattice vectors.

This means that a set of planes (h k l) in real space correspond to a point g_{hkl} in reciprocal space. Furthermore, the direction of the reciprocal lattice vector corresponds to the normal of the real space planes. The interplanar spacing, d, is given by:

$$d_{hkl} = \frac{1}{|\mathbf{g}_{hkl}|} \tag{3.9}$$

where $\mathbf{g}_{hkl}$ is the reciprocal lattice vector defined in equation (3.8).

3.5 Diffraction

Accelerated electrons and X-rays have the potential to ionize matter. Interaction between ionizing radiation and matter gives rise to a wide range of secondary signals. Both X-rays and electrons are easily deflected from their path due to Coulomb interactions with the electron cloud. In addition, electrons can interact with the nucleus of the atom. The interaction between electrons and matter is therefore stronger than the interaction with X-rays and matter.

3.5.1 Terminology of scattering and diffraction

Coulomb interaction between an atom and the passing electron is usually referred to as *scattering*. When describing scattering events electrons are thought of as particles. A
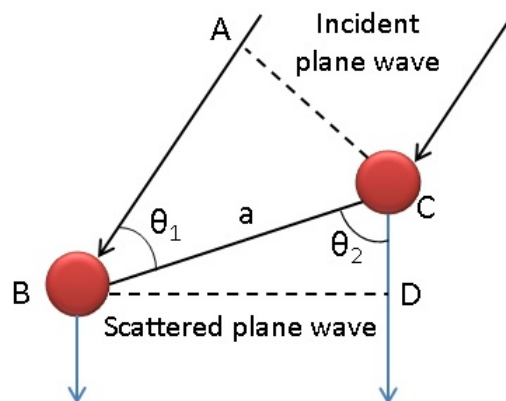
Figure 3.6: Two atoms B and C are a distance *a* apart. A wave is incident at an angle θ_1 and scattered at an angle θ_2. The path difference between incident and scattered wave is AB-CD.

scattering event can be either *ellastic* or *inellastic* describing scattering that, respectively, results in no energy loss or a measurable energy loss. Scattering events can result in different angular distributions. Electrons can be either *forward scattered*, $\theta_{sc} < 90°$, or *back scattered*, $\theta_{sc} > 90°$.

Diffraction is a form of ellastic scattering and describes the phenomena which occurs when a wave encounters an obstacle. The effect of diffraction is however observable only when the propagating wave has a wavelength similar to the dimensions of the diffracting object. Superposition of the diffracted waves, *interference*, occurs if the object has multiple closely spaced openings. The interference pattern has varying intensities where the maximum and minimum intensities are referred to as *constructive* and *destructive interference*.

Electrons can also be referred to as *coherent* or *incoherent*. In this terminology electrons are thought of as waves. Coherent electron waves are in-phase after interaction with matter, while incoherent electron waves are out of phase.

3.5.2 Laue's diffraction equations

Max von Laue was a German physicist who in 1913 was credited for the idea that diffraction can be used to analyse the atomic structure of materials [56]. Von Laue also deduced equations governing diffraction. For this work he received the Nobel prize in Physics in 1914.

Von Laue argued that the diffracted waves are in phase if the path difference between waves scattered by adjacent scattering centers is a whole number of wavelengths. Figure 3.6 shows two scattering centers/atoms positioned at B and C. The distance between the atoms is a, the incident angle is θ_1 and the refracted angle θ_2. The path difference is AB-CD. Basic trigonometry gives:

$$\frac{AB}{a} = \cos\theta_1 \Rightarrow AB = a\cos\theta_1 \tag{3.10}$$

$$\frac{CD}{a} = \cos\theta_2 \Rightarrow CD = a\cos\theta_2 \tag{3.11}$$

By Laue's argument the path difference, AB-CD, should be a whole number of wavelengths. Consequently, Laue's equations in three dimensions are:

$$a(\cos\theta_1 - \cos\theta_2) = h\lambda \tag{3.12}$$

$$b(\cos\theta_3 - \cos\theta_4) = k\lambda \tag{3.13}$$

$$c(\cos\theta_5 - \cos\theta_6) = l\lambda \tag{3.14}$$

A diffracted beam is produced when all three Laue equations are satisfied simultaneously [56]. The letters *hkl* are equivalent to the Miller indices (h k l) of the diffracting crystal planes.

3.5.3 Bragg's law

A simpler approach is usually used to describe diffraction. Sir William H. Bragg and Mr. W. Lawrence Bragg (father and son) proposed in 1913 that waves behave as if they were reflected off atomic planes [56]. The Braggs received a Nobel Prize in Physics in 1914 for their work, a year after von Laue.

Figure 3.7 shows Braggs' approach. Two incident waves are reflected off an upper and lower plane. The path difference is AB + BC, where:

$$AB = BC = d\sin\theta \tag{3.15}$$

where d is the interplanar spacing and θ the angle of incidence.
By this approach, constructive interference is described by Bragg's law as:

$$2d\sin\theta_B = n\lambda \tag{3.16}$$

where θ_B is the Bragg angle, n an integer and λ the wavelength.
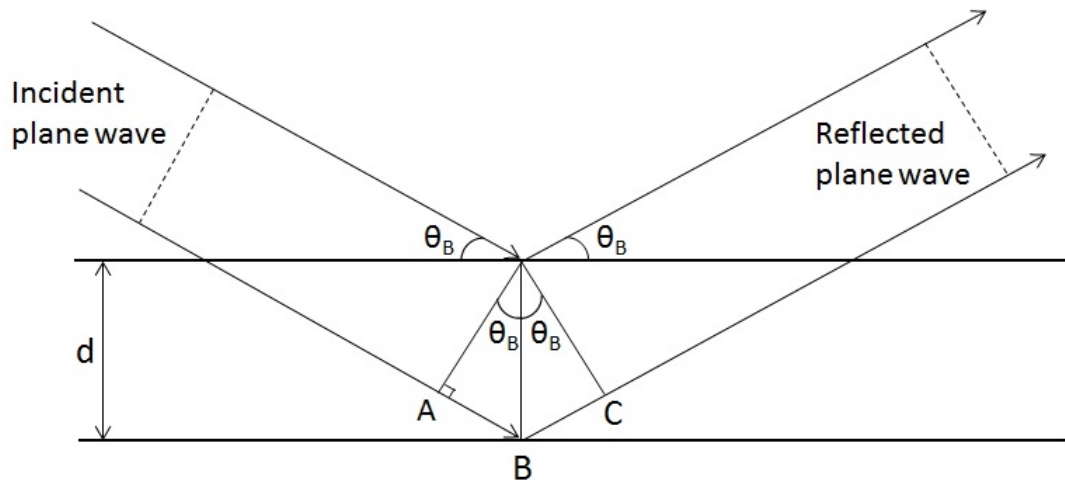
Figure 3.7: A geometrical illustration of Bragg diffraction. Two incident plane waves are reflected off an upper and lower plane. The wave reflected off the lower plane travels a distance AB + BC longer than the wave reflected off the upper plane. The Bragg angle of reflection is indicated with θ_B and the interplanar spacing with d.

It is important to remember that Bragg's law, although mathematically correct, is physically incorrect [56]. Physically, Bragg's law describes reflection not diffraction. The justification in using Bragg's law is however that it can be derived as a special form of the Laue equations, which do describe diffraction.

3.5.4 Kinematic and dynamic scattering

A wave passing through a sample can be scattered by one or several scattering centers. If the wave is scattered by one plane the process is referred to as *kinematic scattering*. The atomic structure of the material can be found by analysing the kinematically scattered intensities. Dynamic effects arise if the already scattered wave is in an ideal orientation to be Bragg scattered once more by an adjacent scattering center. The wave can in this way be scattered multiple times. The probability of dynamic scattering increases with the thickness of the sample [56]. The sample should not be thicker than the mean free path of the wavelength used. The mean free path is dependent on the density of atoms in the unit cell, the scattering angle and the atomic weight of the material [56]. The mean free path of the electrons is ≈10nm. The effect of dynamic scattering is more pronounced in electron diffraction rather than X-ray diffraction since interaction between electrons and matter is stronger than interaction between X-rays and matter.

Kinematic scattering theory applies to perfect crystals. Diffraction intensity can be expressed by the atomic scattering factor, $f_i(\theta)$ and the structure factor, $F(\theta)$. $f_i(\theta)$ is a measure of the scattering amplitude of a wave scattered by one single atom. $F(\theta)$ is the scattering factor for a unit cell. Intensity of the scattered wave is expressed by the scattering factor $F(\theta)$ as:

$$I = |F(\theta)|^2 = |\sum_i^{\infty} f_i e^{2\pi i (hx_i + ky_i + lz_i)}|^2 \tag{3.17}$$

where *hkl* indicates the scattering plane and x_i, y_i, z_i are the positions of the atoms in the unit cell.

Depending on the atom positions in the unit cell, the structure factor and hence the intensity can be 0 for certain reflections. These reflections are called *forbidden* or *extinct*. For example, a body-centered cubic unit cell has two lattice points, (0, 0, 0) and $(\frac{1}{2}, \frac{1}{2}, \frac{1}{2})$. It can be shown that the structure factor, $F(\theta)$, for this type of unit cell is:

$$F(\theta) = f(1 + e^{\pi i (h+k+l)}) \tag{3.18}$$

meaning that $F(\theta) = 2f$ if $h + k + l$ is even, and $F(\theta) = 0$ if $h + k + l$ is odd.

Chapter 4

Experimental methods

4.1 Instrumentation

4.1.1 Laser diffraction

Laser diffraction is a technique for particle size determination from a few nanometers to a few millimeters. Figure 4.1 shows the basic principles of the instrument. In this measurement method a laser is focused on a sample. The angle to which the light is scattered depends on the particle size and the wavelength of the laser light. The diffraction system measures the intensity of scattered light as a function of the scattering angle. Large particles give small scattering angles, while small particles give large scattering angles.

Red laser light with a wavelength of 633 nm is usually used. Resolution of small particles (<1μm) can be improved by using a blue laser with a wavelength of 470 nm. The particle size distribution can be obtained from the scattering pattern by utilizing Mie theory or Fraunhofer approximation. The Mie theory is a general solution to Maxwell's equations for scattered light in the "far field solution" where the distance from the particles to the detector is very large compared to the wavelength of the light. Fraunhofer approximation is, as the name suggests, one of the approximations to Mie theory. In contrast to the Mie theory, the Fraunhofer approximation does not require any optical property information, and is therefore the preferred choice. The Fraunhofer approximation can however sometimes lead to incorrect results.

In this work, Cilas 1180 Particle size analyser was used. The instrument utilizes a red laser light with a wavelength of 633 nm and can measure particles sizes in the range 40nm - 2.5mm in wet or dry dispersions. Both differential and cumulative volume distributions are reported (see section 3.3.1 for an explanation of particle size distributions).
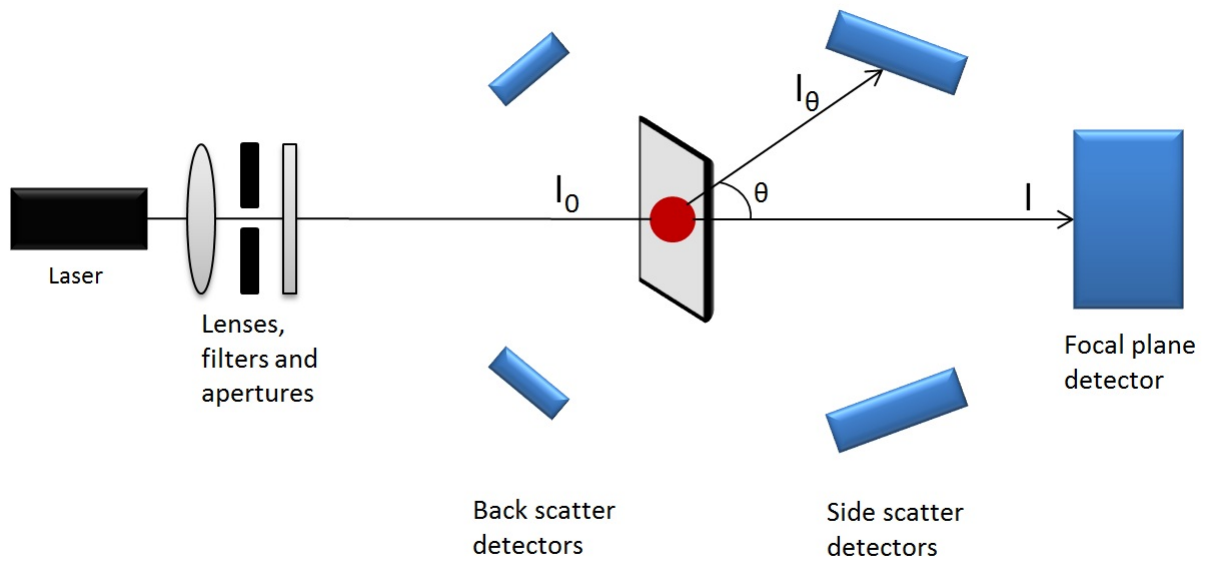
Figure 4.1: Basic principles of light scattering instruments are illustrated. The laser emits light which is modified by lenses, filters and apertures, before it hits a particle in the sample with intensity I_0. The light is scattered by the particle to an angle θ, and the intensity I_θ is recorded by one of the detectors.

4.1.2 Dynamic light scattering

Dynamic light scattering is a quick, non-invasive, low-volume technique for particle size determinations from a few nanometers to a few micrometers. Figure 4.1 shows the basic principles of the instrument. The particle size can be measured due to the Brownian motion of particles. Brownian motion is random movement of particles or molecules in suspensions where the speed depends upon particle size and the mediums viscosity. When a laser is focused on a sample, the light scattering intensity will change with time based on how the particles move. In dynamic light scattering the time dependent fluctuations in scattering intensity are measured in order to determine the translational diffusion coefficient and subsequently the particle radius using the Stoke-Einstein law:

$$a = \frac{kT}{6\pi\eta D} \tag{4.1}$$

where a is the particle radius, k the Boltzmann's constant, T temperature in Kelvin, D the diffusion coefficient and η the medium's viscosity.

The particle size is obtained through a correlation function. Here, the signal from the intensity fluctuations is correlated to find the diffusion rate, and from that calculate

the particle radius. The parameters obtained by this method are the mean size of particles, the width distribution and the size distribution.

In this work, a Malvern Zetasizer Nano ZS is used. The instrument utilizes a backscatter technology where the scattering volume and the focus position in the cell can be adjusted according to particle concentration. The instrument can measure particle sizes in the range 0.3nm - 10μm. The differential cumulative distribution is reported (see section 3.3.1 for an explanation of particle size distributions).

4.1.3   X-ray diffraction

X-ray diffraction, XRD, is an effective method for determination of the crystal structure of materials. X-rays are generated when high energy electrons hit a target. This method gives rise to both continuous and characteristic X-rays. The characteristic X-rays are generated if the incident electron has sufficient energy, a K-shell electron can be ejected through an inelastic collision. The K-shell vacancy can be filled by an outer electron from the L- or M-shell and the excess energy is emitted as an X-ray. This two step process is called *X-ray fluorescence*. A monochromatic radiation is generated by filtering out parts of the spectrum. Usually the Kα_1-line (L$_1 \rightarrow$ K) is used as the monochromatic X-ray radiation. However, the wavelength difference between Kα_1 and Kα_2 (L$_2 \rightarrow$ K) is sometimes so small that both lines are used. In this context, they are referred to as the Kα *doublet*. X-ray beams incident on a crystalline sample will be diffracted by Bragg's law as explained in section 3.5.3 on page 34. Kinematic theory applies to X-ray diffraction, see section 3.5.4 on page 35.

In this work a Bruker D5000 with Cr-Kα_1 monochromatic radiation and Inel Equinox 5000 with Co-Kα_1 were used. The acquired diffractograms were analysed with the software package DIFFRAC PLUS Evaluation (Bruker D5000) and JADE (Inel Equinox 5000) and compared to the information provided by the International Centre for Diffraction Data.

4.1.4   X-ray fluorescence spectrometry

X-ray fluorescence spectrometry, XRF, is a widely used technique in element analysis. As described in section on X-ray diffraction, characteristic X-rays are emitted when high energy electrons hit a target or a sample. The process is called X-ray fluorescence, and in X-ray fluorescence spectrometry these characteristic X-rays are used to identify the elements in the sample. The X-ray photons can be either analysed by an energy-

dispersive analysis where the energy of the photons is detected or by a wavelength dispersive analysis where the wavelength of the photons is detected. The intensity of the radiation is related to the amount of each element in the material.

In this work an Oxford Instruments Twin-X instrument with energy-dispersive detectors was used. The uncertainty in the measurement is 0.001-0.01wt%, which is considered to be insignificant.

4.1.5 Transmission electron microscope

A transmission electron microscope, TEM, is an advanced instrument which makes it possible to image crystal structures down to the atomic level and obtain diffraction patterns down to a few nanometers. The instrument utilizes a high-energy electron beam which is transmitted through a very thin sample (less than a few hundred nanometers). The transmitted beam is in this case scattered elastically in a forward direction. Elastic scattering is usually coherent [56].

A reliable electron source is crucial for the performance of the microscope. There are two types of electron sources, thermionic and field-emission. A thermionic source emits electrons when heated, while a field-emission source emits electrons when there is a large potential difference between the source and the anode. In this context the electron source is often referred to as the cathode. A lanthanum hexaboride crystal, LaB_6, is a common thermionic source in a TEM. Fine tungsten needles are commonly used as a field-emission source. The electrons emitted from the source are accelerated through a potential difference (100-400kV) towards the anode, after which the electron beam enters the TEM-column. High vacuum throughout the column is essential to minimize contamination. The column contains electromagnetic lenses, specimen holder, apertures and deflector coils. The performance of the electromagnetic lenses in a TEM can be compared to convex (converging) lenses in a visible light microscope. One significant difference is however that the lenses in a TEM can vary in strength. The imaging device in a TEM can be a fluorescent screen, photographic film or a CCD camera. Whether an image or a diffraction pattern is seen on the screen depends on whether the lenses are set to focus on the image plane or the back focal plane. Figure 4.2 shows a ray diagram for an electron beam passing through a sample, and the location of the back focal and image plane. Several apertures are positioned throughout the column. They control which electrons can pass from one lens to the next and are in that sense very important in various imaging and diffraction techniques.
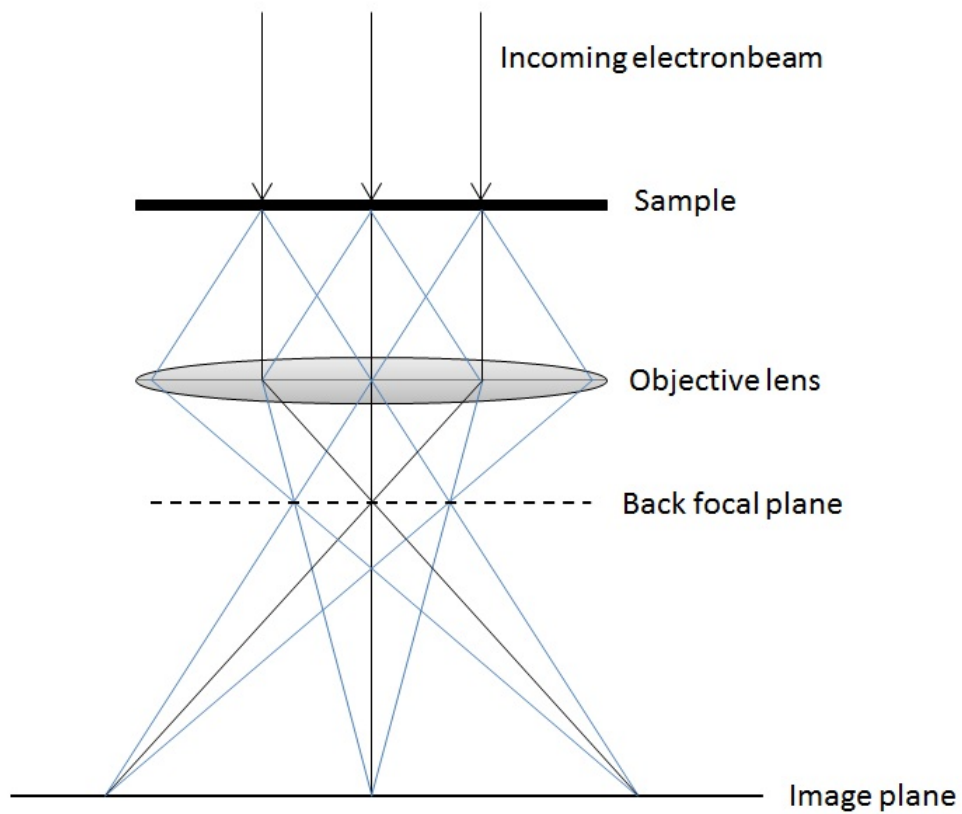
Figure 4.2: A complete ray diagram for an electron beam going through a thin sample. The diffraction pattern is formed in the back focal plane while an inverted image is formed in the image plane.

Selected area diffraction

Selected area diffraction, SAD, is a common technique used to determine lattice spacings from electron diffraction patterns. Selected area aperture is located below the sample holder on the TEM column and is typically in the range of 1-10μm in diameter [56]. The sample is illuminated with a parallel beam which is focused in the back focal plane to form a diffraction pattern on the screen. Each reflection corresponds to a crystal plane in real space. The distance between the planes in the crystal can be found by using the relationship [57]:

$$\frac{R}{L} = \tan 2\theta_B \approx 2 \tan \theta_B \approx 2 \sin \theta_B \tag{4.2}$$

where R is the distance between adjacent reflections in the diffraction pattern, L the camera length and θ_B the Bragg angle.

Combination of this equation with Bragg's law given in equation (3.16) gives:

$$\frac{R}{L} = \frac{\lambda}{d} \Rightarrow d = \frac{\lambda L}{R} \tag{4.3}$$

where λ is the wavelength of the electrons, L the camera length and R the distance between adjacent reflections in the diffraction pattern.

In this work, a JEOL JEM 2000FX with an energy-dispersive detector was used. This instrument has a LaB$_6$-cathode and was operated at an acceleration voltage of 200kV.

4.1.6 Scanning electron microscope

A scanning electron microscope, SEM, is a diverse instrument which can give information about surface topography and morphology, chemical element composition as well as grain size and orientation. The principles of the SEM have many similarities with the TEM. A high energy electron beam is generated, but the potential difference between the electron source (cathode) and the anode is lower (5-20kV) than in the TEM. The electron beam can be modified throughout the SEM-column by electromagnetic lenses and deflection coils, and is used to scan across the surface of the sample. High vacuum is also required. Interactions between the high energy electrons and surface atoms give rise to various signal types like secondary electrons, backscattered electrons, Auger electrons, X-rays and cathodoluminescence. The signals are collected and interpreted by different types of detectors.

In this work two instruments with different electron sources were used, Hitachi Table-top TM3000 with a tungsten thermionic source and a FEI Quanta 2000 with a field-emission source. Both instruments were operated at an acceleration voltage of 15kV. The FEI Quanta 2000 was also operated in a low-vacuum mode with a water pressure of 40Pa.

4.1.7   Specific surface area measurements

The specific surface area of a solid material can be found by the volumetric method. A known amount of a solid material is inserted into a chamber of known volume. Then, a known volume of a gas is introduced. The amount of gas adsorbed can be found by measuring the pressure drop. Depending on the isotherm, the volume of a monolayer of the adsorbed gas can be found either by equation 3.4 or equation 3.5 on page 28. Only gas molecules that are small enough to enter the pores and surface imperfections may be used to determine the surface area of a solid material [54]. Nitrogen gas, N_2, is usually used due to its small size, low cost and inert nature. One N_2-molecule occupies a surface area of $16, 2 \cdot 10^{-20} m^2$, meaning that the surface area of the solid material can easily be found when the monolayer volume of the adsorbed gas is determined. The linearization of the isotherms, determination of the monolayer volume as well as the calculation of the surface area is usually done with the software provided by the manufacturer.

In this work Micromeritics Tristar was used with the software Tristar 3000 v.6.07. All surface areas were analysed by BET theory. The uncertainty in the measurement is $0.01 m^2/g$, which is considered to be insignificant.

4.1.8   Thermogravimetry

Thermogravimetric analysis, TGA, is a technique were a sample's mass change is measured as the sample is heated, held at constant temperature and/or cooled. The heating rate is usually constant. As the sample is heated various components are decomposed and the mass change is measured. Thus, the technique relies on high precision measurements of heating rate, temperature and mass change.

In this work a Mettler Toledo TGA/DCS 1 was used. Depending on the sample, various temperature intervals and heating rates can be programmed. All the TGA methods used are listed in appendix A.

4.1.9 Refractive index measurements

A refractometer measures the index of refraction of a liquid. Snell's law describes the relationship between the angles of incidence and refraction:

$$\frac{\sin \theta_1}{\sin \theta_2} = \frac{n_2}{n_1} \tag{4.4}$$

where θ_1 and n_1 are the angle of incidence and the refractive index for medium 1, and θ_2 and n_2 are the angle of incidence and the refractive index of medium 2.

The basic principle utilized in a refractometer is that if the angle of incidence, the angle of reflection as well as one refractive index are known, the unknown refractive index can be found by Snell's law.

In this work an Index instruments PTR46 was used. The uncertainty in the measurement of the refractive index is ± 0.0001.

4.1.10 Sputter deposition

Sputtering is a common technique for the deposition of thin films. In sputtering deposition high energy gas particles hit a solid surface (the target) which ejects atoms. The atoms from the target can than be deposited on a surface of a substrate. The sputtering gas is often an inert gas and the atomic weight of the sputtering gas should be close to the atomic weight of the target. Argon is usually used for heavy element targets.

In this work the α-Al$_2$O$_3$ and YSZ single crystals were coated with a platinum layer at the electron microscopy lab at the Department of Molecular Biosciences. They have a Cressington 308R coating system.
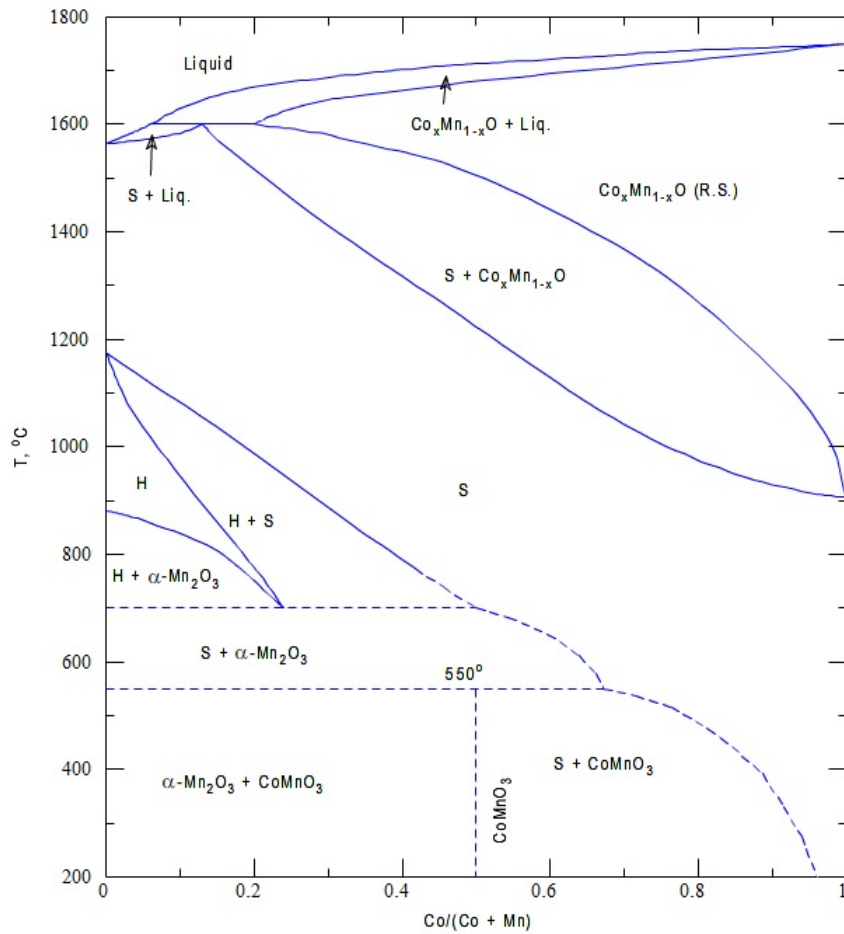
Figure 4.3: Phase diagram for the cobalt-manganese system. H refers to the manganese oxide Mn_2O_3 (hausmannite) and S refers to the spinel structure [58].

4.2 Catalyst synthesis

4.2.1 Synthesis of $Co_{3-x}Mn_xO_4$ spinel catalyst by coprecipitation

The main objective of this experiment was to synthesise a $Co_{3-x}Mn_xO_4$ catalyst with a spinel structure. Figure 4.3 shows the phase diagram for the Co-Mn-O system [58]. A spinel phase can be formed over a wide range of Co/(Co+Mn) ratios and temperatures. In this experiment a Co/(Co+Mn) ratio of 0.5 was chosen. For this ratio, the spinel phase forms above 700°C and corresponds to $Co_{1.5}Mn_{1.5}O_4$.

Coprecipitation is a suitable method for catalyst synthesis when the ionic radii are of similar size. It is documented that the ionic radius is not fixed, but depends on several parameters; for example coordination number, spin state and the degree of symme-

try in the crystal structure [59]. The ionic radii of Mn^{2+} and Co^{2+} can be estimated by taking the mean interatomic distances of Mn^{2+}-O^{2-} and Co^{2+}-O^{2-} and subtract the O^{2-}-ion radius. The Mn^{2+}-O^{2-} distance is 210.0pm and the Co^{2+}-O^{2-} distance is 202.1pm [60]. The crystal radius of the O^{2-}-ion is reported to be 126pm [61]. The Mn^{2+} radius is then calculated to 84.0pm and the Co^{2+} radius to 76.1pm. This shows that the ionic radii of Mn^{2+} and Co^{2+} are of similar size.

The coprecipitation is carried out by mixing of a Mn/Co-solution with NH_4HCO_3. The amount of precipitate produced is dependent on several conditions. One of them is the pH at which the precipitation is carried out, or i.e. the ratio between the metal solution and the base (NH_4HCO_3). The extent of precipitation can be measured in an indirect way by finding the amount of Mn and Co that has not precipitated. A 0.5M Mn/Co solution corresponds to the chosen Co/(Co+Mn) ratio of 0.5. This solution needs to be prepared prior to the coprecipitation.

The chemicals used for the preparation of the 0.5M Mn/Co standard solution were:
• Manganese nitrate hexahydrate ($Mn(NO_3)_2 \cdot 6H_2O$), 98%+, Alfa Aesar • Cobalt nitrate hexahydrate ($Co(NO_3)_2 \cdot 6H_2O$), 99.5%, Alfa Aesar.

The molecular mass of $Mn(NO_3)_2 \cdot 6H_2O$ and $Co(NO_3)_2 \cdot 6H_2O$ was calculated to be 287.04 g/mol and 291.03 g/mol, respectively. For a 0.5M Mn/Co-nitrate standard solution 286.8g of $Mn(NO_3)_2 \cdot 6H_2O$ and 291.2g of $Co(NO_3)_2 \cdot 6H_2O$ was weighted into a 2L volumetric flask and water added to the 2L-mark. The solution was analysed by XRF in order to check the concentrations of Mn and Co. The XRF results showed that the concentration of Mn was 0.4276M and the concentration of Co was 0.3469M. Tracer amounts of Ce were also measured to 0.0037M. This is believed to be due to contamination. 0.5M concentrations of both Mn and Co were expected. Both nitrates are hygroscopic meaning that they can absorb water molecules from the surrounding environment. A TGA of both nitrates was performed in order to check the number of water molecules pr. nitrate molecule. Method 1 was used, see appendix A and section 5.1 for a result overview. The Mn/Co solution was anyhow used in the following coprecipitation.

The chemicals used for the coprecipitation were: • Mn/Co-nitrate solution • 2M standard solution of ammonia bicarbonate (NH_4HCO_3).

	1	2	3	4	5	6	7
metal	100	90	80	70	60	50	37.5
base	50	60	70	80	90	100	112.5

Table 4.1: Metal and base volumes. All volumes are in mL.

The amount of precipitate is dependant on the metal:base ratio. For that reason, the metal:base ratio which would give a maximum precipitate amount was found first. Metal:base ratios from 2:1 to 1:3 and a total precipitate volume of 150ml were chosen for this part of the experiment. 7 precipitate solutions were made in the given ratio range. Table 4.1 shows the volumes of metal and base solutions that were tested. For each precipitation, the metal and base solutions were heated up to 60°C prior to mixing. When the temperature reached 60°C, the two solutions were mixed simultaneously in a larger beaker. A temperature drop of ≈10°C was observed. The precipitate solution was stirred with an electrical stirrer (Heidolph RZR1). The top of the beaker was covered with aluminium foil in order to minimize heat loss and the temperature was held at approximately 60°C. The aging time was 30 minutes. After aging, the precipitate solution was filtered and the liquid phase was analysed by XRF to check the amount of Mn and Co that had not precipitated. The XRF results showed that the maximum precipitate amount was achieved when solutions 4-7 were used (see section 5.1 for results overview). Solution 5, with a metal:base ratio of 2:3, was chosen for the precipitation of the $Co_{3-x}Mn_xO_4$ catalyst.

The catalyst coprecipitation was carried out with larger metal and base volumes, but the metal:base ratio was kept at 2:3 as for solution 5, table 4.1. 1L of the metal solution was used along with 1.5L of base solution. The coprecipitation itself was carried out in the same way as the 7 precipitate solutions described above. One difference was, however, that the beaker in which the metal and base solutions were mixed was first preheated by heating 2.5L of water up to 60°C. The water was removed prior to the mixing of metal and base. In this way, no temperature drop was observed after mixing. The precipitate was filtered after aging and dried in a Termaks heating cabinet at 81°C for 24h. After drying, the product was ground and calcined at 700°C, and then re-ground and re-calcined at 900°. Figure 4.4 shows a more detailed temperature overview for the two calcinations. The final catalyst powder was analysed by XRD. The XRD showed that the catalyst powder contained two different phases. The powder was therefore again ground and calcined at 1100°C by otherwise the same temperature scheme as shown in figure 4.4 (b). Another XRD of the catalyst powder was performed. Also, the powder was first analysed by XRD with a Cu-Kα_1 radiation.

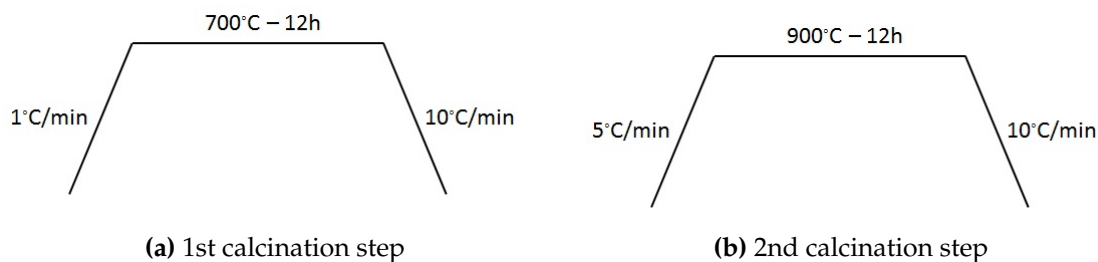**(a)** 1st calcination step   **(b)** 2nd calcination step

Figure 4.4: (a) The first and **(b)** the second calcination steps of the $Co_{3-x}Mn_xO_4$ catalyst powder showing the heating/cooling rates, time and temperature for the heating stage.

The acquired diffractogram contained a lot of noise due to fluorescence of manganese by the Cu-anode. The measurement was therefore repeated with Co-Kα radiation.

4.2.2   Synthesis of $LaMnO_3$ perovskite catalyst by sol-gel method

The sol-gel method, rather than coprecipitation, was chosen as the synthesis route for the $LaMnO_3$ catalyst with a perovskite structure. This is due to the large difference in ion sizes between the La^{3+}-ion and Mn^{2+}-ion. The ionic radius of La^{3+} is calculated to 118.1pm by the same method described in section 4.2.1. The ionic radius of Mn^{2+} is 84pm.

Citric acid was chosen as the chelating agent, while ethyleneglycol was chosen as the polyhydroxy alcohol. Kangvansura documented in her master thesis that ratios between metal and citric acid should be 1:3, and ratios between ethylene glycol and citric acid should be 2:3 [62].

Chemicals used for the synthesis of the $LaMnO_3$ catalyst were: • Citric acid monohydrate ($C_6H_8O_7 \cdot H_2O$), 99.5-100.5%, Merck • Ethylene glycol ($C_2H_6O_2$), $\geq$ 99.5%, Merck • Lanthanum nitrate hexahydrate ($La(NO_3)_2 \cdot 6H_2O$), 99.9%, Alfa Aesar • Manganese nitrate hexahydrate ($Mn(NO_3)_2 \cdot 6H_2O$), 99.9%, Alfa Aesar

A TGA of lanthanum nitrate hexahydrate was performed first to check the correct amount of H_2O pr.$La(NO_3)_2$. Method 1 was used, see appendix A. The TGA showed that the number of H_2O pr. $La(NO_3)_3$ was 6, as stated by the manufacturer (see section 5.1 for result overview).

At a later point an ink will be made out of the produced catalyst powder. For that purpose around 60g of catalyst is needed. Table 4.2 summarizes the amounts needed

Compound	Amount (mol)	Molecular mass ($\frac{g}{mol}$)	Mass (g)
$La(NO_3)_2 \cdot 6H_2O$	0.25	241.85	108.25
$Mn(NO_3)_2 \cdot 6H_2O$	0.25	287.04	71.76
Citric acid	0.75	210.14	153.0
Ethylene glycol	1.125	62.07	69.8

Table 4.2: Amounts, molecular mass and mass of all the compounds needed to produce 60g of $LaMnO_3$ catalyst.

of each chemical compound according to the ratios stated by Kangvansura. For the experiment, 108.2g of $La(NO_3)_2 \cdot 6H_2O$ and 71.9g of manganese $Mn(NO_3)_2 \cdot 6H_2O$ were first weighted into a beaker and dissolved in 500ml water. The beaker was put on a hotplate and the solution stirred with a magnetic stirrer to aid the dissolvation of the nitrates. 154g of citric acid followed by 70.9g of ethyleneglycol was added when the temperature reached 30°C. Citric acid acts as a chelating agent and forms randomly distributed metal-cation complexes, while a polyesterification is carried out by addition of ethylene glycol. The desired temperature was around 60°C, so the beaker was at this point covered with aluminium foil in order to minimize heat loss. After 3h (corresponding to the gelation time), the temperature was turned up to 100°C for 18h (aging). During this step an organic network of randomly distributed metal ions is formed and water evaporated. After the aging, a small sample of the gel was analysed by TGA to find the decomposition temperature of the organic network. Method 2 was used, see appendix A. It was found that the decomposition temperature was at approximately 210°C (see section 5.1 for result overview).

The decomposition of the organic network will result in NO_x gas emission. To minimize the emission of the NO_x gases the gel was decomposed in four batches. First, the gel was dried in a Termaks heating cabinet at 81°C for 18h. The dried gel was divided into four batches and each batch was heated up to 230°C for 1h. Another TGA measurement, by method 3, was performed to check if all the organic network had decomposed. The catalyst powder was then ground and calcined at 700°C, and re-ground and re-calcined at 900°C. A more detailed temperature scheme is shown in figure 4.5. The produced powder was analysed by XRD with Cr-Kα_1 radiation.

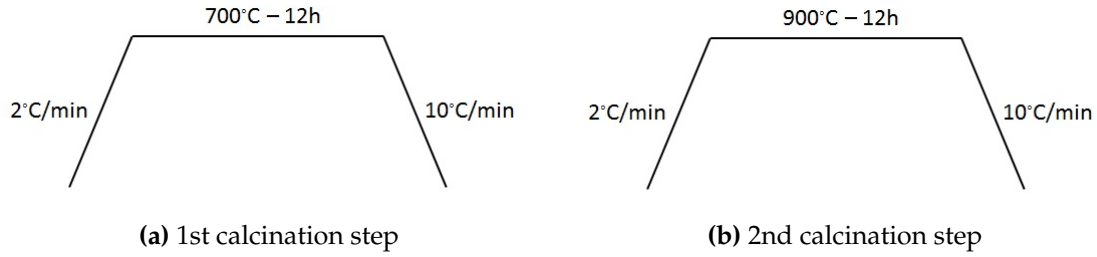**(a)** 1st calcination step   **(b)** 2nd calcination step

Figure 4.5: (a) The first and **(b)** the second calcination steps of the LaMnO$_3$ catalyst powder showing the heating/cooling rates, time and temperature for the heating stage.

4.3   Deposition and characterization of reference layer

A reference layer is needed to mark the original interface between the support and the catalyst layer. The reference layer should contain small crystallites, covering a fraction of the surface. This can be achieved by depositing a uniform layer of a few nanometers by sputtering and sinter at some temperature. Furthermore, it is important that the reference layer particles do not drift around the surface at 900-1000°C since the catalyst and the support will be tested under high-temperature conditions. The melting point of platinum is 2041K (1768°C), while the melting point of gold is 1337K (1064°C). Due to its higher melting point, platinum rather than gold was chosen as the reference layer.

Sintering is a strongly temperature dependent process. Surface diffusion is the underlying mechanism. It is intuitively understandable that diffusion becomes faster when the temperature gets closer to the melting point of the material. Hüttig and Tamman temperatures are directly related to the melting point and indicate at which temperature sintering may occur [63]. The Hüttig temperature defines the onset of mobility at defects, while the Tamman temperature defines the onset of mobility in the bulk. Hüttig and Tamman temperatures are semi-empirical where the recommended relations are:

$$T_H = \frac{T_{melt}}{3} \tag{4.5}$$

$$T_T = \frac{T_{melt}}{2} \tag{4.6}$$

where T$_H$ is the Hüttig temperature, T$_T$ the Tamman temperature and T$_{melt}$ the melting temperature in Kelvin.

By equation (4.5) and (4.6) the Hüttig and Tamman temperatures for platinum are respectively 681K and 1021K, which corresponds to 408°C and 748°C. The sintering temperatures were thus chosen to be 430°C, 550°C, 650°C and 770°C.

This experiment included two parts. The main objective of the first part was to establish the optimum sintering temperature. For this purpose, four single crystals of α-Al$_2$O$_3$ and YSZ were coated with a 10nm platinum layer by sputter deposition. The samples were sintered in a tube furnace starting from room temperature, held 4h at the sintering temperatures described above, and cooled to room temperature before they were taken out. It was not possible to programme the heating and cooling rates on the furnace that was used.

The main objective of the second part of the experiment was to establish the correct platinum layer thickness. Single crystals of α-Al$_2$O$_3$ and YSZ were this time coated with a 2.5nm and 5nm platinum layer by sputter deposition and sintered by the same method as described above at 770°C.

The size and shape of the platinum particles on α-Al$_2$O$_3$ and YSZ-single crystals was studied by SEM.

4.4 Preparation of catalyst ink and deposition of catalyst layer on the single crystals

Before deposition on the reference samples, an ink needs to be made out of the catalyst powder. The ink can be made by the same procedure used in tape casting [64]. Tape casting is a method used to manufacture thin tapes from a slurry. Common additives in a tape casting process include solvent, deflocculant, binder and plasticiser. In addition, a surfactant may sometimes also be used [65]. Dispersion of particle aggregates and powder agglomerates can be accomplished by wet milling of the solvent and the dispersant with the catalyst powder. The dispersion step is essential in order to obtain uniform shrinkage of the ink without coarse grains.

The slurry can be both aqueous or non-aqueous, depending on the solvent used. Aqueous slurries are more health and environmental friendly, while non-aqueous slurries have advantages related to powder dispersion and slurry drying. Organic solvents have a lower boiling point and a lower heat of vaporization than water. Non-

aqueous slurries will therefore dry faster than aqueous slurries. A faster drying process is favourable because it limits degradation of other additives.

Menhaden fish oil is a mixture of various triglycerides and is commonly used as a deflocculant in non-aqueous systems [65]. Deflocculation is in this case promoted by steric repulsion. Particle charging is the main deflocculation mechanism in aqueous systems. The binder is usually of high molecular weight and must be dispersible in the slurry. Another requirement for the binder is that it should have a clean thermal elimination over a wide temperature range in order to avoid sudden gas evolution. The plasticiser should have a lower vapour pressure than the solvent so that it is retained after drying. Two plasticizers are commonly used to reduce the rate of gas evolution when the organics are removed.

Dispersing and mixing are usually accomplished by a two-step milling process. This is done in order to reduce the scale of inhomogeneity in the slurry without degrading the high molecular weight binder molecules [64]. First, the solvent, dispersant and powder are milled. Than, the binder and plasticisers are added and the milling continues.

Chemicals used for the catalyst ink preparation were: • Trichloroethylene (C_2HCl_3), $\geq$ 99.5%, Sigma Aldrich • Absolutt alkohol prima, 2% metylisotylketone, Arcus kjemi • Fish oil from menhaden, Sigma • Polyvinyl butyral, Butvar B-75, Solutia • Polyethylene glycol 200 ($HO(C_2H_4O)_nH$), Merck • Di-n-octyl phthalate ($C_{24}H_{38}O_4$), $\geq$ 99.5%, Sigma Aldrich

The desired composition of the catalyst powder, solvents, deflocculent, binder and plasticiser for the Co-Mn-O ink is summarized in table 4.3 and for the $La_{0.969}Mn_{0.93}O_3$ ink in table 4.4 [65]. Both catalyst powders were first milled in a planetary mill (Retch PM400/2) at 225rpm along with the solvents and the dispersant for 2.5h. All the liquids were weighted in flasks with corks to reduce evaporation. After 2.5h of milling, the binder and plasticisers were added, and the milling continued for another 2h. 3mm zirconia beads were used for the wet milling.

Co-Mn-O ink: The amount of Co-Mn-O powder was 5.11g. For the first milling step, 2.14g of trichloroethylene, 0.49g of ethanol and 0.09g of mehaden fish oil was added. The powder did not dissolve properly, so another 3.60g of trichloroethylene was added, making it a total of 5.74g of trichloroethylene. For the second milling step, 0.19g

Function	Material	Volume%	Density (g/ml)	Weight%	Weight (g)
Catalyst	Co-Mn-O	27	5.5	62.35	5.11
Solvent	Trichloroetylene	42	1.46	25.75	2.11
Solvent	Ethanol	16	0.78	5.24	0.43
Deflocculent	Menhaden fish oil	1.8	0.93	0.70	0.06
Binder	Polyvinyl butyral	4.4	1.1	2.03	0.17
Plasticiser	Polyethylene glycol	4.8	1.13	2.28	0.19
Plasticiser	Dioctyl phthalate	4.0	0.98	1.65	0.14

Table 4.3: The table shows the volume% of all the additives needed for the preparation of the Co-Mn-O ink [65]. The catalyst density is found for the phase $Co_{1.5}Mn_{1.5}O_4$. Densities for the additives are tabulated values. Weight% is calculated from the density and volume%, while the weight in grams is calculated from the weight% and the weight of the catalyst powder.

Function	Material	Volume%	Density (g/ml)	Weight%	Weight (g)
Catalyst	$La_{0.969}Mn_{0.93}O_3$	27	6.57	66.43	20.15
Solvent	Trichloroetylene	42	1.46	22.96	6.96
Solvent	Ethanol	16	0.78	4.67	1.42
Deflocculent	Menhaden fish oil	1.8	0.93	0.63	0.19
Binder	Polyvinyl butyral	4.4	1.1	1.81	0.55
Plasticiser	Polyethylene glycol	4.8	1.13	2.03	0.62
Plasticiser	Dioctyl phthalate	4.0	0.98	1.47	0.45

Table 4.4: The table shows the volume% of all the additives needed for the preparation of the $La_{0.969}Mn_{0.93}O_3$ ink [65]. All the densities are tabulated values. Weight% is calculated from the density and volume%, while the weight in grams is calculated from the weight% and the weight of the catalyst powder.

polyvinyl butyral, 0.27g polyethylene glycol and 0.18g di-n-octyl phthalate was added. After the second milling, another 3.3g of trichloroethylene was added.

$La_{0.969}Mn_{0.93}O_3$ *ink:* The amount of $La_{0.969}Mn_{0.93}O_3$-powder was 20.15g. For the first milling step, 7.09g trichloroethylene, 1.41g ethanol and 0.27g menhaden fish oil was added. Also here, extra 7.31g of trichloroethylene was added, making it a total of 14.4g of trichloroethylene. For the second milling step 0.56g polyvinyl butyral, 0.63g polyethylene glycol and 0.52g di-n-octyl phthalate was added.

Platinum coating as a referance layer: Four single crystals of α-Al_2O_3 and YSZ were coated with a platinum layer of 5nm, and sintered in a tube furnace started from room temperature, held at 770°C for 4h, and cooled to room temperature.

Catalyst ink coating: The Co-Mn-O and $La_{0.969}Mn_{0.93}O_3$ catalyst inks were painted onto

(a) Co-Mn-O ink

(b) $La_{0.969}Mn_{0.93}O_3$ ink

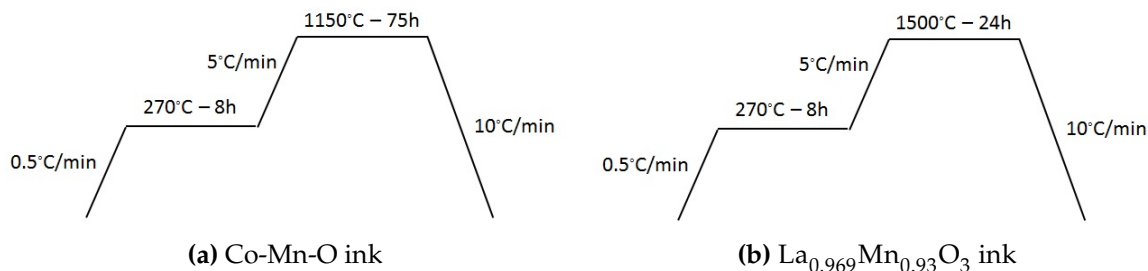**Figure 4.6:** Annealing of samples coated with **(a)** the Co-Mn-O ink and **(b)** the $La_{0.969}Mn_{0.93}O_3$ ink showing the heating/cooling rates, time and temperature for the heating stage.

the platinum coated single crystals of α-Al_2O_3 and YSZ with a small paintbrush. Two layers were painted, one in each direction, to ensure good catalyst ink coverage. The first layer was left to dry for approximately one minute before the second layer was painted on. After both layers had dried, the samples with the $La_{0.969}Mn_{0.93}O_3$ on α-Al_2O_3 were packed in parafilm paper and isostatically pressed (Loomis press, type 1011-3-12-30) to insure good contact between the catalyst ink and the support. Pressure was set at 30 000 psi for 60s. After pressing, the catalyst coating detached from the single crystals when the samples were unpacked. Therefore, no further samples were pressed.

All the samples were put on a ceramic plate. The samples were annealed in two steps to reduce gas evolution during each step. Ultimately, the Co-Mn-O/α-Al_2O_3 samples were annealed at 1150°C for 75h and the $La_{0.969}Mn_{0.93}O_3$/α-Al_2O_3 were annealed at 1500°C for 24h. A more detailed temperature scheme is shown in figure 4.6. Figure 4.7 shows the catalyst coated single crystals after annealing. The catalyst-support interface was analysed with SEM, XRD and TEM. First TEM samples were prepared. The SEM analysis was performed on the TEM-samples. XRD was performed by attaching a sample to the XRD sample holder with Blu Tack.

(a)

(b)

(c)

(d)
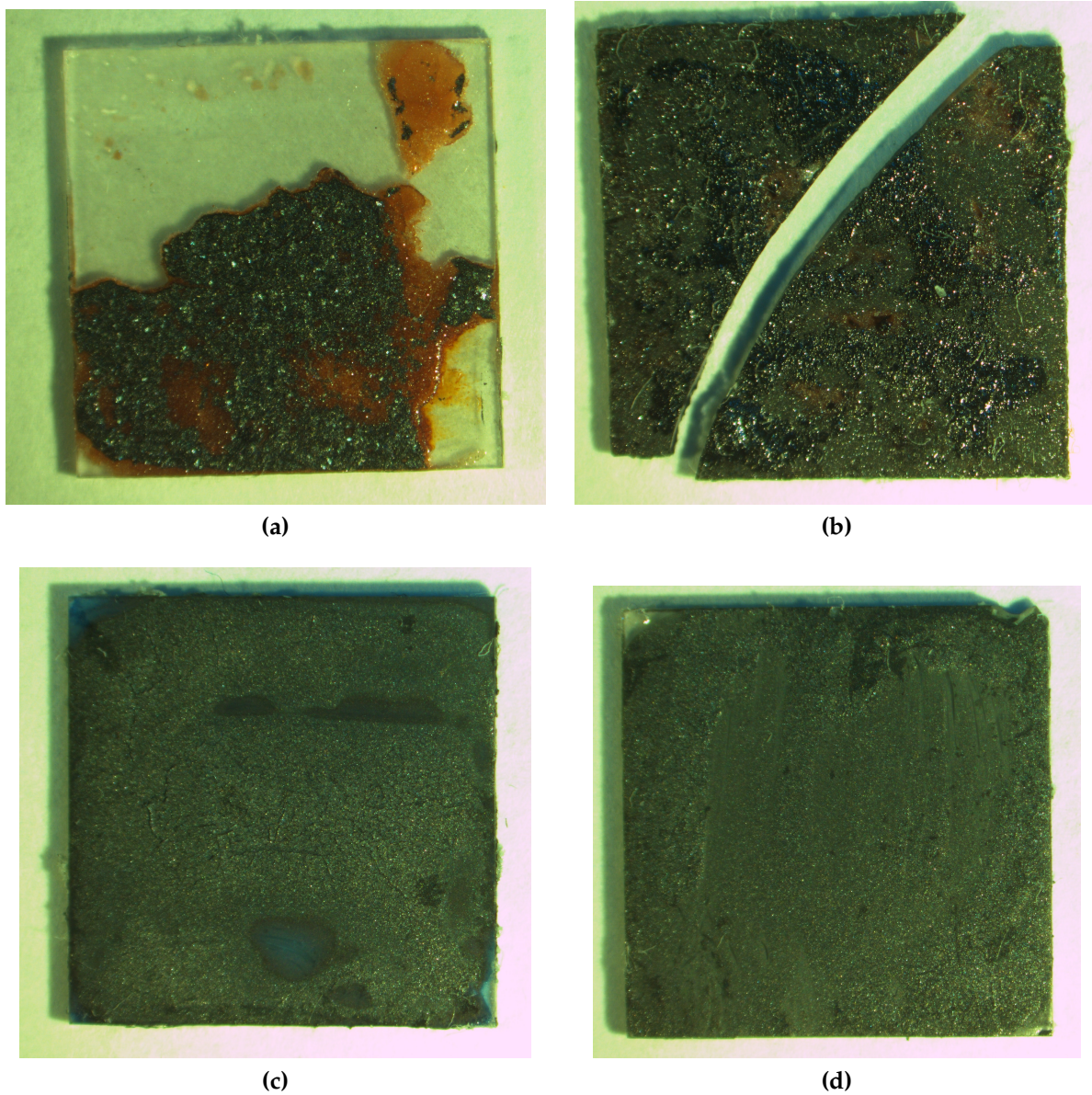
Figure 4.7: Heat treated single crystals of α-Al_2O_3 and YSZ coated with **(a)/(b)** $La_{0.969}Mn_{0.93}O_3$ ink and (**(c)/(d)** Co-Mn-O ink.
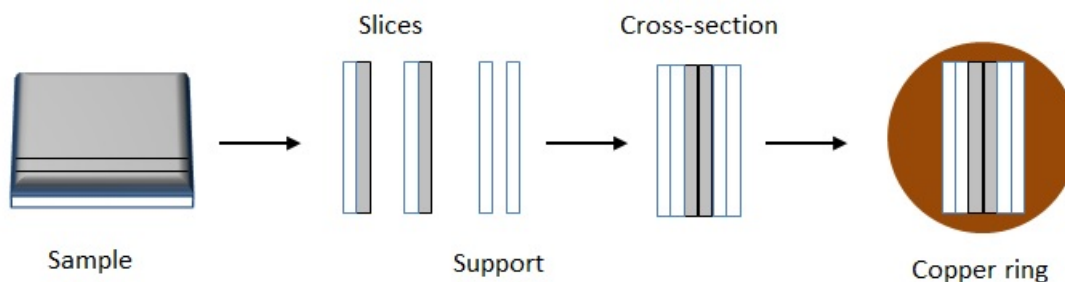
Figure 4.8: An illustration of the sample preparation for TEM-analysis. First 2mm wide slices are cut. The cross-section is made by gluing the two slices along with an additional support layer on each side. The copper ring is glued on the cross-section after grinding.

4.5 TEM characterization

4.5.1 Sample preparation

There are many ways in which a specimen for TEM-analysis can be prepared. The specimen must be electron transparent and, ideally, have a thickness of less than $10\mu m$. The time needed to prepare a TEM-specimen depends on the sample preparation method and the material. It is important that the TEM-specimen is still representative for the material studied after the sample preparation.

Single crystals with the platinum and catalyst layer were first cut into 2mm wide slices with a diamond saw. A cross-section was made by gluing the two slices together with the catalyst layer facing inwards. The cross-section was supported with an additional layer of support material on each side. Figure 4.8 shows an illustration of the sample preparation steps.

Aluminium oxides are in general very hard materials; 9 on the Mohs scale where diamond is set at 10. The cross-sections were initially ground on SiC-paper. This had no significant effect. The samples where then ground on diamond paper (MD Piano 600/1200, Struers) down to $\approx$2-300μm after which the samples where ground with a Multiprep system (Allied). The samples were mounted on a thinning paddle and ground down to $\approx$70μm (paper grain size 30/15μm). Further grinding with the Multiprep system with paper grain size of 6μm took very long time. The samples were therefore ground manually with paper grain size 6μm down to 1μm. The samples were still mounted on the thinning paddle. In this way the samples were ground down to $\approx$20μm. A 3.05mm copper ring with slot size 2mm$\times$1.5mm was glued on
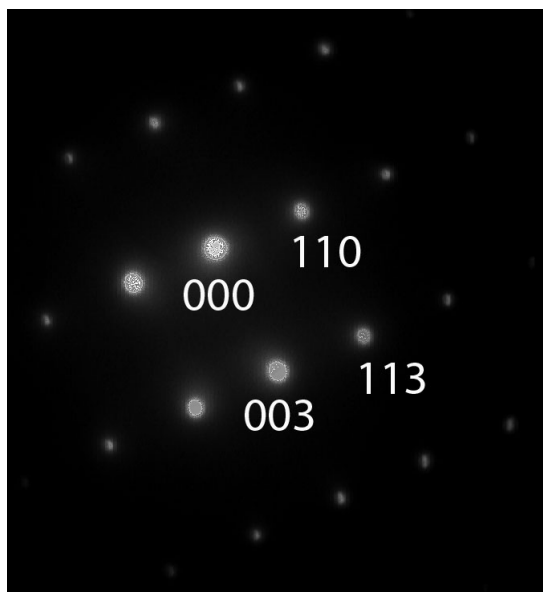
Figure 4.9: Diffraction pattern along the [1 $\bar{1}$ 0] zone axis of the α-Al$_2$O$_3$ support.

the sample. Final thinning of the sample was done by ion milling (Gatan Model 691 Precision). Ar$^+$-ions with an angle of 10° above and below the plane of the sample were used. The acceleration voltage was set at 6keV and the angles were adjusted to 8° above and 8° below the plane of the sample towards the end of the thinning process.

4.5.2 Calibration of the camera length

The camera length was calibrated using a diffraction pattern of the α-Al$_2$O$_3$ support. Figure 5.11 shows the diffraction pattern obtained with a 55cm camera length at eucentric height. The results are summarized in table 4.5. The distances in the diffraction pattern were measured over several reflections, and a mean distance was calculated in order to minimize measurement errors. The calibrated camera lengths were calculated by equation (4.3) and show a quite large deviation from the nominal camera length of 55cm. Moreover, the calibrated camera lengths are dependent on the direction measured in the diffraction pattern. This may be due to astigmatism in the objective lens. Astigmatism is a common lens aberration and it arises because the magnetic field in the electromagnetic lens is not uniform. The d-values of the catalyst layer interface were therefore calculated with both camera lengths, 42cm and 50cm.

hkl	Mean distance/mm	Literature d-value/A	Calibrated camera length/cm
003	2.90	4.33	50
110	4.43	2.37	42
113	5.13	2.09	42

Table 4.5: Calibrated camera lengths

4.6 Particle downsizing and polymer adsorption

Particle downsizing may serve several purposes like for example increase in surface area and manufacturing of a solid material with a desired grain size. Downsizing of particles can be achieved by crushing and milling. The choice of method is dependent on both the substance and the desired particle size. In order to obtain very small particles a combination of methods may be used. In a ballmill a cylinder is filled with balls and a solid material or a dispersion. The material is grinded by friction and impact with the tumbling balls. Wet milling often gives smaller particle sizes than dry milling. This is because the interfacial tension is lower than surface tension, so that lower energy is needed. Once the particles have been downsized they may start to flocculate. A deflocculant, also called a dispersant, may be added to prevent flocculation. The dispersant may enhance particle stability either by charge or steric effects as explained in section 3.2.1.

Particle size can be measured by various techniques. Two of them are laser diffraction and dynamic light scattering explained in section 4.1. Different particle sizing techniques may use different physical properties to measure a particle and relate that value to a sphere in order to report a particle size. When comparing the results it is important to be aware of that, since most particles are irregularly shaped, the average values calculated by different physical properties will not be the same.

4.6.1 Downsizing of α-Al_2O_3 particles

The particle size of the α-Al_2O_3 powder was measured both by laser diffraction and by dynamic light scattering. The instrument used for the laser diffraction was a Cilas 1180 particle size analyser which can analyse particles in wet or dry dispersions. The software calculates both cumulative and distributive particle distributions and reports the 10, 50 and 90 percentiles. Either the Fraunhofer approximation or Mie theory can be selected for the particle size analysis. In order to use Mie theory, refractive index and absorption coefficient of the material need to be known. For the Mie theory the

refractive index of α-Al_2O_3 particles was set to 1.76 and the absorption coefficient to 0.01. The refractive index of water was set to 1.33.

The dynamic light scattering measurements were performed with a Malvern Zetasizer Nano ZS. The instrument analyses particles in wet dispersions with a wide range of concentrations. The software calculates the distributive particle distribution and the Z-average. The Z-average is an intensity based mean value.

Chemicals used for the downsizing of $\alpha - Al_2O_3$ particles were: • Aluminium oxide, alpha (α-Al_2O_3), 99.9%, Alfa Aesar • Polyphosphate dispersant Fluka (($NaPO_3)_n$), 15wt% solution • 0.5M HNO_3 standard solution

Laser diffraction is a more accurate measurement method than dynamic light scattering when the particle size is in the μm range. The particle size was therefore initially analysed by laser diffraction. The particles in the original powder were found to be in the μm-range rather than the desired nm-range, so downsizing was necessary. First the particles were wet milled in a ball mill (Gladstone Engineering Double Jar mill) for 48h. Al_2O_3 beads were used. The particle size was measured after 24h and 48h of milling.

The particle size was still not in the desired nanometer range after ball milling of the α-Al_2O_3 powder. A planetary mill rotates faster than a ball mill, so that the impact force on the particles is larger. The milling continued in a planetary mill (Retch mill PM400/2). 3mm ZrO_2 beads were used and the mill was set at 200rpm. There was room for two containers in the mill. One container was filled with the ball milled Al_2O_3-slurry while the other was filled with the ball milled slurry added the dispersing agent Fluka. The slurries were milled for 2h. The particle size was measured by dynamic light scattering after 1h and 2h of milling. These measurements suggested that the particles were agglomerating.

In theory, Al_2O_3 particles can also be stabilized by lowering the pH instead of adding a dispersing agent, see section 3.2.1. 0.5M HNO_3 was added to 20g of the ball milled Al_2O_3 slurry until the pH reached 2.28. Both slurries were milled in the planetary mill for 6h. The particle size was measured by dynamic light scattering after 1h, 2h and 6h. The measurements showed that the particle stability was improved by lowering the pH of the slurry.
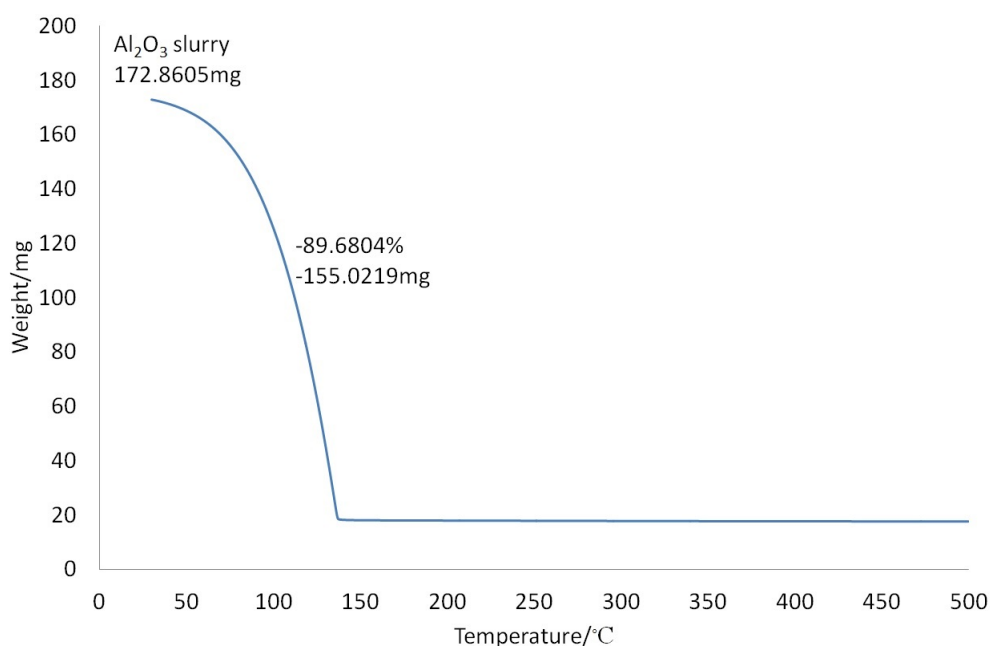
Figure 4.10: TGA graph of a Al_2O_3 slurry that was milled in a ball mill for 48h, milled in a planetary mill for 6h and where the pH was adjusted to 2.28.

To check the reproducibility of the results the pH was lowered to 2.22 by adding $0.5MHNO_3$ to 30g of the ball milled slurry, and milled in the planetary mill for 8h.

A small sample of the slurries was dried at 140°C for 48h. This included 3 slurries that were:

1. Ball milled for 48h.

2. Ball milled for 48h and milled in a planetary mill for 6h.

3. Ball milled for 48h, milled in a planetary mill for 6h and pH adjusted to 2.28.

The optimum drying temperature was found by a TGA measurement of the pH adjusted slurry (number 3 above). TGA method 2 was used, see appendix A. Figure 4.10 shows the TGA-graph with a sharp drop at approximately 140°C. The surface area of the powders obtained from the slurries as well as the original Al_2O_3-powder was measured and analysed with the BET-theory.

Concentration (mg/g)	PAA (g)
1	0.2215
2	0.4023
3	0.5990
5	1.0175
10	2.0045
20	4.0110
30	6.0035

Table 4.6: The amount of PAA added for each polymer concentration.

4.6.2 Polymer adsorption

The surface of oxide particles can be manipulated by adsorbing charged polymers. Two common charged polymers are poly(acrylic acid), PAA, and poly(ethylene imine), PEI. PAA is acidic and has a negative charge in aqueous dispersions, while PEI is basic and has a positive charge in aqueous dispersions. Polymer adsorption can be measured indirectly by measuring the amount of polymer in the slurry that is not adsorbed. The amount of adsorbed polymer can then be calculated if the initial amount of polymer is known.

Chemicals used were: • Aluminium oxide, alpha ($\alpha - Al_2O_3$), 99.9%, Alfa Aesar • Polyacrylic acid, PAA, partial sodium salt, 50wt% solution in water, M_w=5000 (GPC), Aldrich

First of all, the 50wt% PAA solution was diluted to a 2.5wt% solution. This was done by weighing 5g of 50wt% PAA-solution into a 100ml volumetric flask and filling up with water to the 100ml mark. The concentrations of the polymer were ranging from 1-30 mg/g (PAA/Al_2O_3). For each polymer concentration 5g of the Al_2O_3 powder was weighted into a small beaker. The wanted amount of PAA was added. Water was added so that the total weight of powder, polymer and water was 50g. The top of the beaker was covered with parafilm and the solution was left to stir for 16h and then left to sediment for 1h. The solution was centrifuged at 3000rpm for 5min and filtrated through a 0.025μm filterpaper (Millipore type VS). Table 4.6 shows the specific amount of 2.5wt%PAA added for each concentration.

Initially, concentrations ranging from 1-5mg/g as well as the 2.5wt% PAA solution were analysed by TGA. 2.5wt% PAA solution was also filtrated and analysed by TGA to check if the polymer was retained on the filter paper. Methods 3 and 4 were used,

see appendix A. The results showed that TGA probably was not a suitable method. The solutions were therefore also analysed by measuring the refractive index. The uncertainty in the measurement is ± 0.0001. Before the actual samples could be analysed a calibration curve for the PAA/PEI systems was made by measuring the refractive index of 0.5wt%, 1.0wt%, 1.5wt% and 2.0wt% standard PAA/PEI solutions. These were made in a similar way as the 2.5wt% solution described above. Finally, the refractive index was measured for all the polymer concentrations listed in table 4.6.

Chapter 5

Results

5.1 Catalyst synthesis and characterisation

5.1.1 $Co_{3-x}Mn_xO_4$ catalyst

$Mn(NO_3)_2 \cdot 6H_2O$ and $Co(NO_3)_2 \cdot 6H_2O$ were used during preparation of a metal solution that was later to be used in a coprecipitation. The concentrations of Mn and Co deviated from the expected concentrations. As both nitrates are hygroscopic they were analysed by TGA to check if the water amount was the same as stated by the manufacturer.

Figure 5.1 a) shows the TGA graph of $Mn(NO_3)_2 \cdot xH_2O$. The starting mass of $Mn(NO_3)_2 \cdot xH_2O$ is 272.2083mg. The final mass of the most stable compound, Mn_3O_4, is calculated to 72.2016mg. A simplified chemical reaction can be expressed as:

$$Mn(NO_3)_2 \cdot xH_2O \xrightarrow{heat} Mn_3O_4 \qquad (5.1)$$
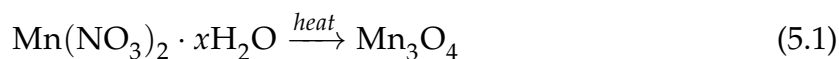
The equation above shows that the molratio is 1:1. Given this data the number of H_2O pr. $Mn(NO_3)_2$ was calculated to 6.028.

The number of H_2O pr. $Co(NO_3)_2$ was found in the same way. The most stable cobalt compound is CoO. The simplified chemical reaction is:

$$Co(NO_3)_2 \cdot xH_2O \xrightarrow{heat} CoO \qquad (5.2)$$

The molratio is also in this case 1:1. Figure 5.1 b) shows that the starting mass of $Co(NO_3)_2 \cdot xH_2O$ was 89.1946mg and the final mass of CoO is calculated to 23.5461mg. The calculated number of H_2O pr. $Co(NO_3)_2$ was found to be 5.6.

Metal:base ratio which would give a maximum amount of precipitate was investigated by coprecipitation of different metal:base ratios. The amount of precipitation was checked indirectly by measuring the concentrations of Mn and Co that had not precipitated. This is shown in table 5.1. Explanation on which ratios solutions 1-7 refer to can be found in table 4.1 on page 47. Figure 5.2 shows a plot of Mn and Co

(a)

(b)

Figure 5.1: TGA graphs showing weight loss as a function of temperature for **(a)**$Mn(NO_3)_2 \cdot xH_2O$ and $Co(NO_3)_2 \cdot xH_2O$. The most stable compound is also indicated on each graph.

Element	1	2	3	4	5	6	7
Mn	0.2019	0.1134	0.0398	0.0043	0.0042	0.0041	0.0041
Co	0.2275	0.1502	0.0668	0.0034	0.0026	0.0028	0.0029
Ce	0.0029	0.0025	0.0018	0.0012	0.0012	0.0012	0.0013

Table 5.1: Concentrations of Mn and Co in the precipitation liquid measured by XRF. Small amounts of Ce were also found, probably due to contamination.
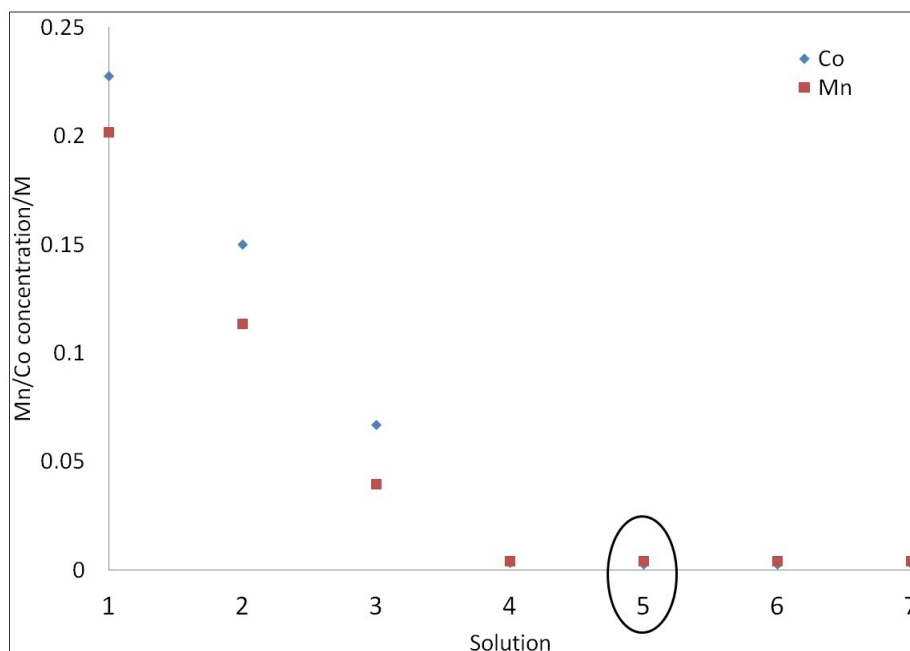
Figure 5.2: Plot of Mn- and Co-concentrations measured in the precipitate liquid as a function of precipitate solution number. The metal:base ratios used in solution 5 was chosen as the basis for a larger scale precipitation.

concentrations given in table 4.1 as a function of the precipitate solution number. All solutions in the range 4-7 give maximum coprecipitate yield. However, if solution 4 is chosen, small inaccuracies during preparation can lead to a precipitation that does not give the maximum yield. For that reason, solution 5 was used for the coprecipiatation of the catalyst $Co_{3-x}Mn_xO_4$.

The catalyst powder was calcined after coprecipitation and analysed by XRD, see section 4.2 for details. Figure 5.3 shows the acquired diffractogram for the powder calcined at 900°C (black) and 1100°C (red). The powder contains two phases at both calcination temperatures, $CoMn_2O_4$ (light blue) with a body-centered tetragonal crystal lattice, space groupe I41/amd, cell parameters a = 5.784A and c = 9.091A and $MnCo_2O_4$ (green) with a cubic crystal lattice, Fd$\bar{3}$m space group and cell parameter a =
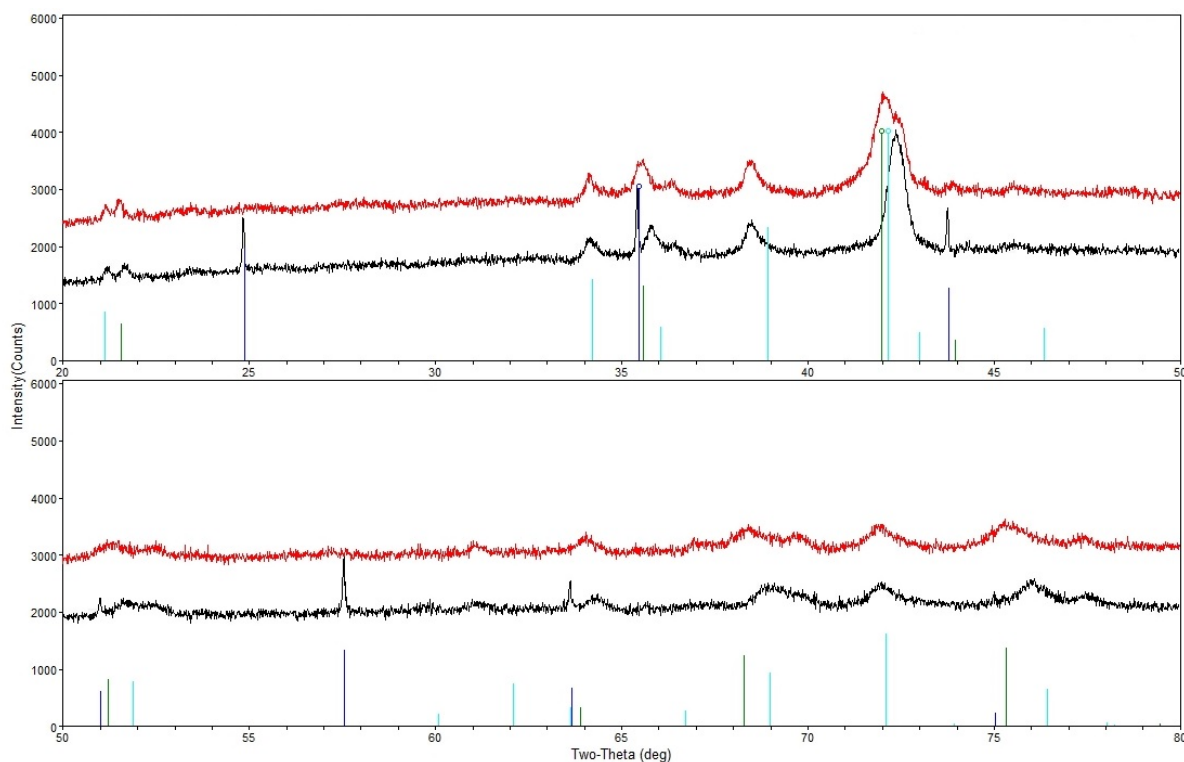
Figure 5.3: Diffractogram of the $Co_{3-x}Mn_xO_4$ catalyst powder calcined at 900°C (black) and 1100°C (red). Peaks from the LaB_6-referance are marked purple. $CoMn_2O_4$ phase is marked by light blue peaks while $MnCo_2O_4$ phase is marked by green peaks.

8.28A, are marked on the diffractogram [66, 67]. The composition of the two indicated phases is not accurate to the ones present in the catalyst powder. The peaks related to $MnCo_2O_4$ are shifted to the right towards smaller d-values. The remaining peaks were hard to identify. $CoMn_2O_4$ was found to be the best fit even though it does not provide a plausible explanation of all the peaks. For example, the peak at $2\theta \approx 38.2°$ is shifted to left, while the peak at $\approx 42.5°$ is shifted to the right. However, the rest of the remaining peaks are well explained by this phase if a shift towards smaller d-values is taken into consideration.

The targeted catalyst was $Co_{3-x}Mn_xO_4$ with a spinel structure. Figure 5.3 clearly shows that this is not accomplished. This catalyst was anyhow used for further experiments as the composition of the phase is not crucial. The focus of this work is primarily on the reaction that occurs when a supported catalyst undergoes high temperature treatment. The powder is assigned as Co-Mn-O which is meant to indicate that more than one phase is present.

5.1.2 LaMnO$_3$ **catalyst**

The LaMnO$_3$ catalyst was to be synthesised by the sol-gel method. One of the components used during the synthesis is La(NO$_3$)$_3 \cdot$ 6H$_2$O. A TGA was first performed to check if the water amount was the same as stated by the manufacturer. Figure 5.4 (a) shows the TGA graph of La(NO$_3$)$_3 \cdot x$H$_2$O.

The most stable lanthanum compound is La$_2$O$_3$. The simplified chemical reaction is:

$$2\text{La(NO}_3)_3 \cdot z\text{H}_2\text{O} \xrightarrow{heat} \text{La}_2\text{O}_3 \tag{5.3}$$
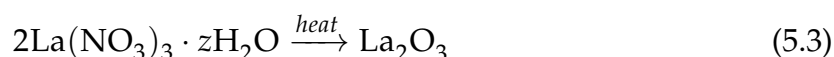
The molratio is in this case 2:1. Figure 5.1 c) shows that the starting mass of La(NO$_3$)$_3 \cdot x$H$_2$O was 105.9938mg. The final mass of La$_2$O$_3$ was calculated to 39.6145mg. The calculated amount of H$_2$O pr. La(NO$_3$)$_3$ was found to be 6. This is the same as the number given by the manufacturer.

During synthesis a TGA was performed both to check the temperature at which the gel decomposes, and to check that all the gel had decomposed. Figure 5.4 (b) shows a sharp weight drop at a temperature $\approx$210°C, which indicates that this is the decomposition temperature. On the other hand, there is no weight drop in figure 5.4 (c), which shows that all the gel had in fact decomposed.

The produced powder was analysed by XRD with Cr-Kα_1 radiation. Figure 5.5 shows the acquired diffractogram. Narrow peaks with relatively high intensity indicate that the produced powder is crystalline. The position of the peaks is consistent to the La$_{0.969}$Mn$_{0.93}$O$_3$ phase with a rombohedral crystal lattice, space group R$\bar{3}$c with cell parameters a = 5.5220A, c = 13.33170A [68]. It should be noted that the (110) intensity is the strongest one for the La$_{0.969}$Mn$_{0.93}$O$_3$ phase. In the diffractogram, reflection from (104) gives the strongest intensity. The difference in the two intensities for the La$_{0.969}$Mn$_{0.93}$O$_3$ phase are not large, 999 vs. 993. The diffractogram shows no other peaks than those of the Si-reference.
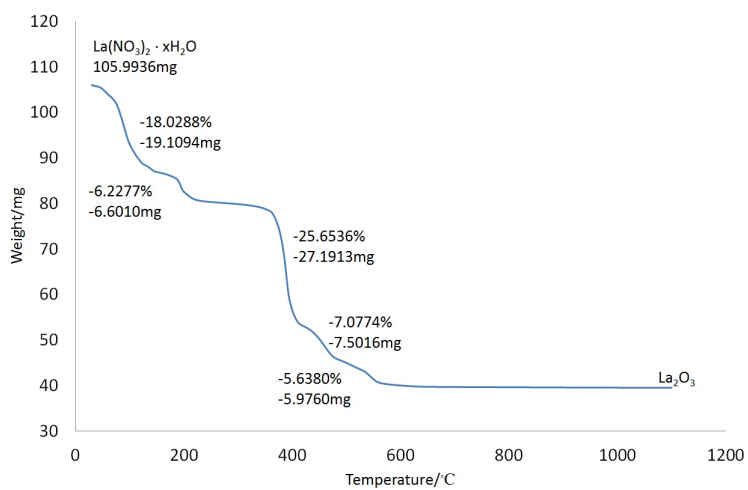
(a)
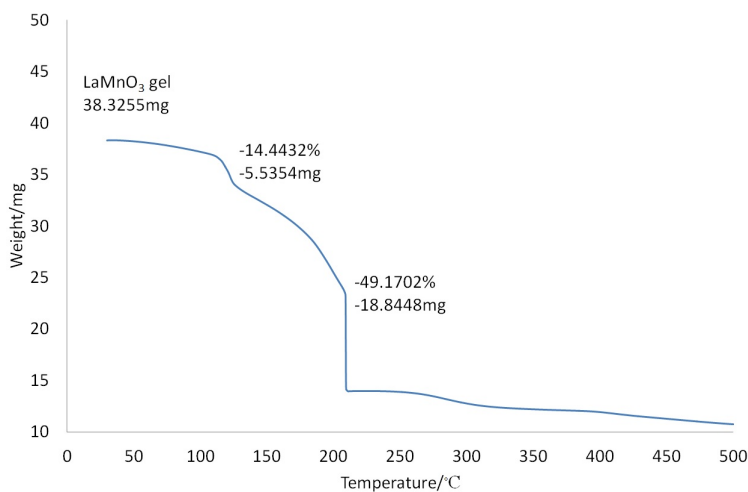
(b)
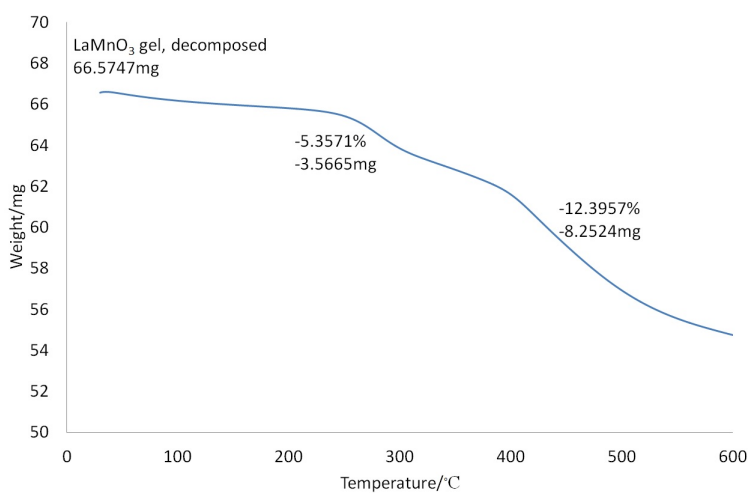
(c)

Figure 5.4: TGA graphs showing weight loss as a function of temperature of **(a)**$La(NO_3)_3 \cdot xH_2O$, **(b)** the $LaMnO_3$ gel indicating a transition temperature at $\approx 210°C$ and **(c)** the $LaMnO_3$ gel after the decomposition of the organic network.
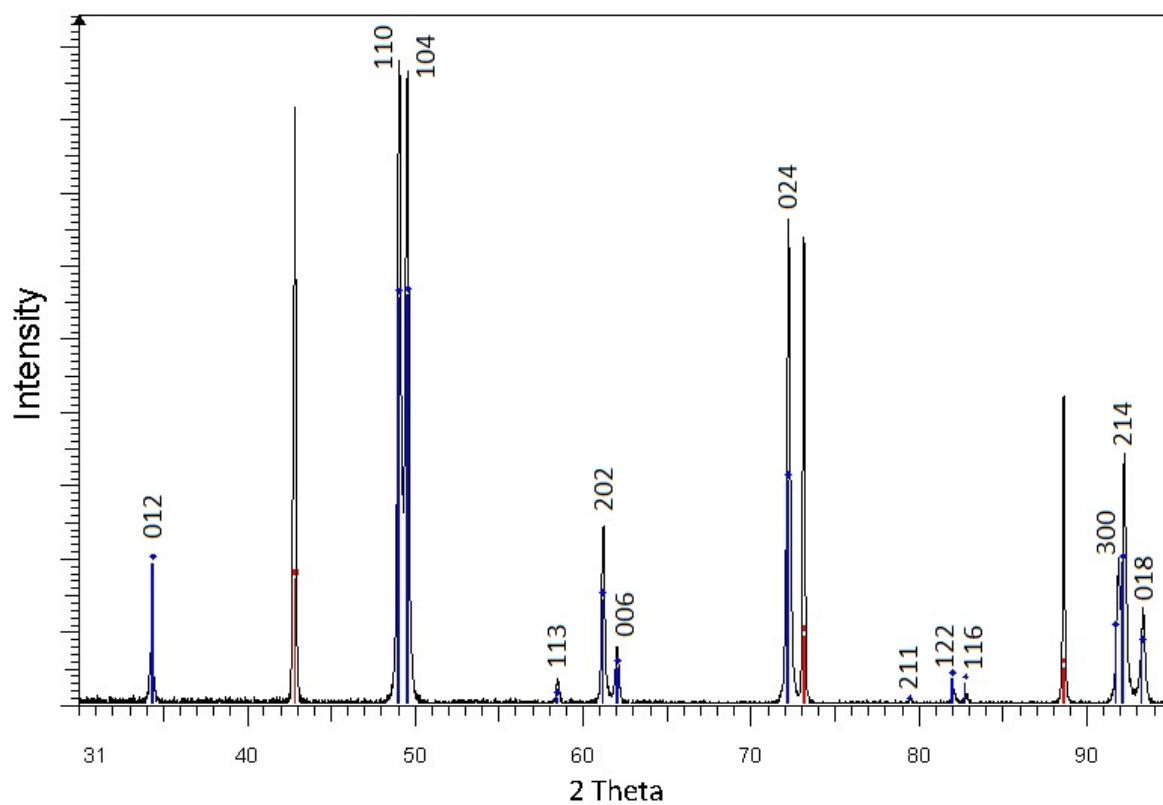
Figure 5.5: Diffractogram of the $La_{0.969}Mn_{0.93}O_3$ catalyst powder. Peaks from the Si-referance are marked red, while peaks from the catalyst powder are marked blue.

Figure 5.6: The figure shows the 10nm Pt-layer deposited on single crystals of α-Al$_2$O$_3$ and sintered for 4h at **(a)** 430°C, **(b)** 550°C, **(c)** 650°C and **(d)** 770°C.

5.2 Characterization of the Pt-reference layer

A layer of Pt-particles was desired as a reference between the catalyst and the support. The deposition method and selection of sintering temperatures is described in section 4.3.

Figure 5.6 shows the surface of the 10nm Pt-layer deposited on α-Al$_2$O$_3$ single crystals and sintered for 4h at (a) 430°C, (b) 550°C, (c) 650°C and (d) 770°C. Figure 5.7 shows the surface of the 10nm Pt-layer deposited on YSZ single crystals and sintered for 4h at (a) 430°C, (b) 550°C, (c) 650°C and (d) 770°C.

(a)

(b)

(c)

(d)

Figure 5.7: The figure shows the 10nm Pt-layer deposited on single crystals of YSZ and sintered for 4h at **(a)** 430°C, **(b)** 550°C, **(c)** 650°C and **(d)** 770°C.

Figure 5.6 and figure 5.7 show that the desired small Pt-particles are formed at 770°C. By comparing figure 5.6 (a) and (b) to figure 5.7 (a) and (b) it also shown that the support has an effect on the formation of Pt-particles at temperatures below 650°C.

Once the correct sintering temperature was established, the effect of the initial Pt-layer thickness was investigated. Figure 5.8 shows the surface of the formed Pt-particles for the initial Pt-layer thicknesses of 2.5nm and 5nm deposited on the single crystals of (a)/(b) α-Al_2O_3 and (c)/(d) YSZ. Small Pt-particles are formed on both surfaces with both Pt-layer thicknesses. As expected, the surface that was covered with a 5nm Pt-layer has a higher Pt-particle coverage than the surface that was covered with a 2.5nm Pt-layer.

These experiments showed that the desired Pt-particles were formed when a 5nm Pt-layer was deposited on $\alpha - Al_2O_3$ and YSZ single crystals and sintered at 770° for 4h.

(a)

(b)

(c)

(d)

Figure 5.8: Initial Pt-layer thickness of 2.5nm and 5nm deposited on **(a)/(b)** α-Al$_2$O$_3$ and **(c)/(d)** YSZ, respectively.

Figure 5.9: Image of the $La_{0.969}Mn_{0.93}O_3/Al_2O_3$ sample. EDS measurements were performed in point 1 and 2 as indicated in the image.

	Point 1		Point 2	
Element	**Wt%**	**At%**	**Wt%**	**At%**
Aluminium	70.98	89.91	66.51	87.89
Lanthanum	21.16	5.21	24.52	6.29
Manganese	7.86	4.89	8.97	5.82

Table 5.2: Atom% and weight% obtained by EDS of the $La_{0.969}Mn_{0.93}O_3/\alpha$-$Al_2O_3$ interface layer at point 1 and 2

5.3 Characterization of a supported catalyst with a Pt-reference

The catalyst inks were painted onto the single crystals of α-Al_2O_3 and YSZ as described in section 4.4.

5.3.1 $La_{0.969}Mn_{0.93}O_3/\alpha$-$Al_2O_3$ interface

A TEM sample was prepared after annealing as described in section 4.5.1. Figure 5.9 shows an overview image of the $La_{0.969}Mn_{0.93}O_3/\alpha$-$Al_2O_3$ sample. The catalyst interface layer was initially analysed by SEM. Unfortunately, the Pt-reference layer was not visible on SEM images analysed by backscattered electrons. In order to investigate the extent of the catalyst-support interaction, element analysis was performed with EDS at two boundary positions; point 1 close to the pure α-Al_2O_3 single crystal and point

74

2 close to the catalyst surface, see figure 5.9. Table 5.2 shows a summarized overview of the measured elements and their atom% and weight% at the two different points indicated in figure 5.9.

Figure 5.10 shows the diffractogram of the $La_{0.969}Mn_{0.93}O_3/\alpha$-$Al_2O_3$ sample in black. The sample was attached to the sample holder with Blu Tack. Some background from Blu Tack is observed. Blu Tack diffractogram is shown in red. It was not possible to run the measurement with a reference. The phase $LaMnAl_{11}O_{19}$ with a hexagonal crystal lattice, space group P63/mmc and cell parameters a = 5.574A and c = 22.008A, was found to be the best fit to the data. This phase is indicated in the diffractogram in figure 5.10 [69]. The peaks from the interface layer are shifted to the left in the direction of larger d-values. This may because the measurement was run without a reference, so the diffractogram is not adjusted. It can also be because the composition is not correct, or the sample was not aligned properly in the sample holder. The $LaMnAl_{11}O_{19}$ phase does not account for all the peaks observed in the diffractogram. These were in general difficult to analyse as a reference is not used. Two other phases are indicated, $La(AlO_3)$ (light blue) with a rhombohedral crystal lattice, space group R3m and cell parameter a = 3.789A, as well as $La_{0.951}Mn_{0.951}O_3$ (green) with a rhombohedral crystal lattice, space group R$\bar{3}$c [70, 71]. These measurements were obtained and analysed at the Yara Technology Centre. They have access to a different crystallographic database than the University of Oslo. The $La_{0.951}Mn_{0.951}O_3$ phase was the one that was closest to the composition of the catalyst $La_{0.969}Mn_{0.93}O_3$. This phase is indicated to check if some of the peaks can be explained by the presence of the catalyst that has not reacted with the support. None of the phases listed up in the diffractogram are a perfect fit. This is commented in section 6.3.1.

The interface layer was also studied by TEM to complement the XRD results. The camera length of the microscope was calibrated as explained in section 4.5.2. Figure 5.11 shows the obtained indexed diffraction pattern. The d-values were calculated by equation (4.3) for camera lengths of 42cm and 50cm and are shown in table 5.3.

hkl	Mean distance/mm	d-value/A (L=42cm)	d-value/A (L=50cm)
002	1.01	10.4	12.42
110	3.94	2.66	3.18
112	4.06	2.59	3.09

Table 5.3: D-values calculated with a camera length, L, of 42cm and 50cm as well as mean measured distances in the diffraction pattern and according diffraction planes.

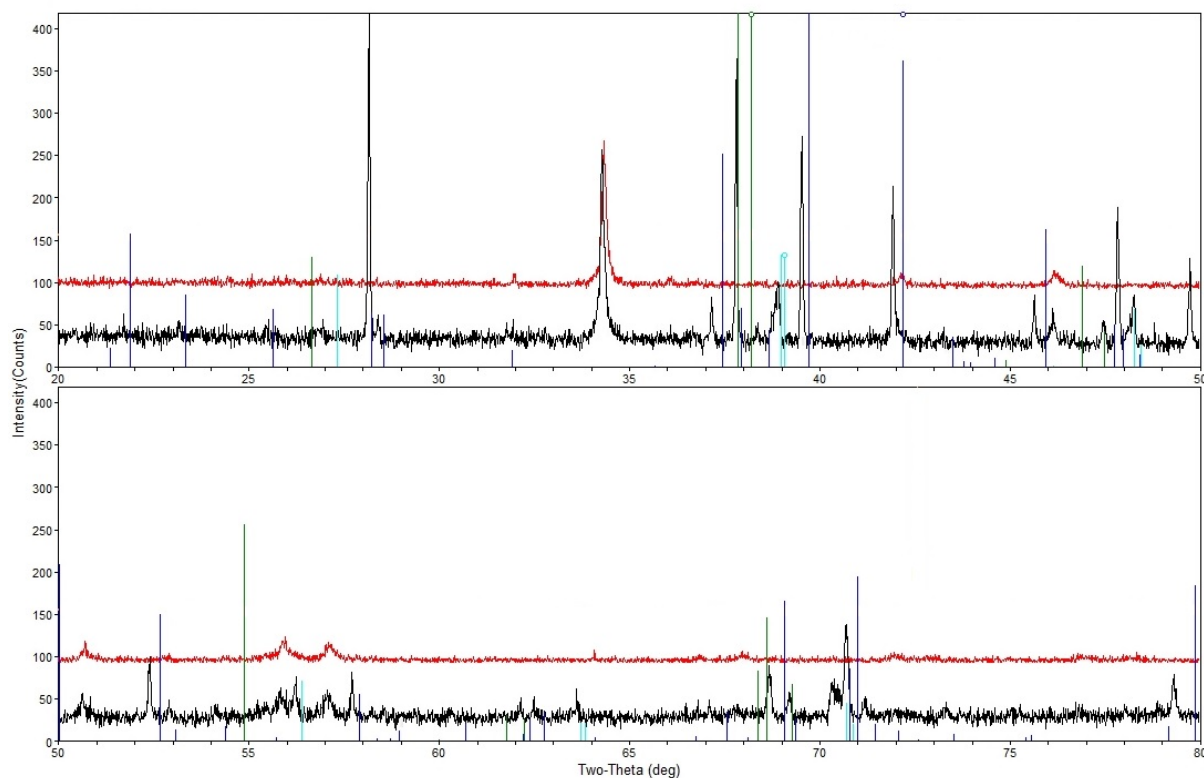**Figure 5.10:** Diffractogram of the $La_{0.969}Mn_{0.93}O_3/\alpha$-$Al_2O_3$ sample (black) and Blu Tack (red). Expected peak positions for $LaMnAl_{11}O_{19}$ is marked purple, $La(AlO_3)$ is marked light blue and $La_{0.951}Mn_{0.951}O_3$ is marked green.
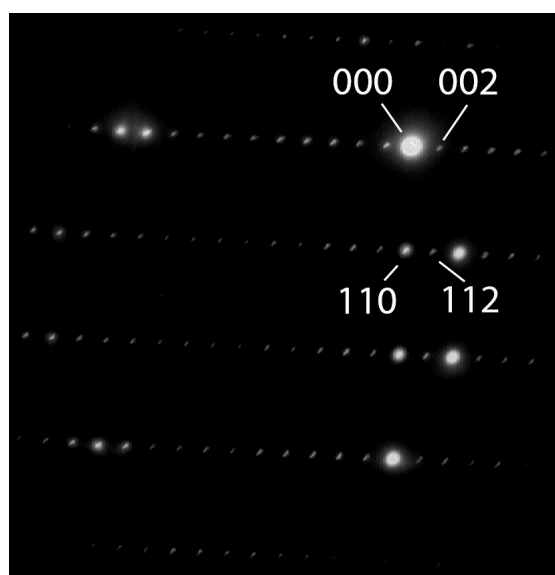
Figure 5.11: Diffraction pattern along the [1 $\bar{1}$ 0] zone axis of the $La_{0.969}Mn_{0.93}O_3/\alpha$-$Al_2O_3$ interface.
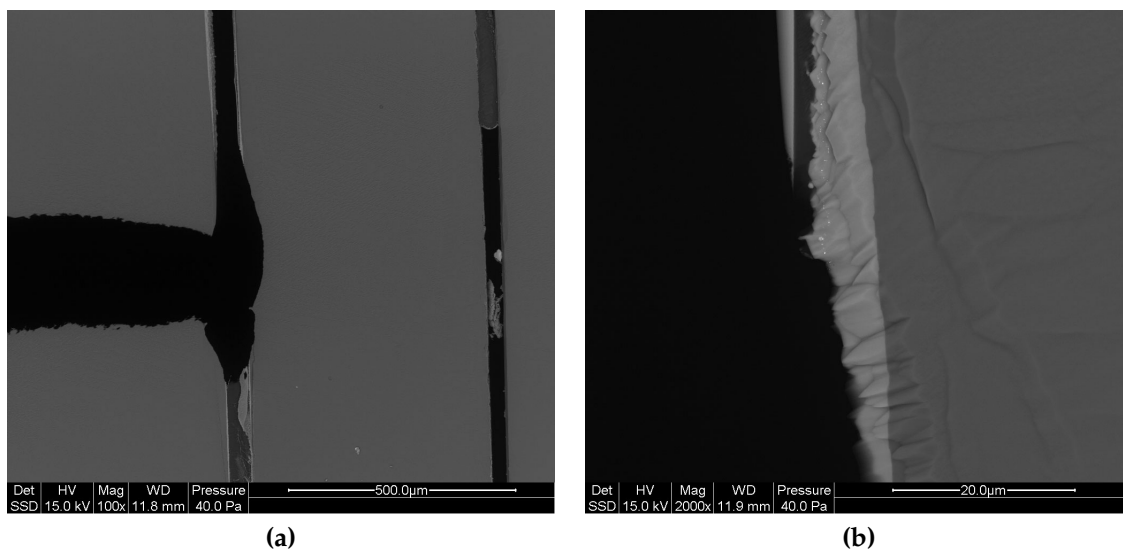
Figure 5.12: Image of the Co-Mn-O/α-Al$_2$O$_3$ sample showing **(a)** an overview and **(b)** the Pt-reference layer.

5.3.2 Co-Mn-O/α-Al$_2$O$_3$ interface

Also here, a TEM sample was prepared after annealing. Figure 5.12 shows (a) an overview image of the Co-Mn-O/α-Al$_2$O$_3$ sample and (b) an image showing the Pt-reference layer. An EDS of the layer between the Pt-reference and the α-Al$_2$O$_3$ support was performed. Table 5.4 shows atom% and weight% of aluminium, cobalt and manganese when the aluminium background is subtracted. An EDS of the layer between the catalyst and the Pt-reference was also performed and found to deviate by only a few atom% in relation to the values shown i table 5.4.

Figure 5.13 shows the diffractogram of the Co-Mn-O/α-Al$_2$O$_3$ sample. This measurement was also not run with a reference. In the same way as the La$_{0.969}$Mn$_{0.93}$O$_3$/α-Al$_2$O$_3$, this sample was also attached to the sample holder with Blu Tack. There is a peak assigned to Blue Tack at 2θ=46.5°. Otherwise, three other phases that could have formed and explain the peaks in the diffractogram by left of right displacement are marked. MnCo$_2$O$_4$ (purple) with a cubic crystal lattice, space group Fd$\bar{3}$m and cell parameter a = 8.28A, CoCo$_2$O$_4$ (light blue) with a cubic crystal lattice, space group Fd$\bar{3}$m and cell parameter a = 8.0837A, as well as (Mn$_{0.89}$Al$_{0.11}$)Al$_2$O$_4$ with a cubic crystal lattice, Fd$\bar{3}$m space group and cell parameter a = 8.181A. These phases are discussed in further detail in section 6.3.2.

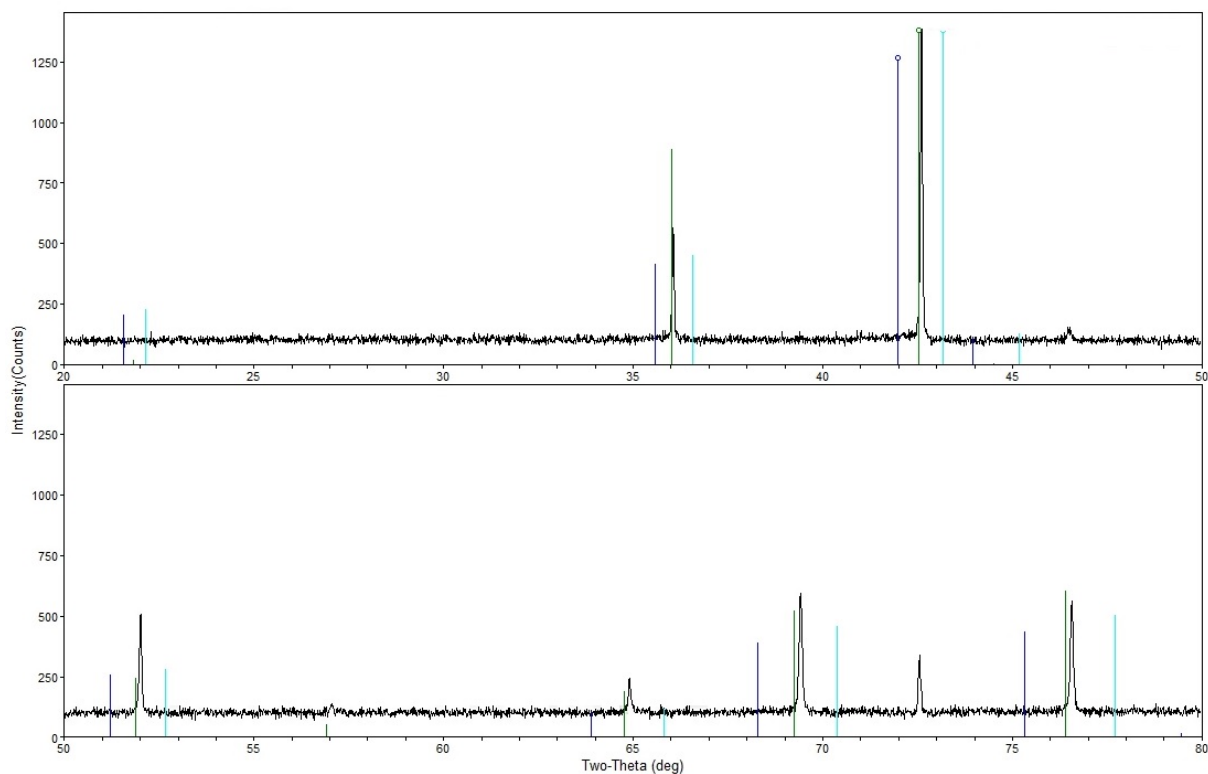The interface of the layer was also studied by TEM to complement the XRD results.

Figure 5.13: Diffractogram of the Co-Mn-O/Al_2O_3 sample. Expected peak positions for $MnCo_2O_4$ phase is marked purple, $CoCo_2O_4$ is marked light blue and $(Mn_{0.89}Al_{0.11})Al_2O_4$ is marked green.

Element	Wt%	At%
Aluminium	52.19	69.75
Cobalt	25.67	15.71
Manganese	22.15	14.54

Table 5.4: Atom% and weight% obtained by EDS of the Co-Mn-O/α-Al_2O_3 interface layer.

Direction	Mean distance/mm	d-value/A (L=58cm)	d-value/A (L=60cm)
1	4.17	3.48	3.60
2	5.63	2.58	2.66
3	6.73	2.16	2.23

Table 5.5: D-values calculated with a camera length, L, of 58cm and 60cm as well as mean measured distances in the diffraction pattern.
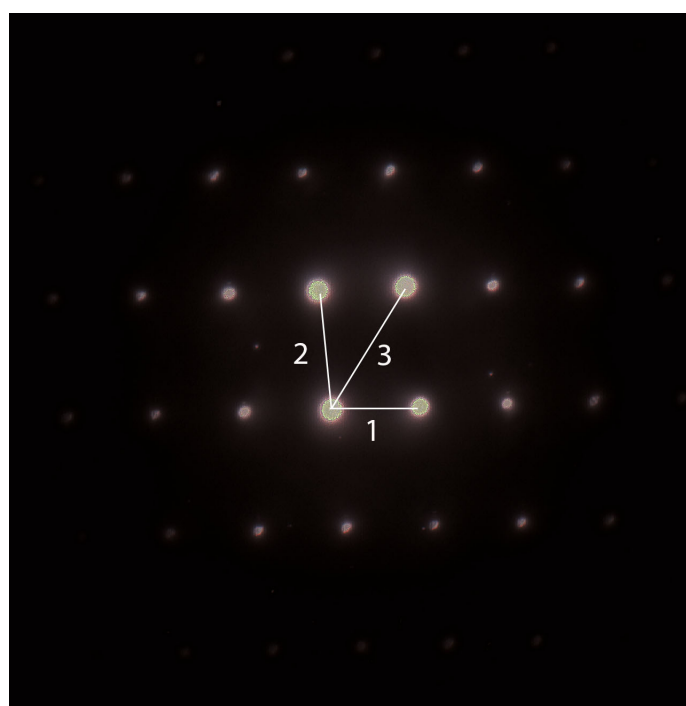
Figure 5.14: Diffraction pattern of the Co-Mn-O/α-Al$_2$O$_3$ interface.

Diffraction pattern images of the catalyst layer interface were obtained with a 66cm camera length at eucentric height. Stokkan reported in her master thesis that the camera length varied from 58.6cm to 60.4cm for the nominal length of 66cm [72]. In the following, the d-values of the catalyst layer interface are calculated with both camera lengths, 58cm and 60cm, by equation 4.3. The results are shown in table 5.5. Unfortunately, it was not possible to identify the phase which the diffraction pattern describes. An EDS of the phase was performed showing that the phase contained aluminium, manganese and cobalt.

5.4 Particle downsizing and polymer adsorption

## 5.4.1 Downsizing of $\alpha - Al_2O_3$-particles

The particle size was measured by two different techniques, laser diffraction and dynamic light scattering. In general, laser diffraction gives more accurate measurements when particles are in μm range, while dynamic light scattering gives more accurate measurements when the particles are in nm range.
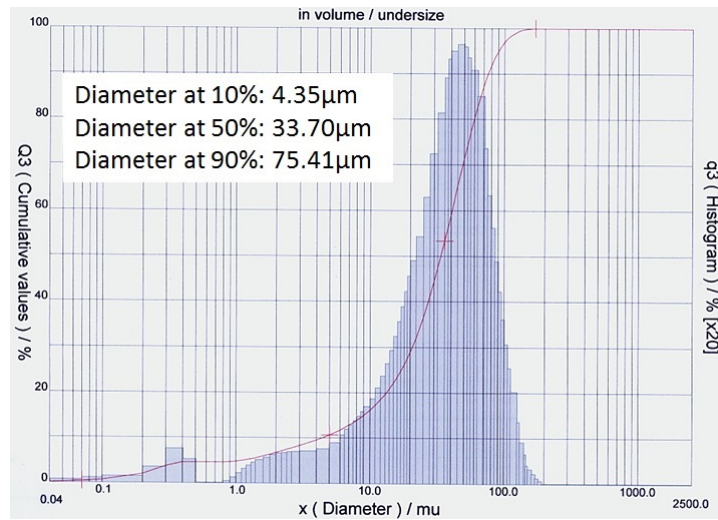
Particle size measurements by laser diffraction

The desired median diameter (d(50%) value) of the α-Al_2O_3 particles was in the nanometer range in order to prevent sedimentation during zeta potential measurements. First, the particle size of the original α-Al_2O_3 powder was measured by laser diffraction and the results were analysed by both Mie theory and Fraunhofer approximation. Figure 5.15 show that there is a good correlation between the d(50%) values as calculated by the (a) Fraunhofer approximation, d(50%) = 33.76μm and (b) Mie theory, d(50%) = 33.70μm. To check whether the particles were agglomerating a dispersant Fluka was added and another measurement performed and analysed with the Fraunhofer theory. This result is shown in figure 5.15 (c) where the d(50%) value is measured to 32.38μm. This shows that the α-Al_2O_3 do not agglomerate prior to milling.

The measured particle size as shown in figure 5.15 shows that the particles are too large compared to the desired nanometer range. Moreover, the size distribution is not unimodal. The powder was therefore wet milled in a ball mill. Figure 5.16 shows the measured particle size analysed after 24h of milling by (a) Fraunhofer approximation and (b) Mie theory. The d(50%) value as analysed by the Fraunhofer approximation has been lowered from 33.76μm to 0.83μm and from 33.70μm to 1.00μm as analysed by Mie theory. The same measurement was performed with Fluka added prior to the measurement. This is shown in figure 5.17. By comparing the values to those measured without Fluka, an indication of particle agglomeration after milling can be observed. The d(50%) value as measured with Fluka and analysed with the Fraunhofer approximation is 0.68μm opposed to 0.83μm without Fluka, and 0.91μm with Fluka and analysed with the Mie theory as opposed to 1.00 μm without Fluka. In both cases the d(50%) diameters are lower for the measurements where Fluka was added.
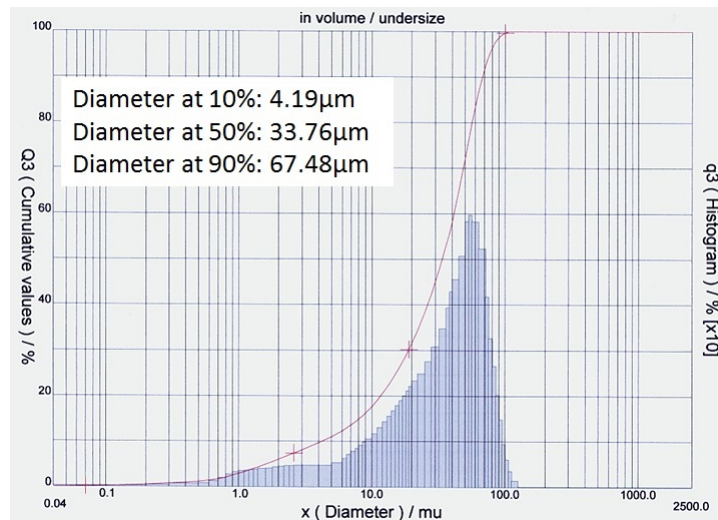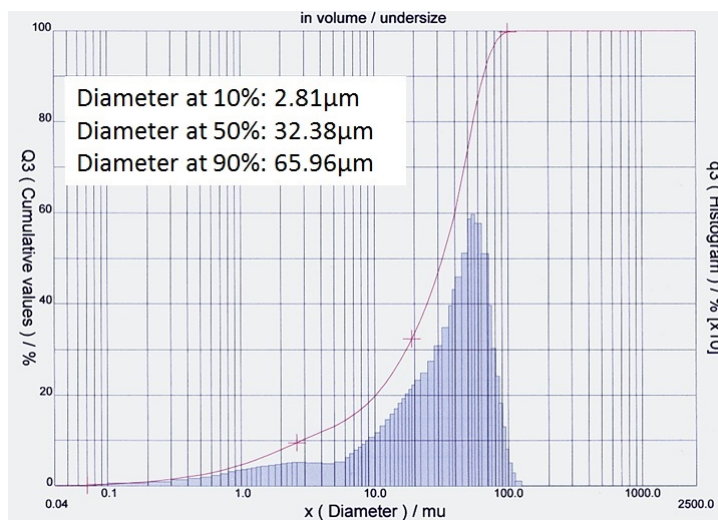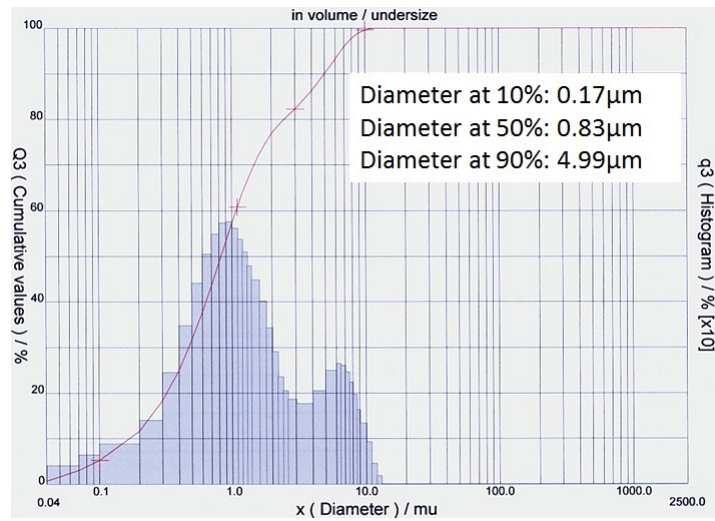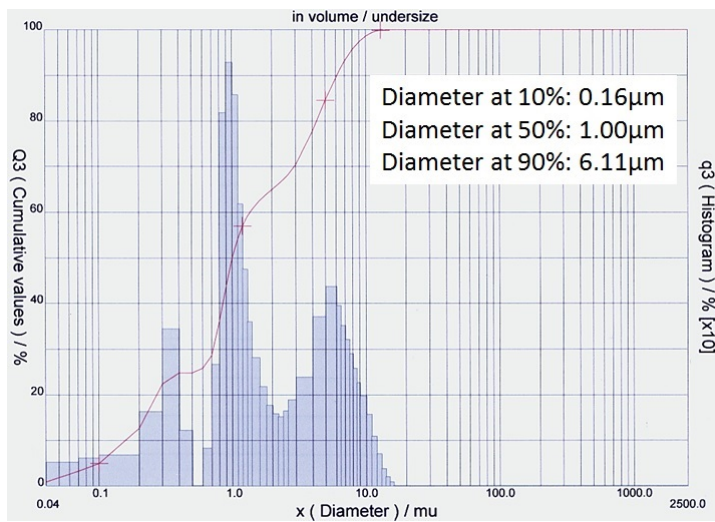
(a)

(b)

(c)

Figure 5.15: The particle size of the original α-Al$_2$O$_3$ powder measured by laser diffraction and **(a)** analysed with the Fraunhofer approximation, **(b)** analysed with the Mie theory, (c) added dispersant Fluka and analysed with the Fraunhofer approximation.
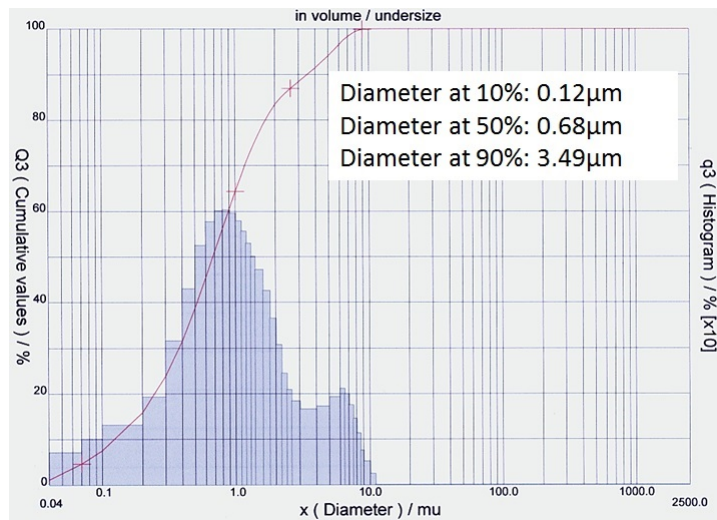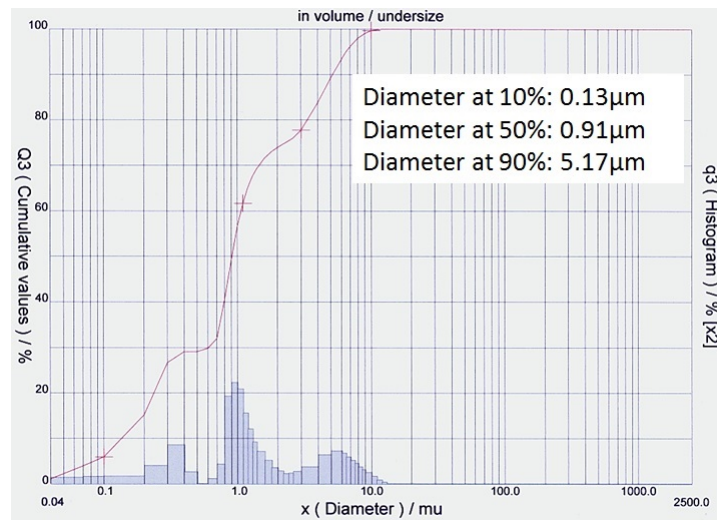
81

(a)

(b)

Figure 5.16: The particle size measured by laser diffraction after 24h of ballmilling and **(a)** analysed with the Fraunhofer approximation, **(b)** analysed with the Mie theory.

(a)

(b)

Figure 5.17: The particle size measured by laser diffraction after 24h of ballmilling and **(a)** added a dispersant Fluka and analysed with the Fraunhofer approximation, **(b)** added a dispersant Fluka and analysed with the Mie theory.
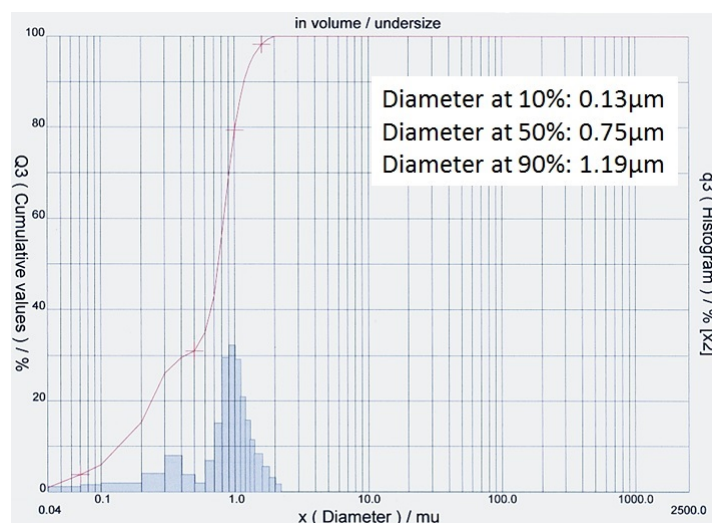
Figure 5.18: The particle size measured by laser diffraction after 48h of ballmilling and analysed with the Mie theory. A dispersant Fluka was added prior to the measurement.

A unimodal particle size distribution was still not achieved, so the milling continued for another 24h (48h in total). Another measurement was performed to check the effect of further ballmilling. This time the particle size was only measured with Fluka added and analysed with the Mie theory. This measurement is shown in figure 5.18. The d(50%) value is here measured to 0.75μm. The particle size distribution is still bimodal. The decrease in particle size by the additional 24h of ballmilling was not large (Δd(50%) = 0.16μm). Further milling was therefore continued in a planetary mill. A planetary mill rotates faster than a ball mill so that the impact force on the particles is larger. In this way, smaller particle sizes are achievable in shorter time. Also, subsequent particle size measurements were performed by dynamic light scattering rather than laser diffraction as smaller particle sizes can be measured by dynamic light scattering.

Particle size measurements by dynamic light scattering

First, the particle size of the sample that was ball milled for 48h was measured by dynamic light scattering. This is shown in figure 5.19 (a) where the Z-average is measured to 2949nm. The Z-average value obtained by dynamic light scattering is not directly comparable to the d(50%) value obtained by laser diffraction. Z-average is an intensity weighted mean value, while the d(50%) value is a volume weighted mean value. However, the results displayed in figure 5.19 (a) are a good reference for further milling.

The planetary mill is balanced by two containers. Both containers were filled with the Al_2O_3-slurry and ZrO_2 balls, but Fluka was added to only one container. Figure 5.19 (b) and (c) show the results after 2h of milling for the sample without Fluka, Z-average = 2941nm and with Fluka, Z-average 354.4nm, respectively. The large difference in measured particle size show that the particles are unstable and start agglomerating after milling.

Figure 5.19 (c) shows that the particle size is in the desired nanometer range when the particles are stabilized. Stabilization of particles by polymer adsorption is however not a good idea since charged polymers will be adsorbed later to manipulate the surface charge of the α-Al_2O_3 particles.

Oxide particles dispersed in water can also be stabilized by changing the pH as explained in section 3.2.1. Stabilization of particles by lowering the pH in the slurry was tested, see section 4.6.1 for experimental details. The pH lowered slurry and the "original" ball milled slurry were milled for 1h in a planetary mill. Figure 5.20 shows that the Z-average = 3388nm for the "original" slurry and that the Z-average = 398.4nm for the pH reduced slurry. This shows that the particles can be stabilized by lowering the pH of the slurry instead of polymer adsorption. The particle size distribution shown in figure 5.20 (b) is however still slightly bimodal. The two slurries were therefore milled for another hour, now total of 2h in the planetary mill.

Figure 5.21 (b) shows that the distribution is of a more pronounced bimodal shape than that in figure 5.20 (b). The particle size is lower, Z-average = 318.0nm for the pH reduced slurry and Z-average = 3338nm for the "original" slurry. The slurries were milled for another 4h. Figure 5.22 shows the effect of a total of 6h milling in a planetary mill for (a) the "original" slurry, Z-average = 2054nm and (b) the pH reduced slurry, Z-average = 257.7nm. Moreover, figure 5.22 (b) shows that the desired particle size with a unimodal distribution is finally obtained. The reproducibility of the results was checked by adjusting the pH of a new slurry to 2.22 and milling for 8h in a planetary mill. Figure 5.22 (c) shows that the results are easily reproducible, Z-average = 201.nm.
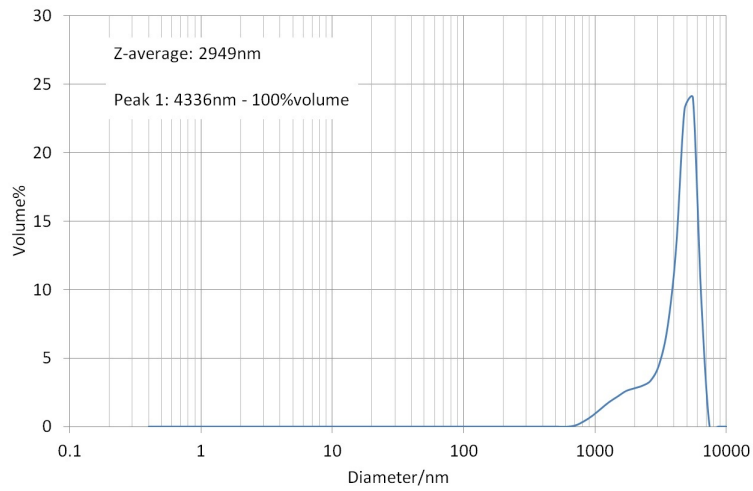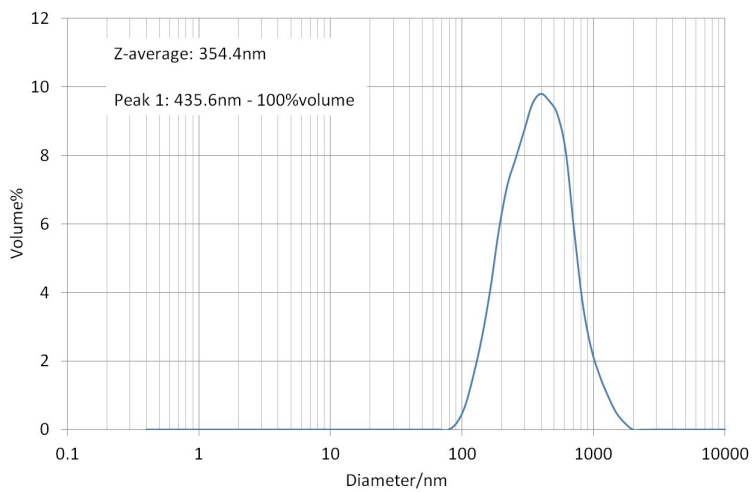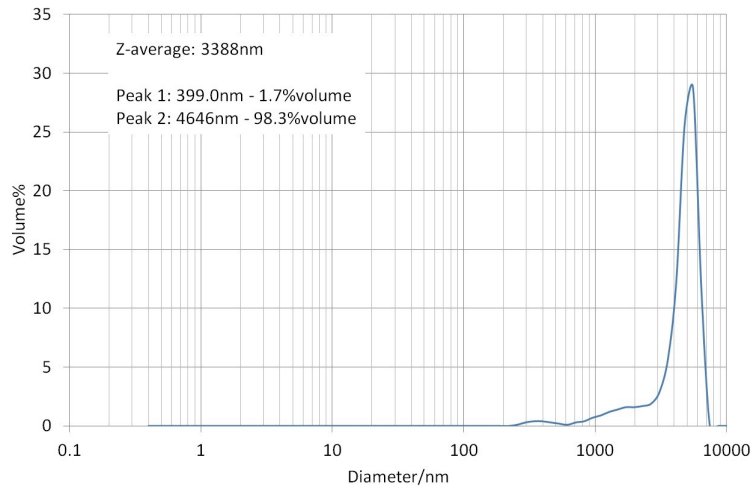
(a)
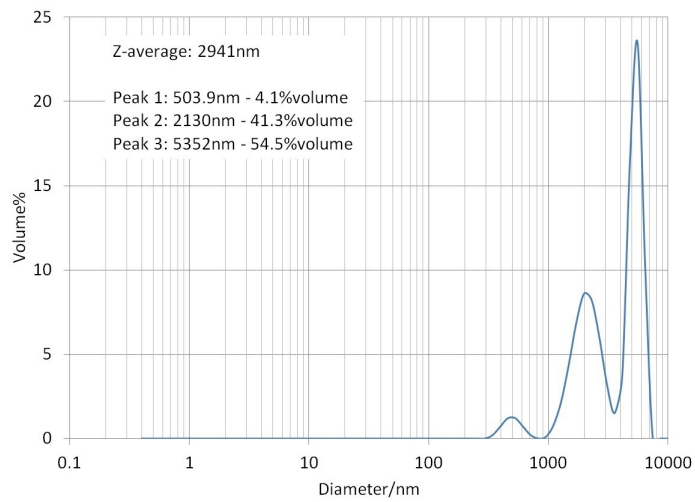
(b)

(c)

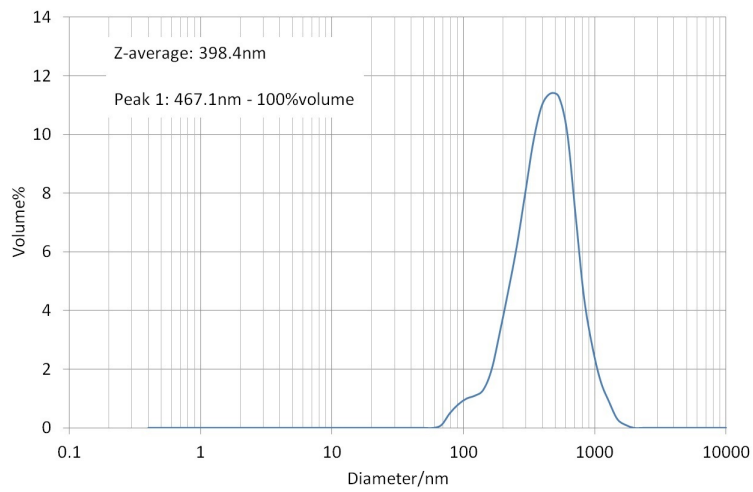**Figure 5.19:** Particle size of the Al_2O_3-slurry measured by dynamic light scattering after **(a)** 48h of ballmilling, **(b)** additional 2h planetary milling, **(c)** additional 2h planetary milling with added Fluka.

(a)

(b)

Figure 5.20: Particle size measured after 1h of planetary milling of **(a)** the ballmilled Al$_2$O$_3$-slurry and **(b)** the ballmilled Al$_2$O$_3$-slurry with pH = 2.28

(a)

(b)

Figure 5.21: Particle size measured after 2h of planetary milling of **(a)** the ballmilled Al_2O_3-slurry and **(b)** the ballmilled Al_2O_3-slurry with pH = 2.28
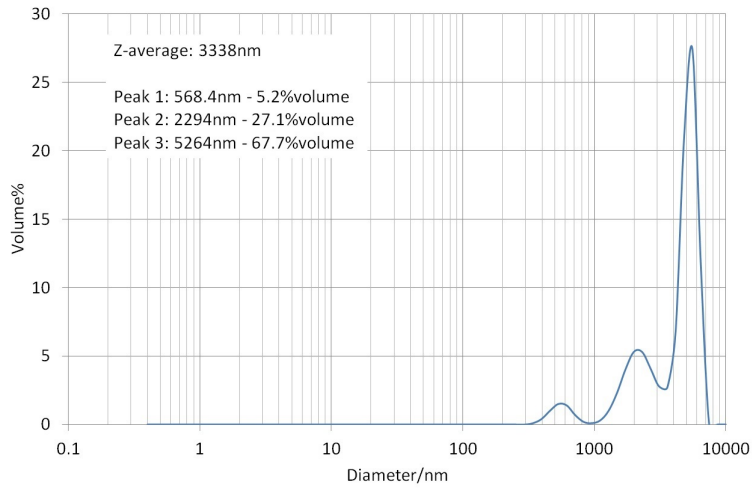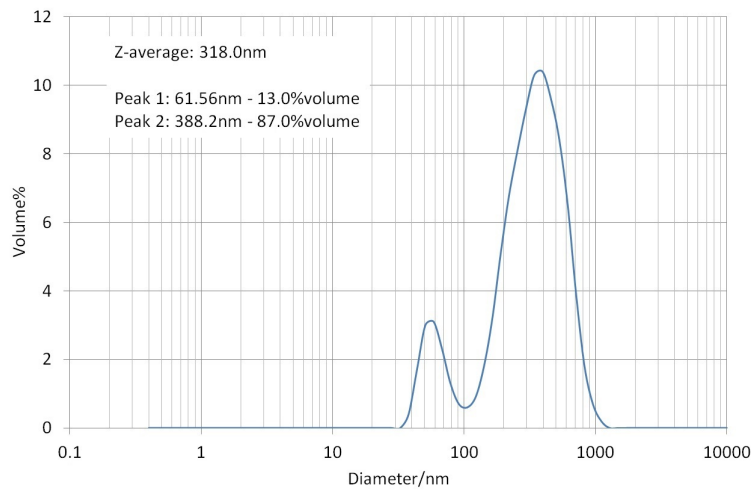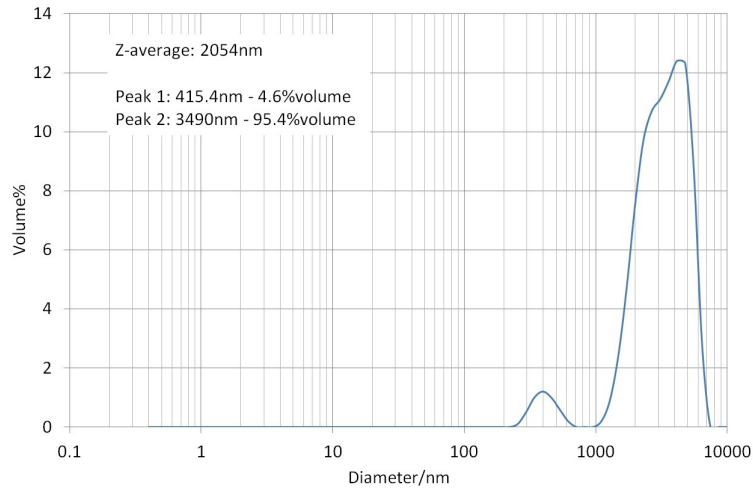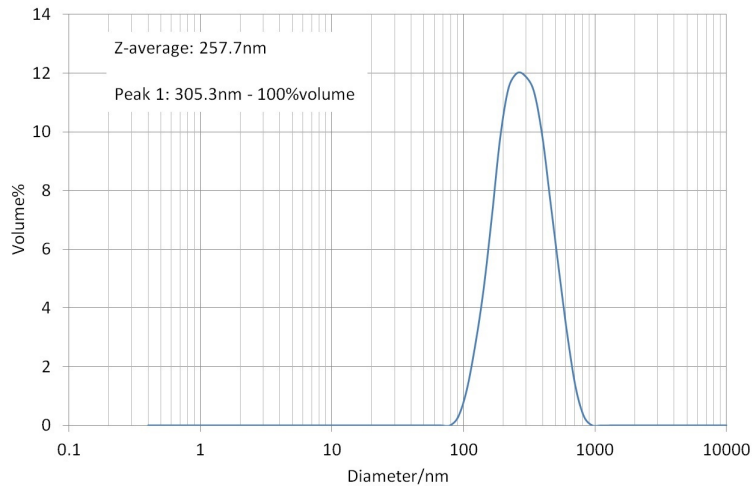
(a)

(b)

(c)

Figure 5.22: Particle size measured after 6h of planetary milling of **(a)** the ballmilled Al_2O_3-slurry and **(b)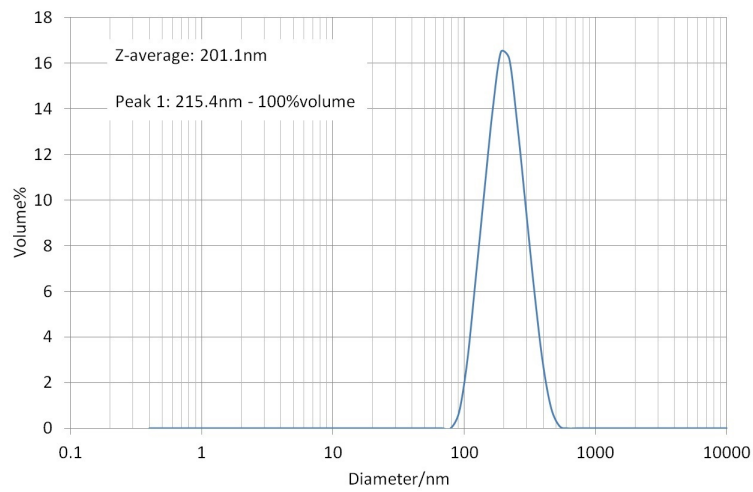** the ballmilled Al_2O_3-slurry with pH = 2.28. **(c)** Particle size measured after 8h of planetary milling where pH = 2.22.

Measured area ($\frac{m^2}{g}$)	Original powder	Ball mill	Planetary mill	pH
Micropore	0.6239	0.3041	2.1630	2.8466
External surface	4.5533	5.4811	16.6313	27.5091
Total BET surface	5.1772	5.7851	18.7943	30.3557

Table 5.6: Micropore area, external surface area and total BET surface area of the original Al_2O_3 powder as well as 3 milled powders. The powder indicated as "ball mill" was ball milled for 48h, the powder indicated as "planetary mill" was ball milled for 48h and milled in a planetary mill for 6h, and the powder indicated as pH was ball milled for 48h, milled in a planetary mill for 6h and the pH was adjusted to 2.28.

Surface area measurements

3 slurries were dried in a furnace to give Al_2O_3 powders. This included the slurry that was ball milled for 48h, the slurry that was additionally milled in a planetary mill for 6h, and the slurry where the pH was additionally adjusted. The surface area of the original powder along with the 3 dried powders was measured by BET theory. Table 5.6 shows the measured micropore area, external surface area and total BET surface area. The total BET surface area is a sum of the micropore area and the external surface area.

5.4.2 Polymer adsorption

PAA adsorption on α-Al_2O_3 was first tested by TGA. The adsorption was carried out, and the liquid centrifuged and filtrated prior to the TGA measurement. Figure 5.23 shows the TGA graphs of the adsorption carried out with (a) the PAA concentration 1mg/g and (b) the PAA concentration 5mg/g and measured by TGA method 3. Figure 5.23 (c) also shows TGA measurement of the 5mg/g PAA concentration but measured by TGA method 4. By comparing figure 5.23 (b) with (c) it can be seen that the choice of TGA method affects the measured evaporation temperature; $\approx 160°$C as measured by method 3 shown in figure 5.23 (b) and $\approx 100°$C as measured by method 4 shown in figure 5.23 (c). The resolution in method 4 is higher than that in method 3, heating rate $1°$/min vs. $4°$/min. It is believed that the evaporation temperature should be $\approx 100°$C as the solution mainly contains water. Further measurements were therefore only run by method 4. Figure 5.23 shows anyhow that that practically all the liquid evaporates. This can mean that all the polymer is adsorbed, or the unadsorbed polymer is retained on the filter.

	1,0wt% PAA	1,0wt% PEI
Unfiltrated	1.3337	1.3345
Filtrated	1.3338	1.3343

Table 5.7: The table shows the measured refractive index of unfiltrated and filtrated 1.0wt% PAA and PEI standard solutions.

| Concentration (mg/g)	Refractive index
1	1.3324
2	1.3324
3	1.3324
5	1.3324
10	1.3324
20	1.3325
30	1.3325

Table 5.8: The table shows the measured refractive index of all the prepared polymer concentrations.

The 2.5wt% PAA standard solution was also filtrated and the liquid analysed in the TGA to check if possibly the polymer was retained on the filter. Figure 5.24 shows TGA graphs of (a) the 2.5wt% PAA standard solution and (b) the filtrated 2.5wt% PAA standard solution. Both figures show a gradual weight loss. This indicates that it could be difficult to analyse the polymer adsorption accurately using TGA. Measurements of the refractive index are believed to be a more accurate method.

Figure 5.25 shows the calibration curve for the PAA system, while figure 5.26 shows the calibration curve for the PEI system. Then, the 1.0wt% standard solutions of PAA and PEI were filtrated through a 0.025μm Millipore filter to again check whether the polymer was retained on the filter. The measured refractive index' are shown in table 5.7. These results show that the polymer is not retained on the filter.

In the end, the refractive index of the prepared polymer concentrations were measured. These results are shown in table 5.8. The refractive index of water was measured to 1.3324.
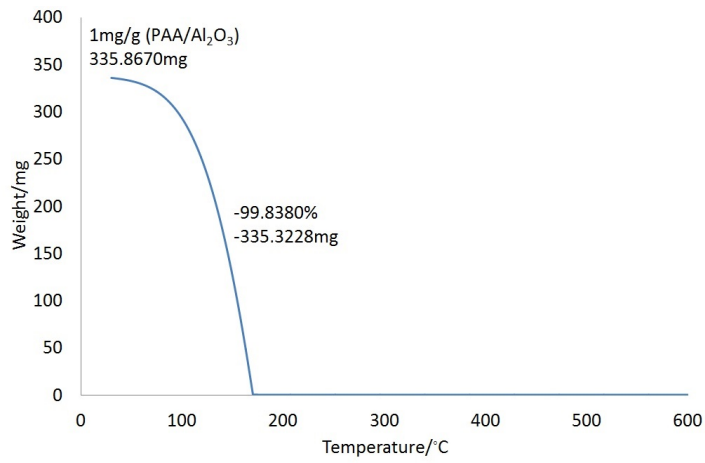
(a)
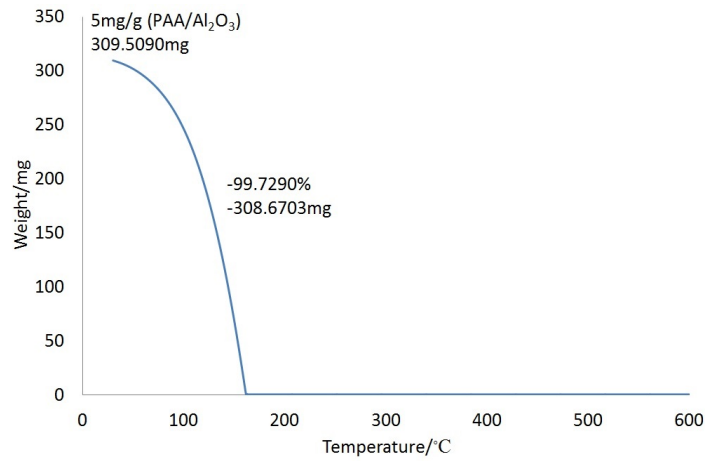
(b)
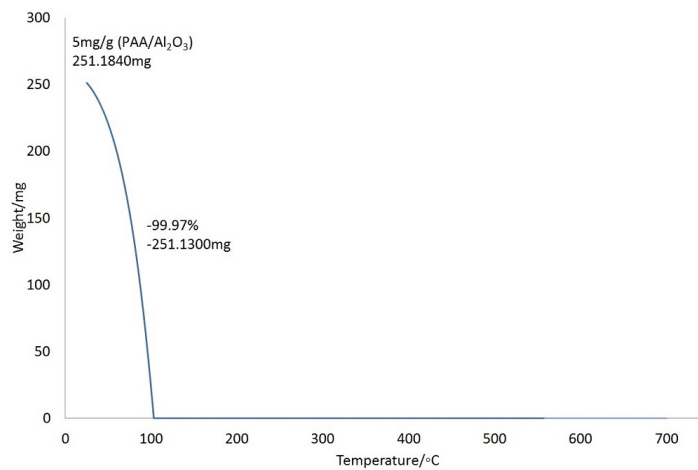
(c)

Figure 5.23: TGA graphs showing weight loss as a function of temperature of **(a)** 1mg/g (PAA/α-Al$_2$O$_3$), **(b)** 5mg/g (PAA/α-Al$_2$O$_3$) measured by TGA method 3 and **(b)** 5mg/g (PAA/α-Al$_2$O$_3$) measured by TGA method 4.
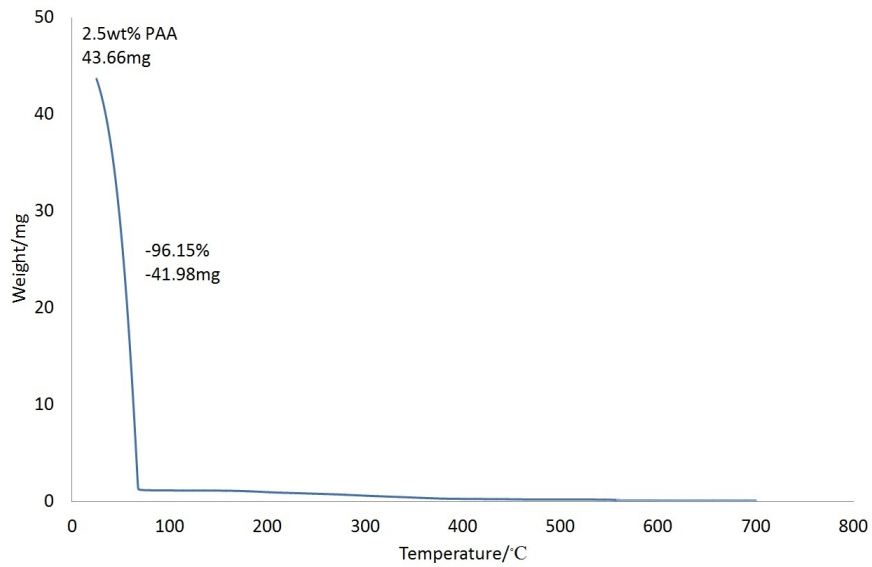
(a)
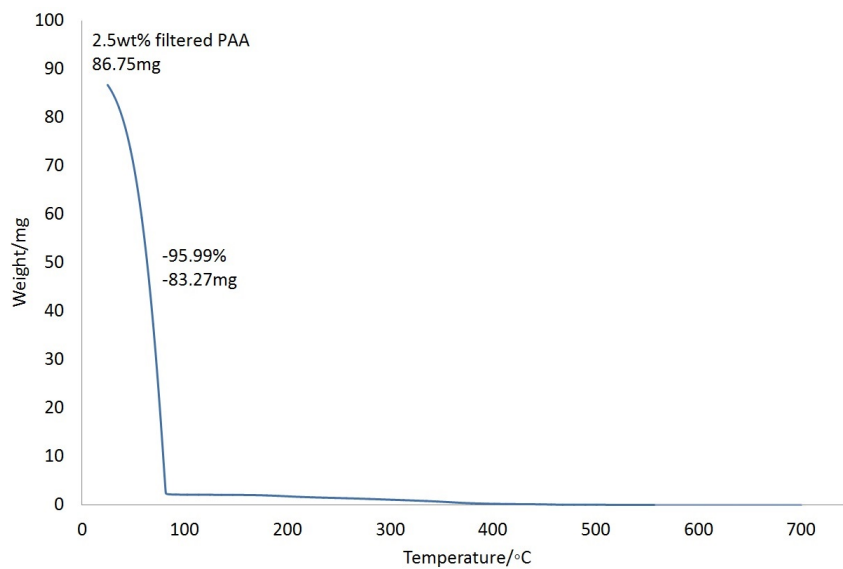
(b)

Figure 5.24: TGA graphs showing weight loss as a function of temperature of **(a)** 2.5wt% PAA standard solution and **(b)** filtrated 2.5wt% PAA standard solution.
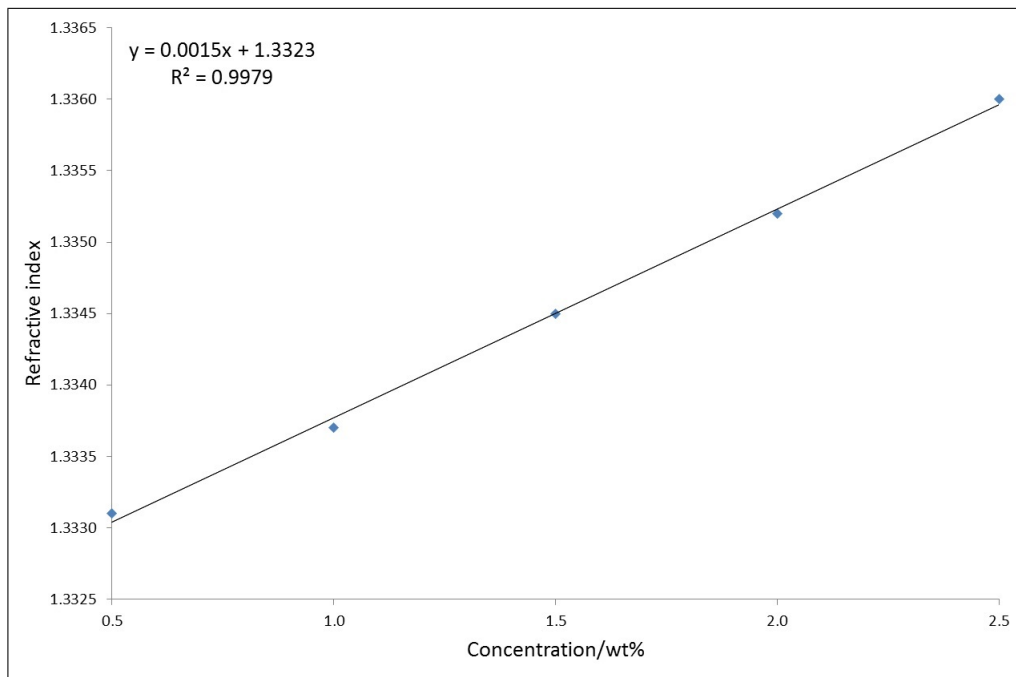
Figure 5.25: Calibration curve for the PAA system showing the refractive index as a function of standard solution wt%.
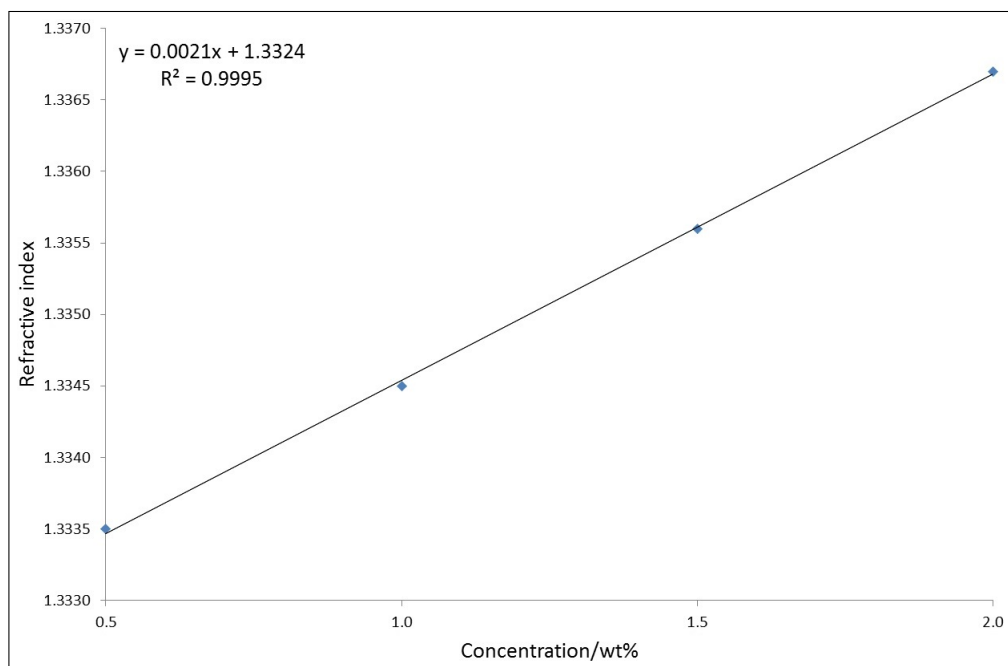
Figure 5.26: Calibration curve for the PEI system showing the refractive index as a function of standard solution wt%.

Chapter 6

Discussion

6.1 Catalyst characterisation

6.1.1 $Co_{3-x}Mn_xO_4$ catalyst

The spinel $Co_{3-x}Mn_xO_4$ was synthesised by coprecipitation. It was intended that the coprecipitation would be carried out with a 0.5M Mn/Co solution and 2M NH_4HCO_3. XRF measurements showed however that the concentration of Mn and Co in the solution was not 0.5M. The largest deviation was found for cobalt, 0.3469M instead of 0.5M. TGA measurements showed that the water content in $Co(NO_3)_2 \cdot xH_2O$ was slightly less than stated by the manufacturer, $5.6H_2O$ instead of $6H_2O$, leading to the conclusion that the measured concentration of Co in the standard solution should be higher than 0.5M. These results do not provide a clear explanation to why the Mn/Co concentration is not 0.5M.

The Co(Co+Mn) ratio in the metal solution that was prepared was calculated to 0.45. The phase diagram of the Mn-Co-O system, figure 4.3 on page 45, shows that a spinel phase forms above 750°C. However, the powder was first heated up to 700°C, then to 900°C, and then to 1100°. The phase diagram shows that at 700°C and for a Co/(Co+Mn) ratio of 0.45 a boundary between two two-phase regions Mn_3O_4 (hausmannite) and a spinel as well as a spinel and α-Mn_2O_3 is reached. Only the spinel phase forms at 900°C and 1100°C.

Mn_3O_4 has a body-centered tetragonal crystal lattice with space group I41/amd and cell parameters a = 5.752A and c = 9.4696A, while the spinel has a cubic crystal lattice and space group Fd$\bar{3}$m. The XRD of the catalyst powder, figure 5.3 on page 66, does in fact show formation of two phases. $CoMn_2O_4$ with a body-centered tetragonal crystal lattice, space groupe I41/amd, cell parameters a = 5.784A and c = 9.091A and $MnCo_2O_4$ with a cubic crystal lattice, Fd$\bar{3}$m space group and cell parameter a = 8.28A are indicated in the diffractogram. It is clear that the composition of the two indicated phases are not accurate to the ones present in the catalyst powder. The peaks that can be related to $MnCo_2O_4$ are shifted to the right towards smaller d-values. This indicates that the crystal lattice is contracted, which again indicates substitution of

Co with Mn. Moreover, $MnCo_2O_4$ is a cubic spinel with space group $Fd\bar{3}m$. This corresponds well with the data in the phase diagram. These results support that the catalyst phase formed is a cobalt rich spinel of the form $Co_{3-x}Mn_xO_4$. The remaining peaks were hard to identify. $CoMn_2O_4$ was found to be the best fit even though it does not provide a plausible explanation of all the peaks. For example, the peak at $2\theta \approx 38.2°$ is shifted to left, while the peak at $\approx 42.5°$ is shifted to the right. However, the rest of the remaining peaks are well explained by this phase. $CoMn_2O_4$ has a body-centered tetragonal crystal lattice and space group $I41/amd$, the same as the hausmannite. The second phase is therefore believed to be a cobalt substituted hausmannite, $Mn_{3-x}Co_xO_4$. For simplicity, the powder is assigned as Co-Mn-O which is meant to indicate that more than one phase is present.

There is an alternative explanation to why two phases may form during catalyst synthesis. A single phase could have been formed at 900° and 1100°, but two phases are formed upon cooling in the furnace. According the the phase diagram, formation of $CoMnO_3$ and α-Mn_2O_3 could be expected. The d-values of these two phases are however not a good match to the d-values of the catalyst powder.

6.1.2 $LaMnO_3$ **catalyst**

The $LaMnO_3$ catalyst was synthesised by the sol-gel method. Two of the additives are citric acid and ethylene glycol, which should be added in a ratio of 2:3. The amount of ethylene glycol was miscalculated. If the amount of citric acid is 0.75mol, the amount of ethylene glycol should be 0.50mol ($0.75 \cdot \frac{2}{3}$). However 1.125mol was added ($0.75 \cdot \frac{3}{2}$). The XRD diffractogram, figure 5.5 on page 69, shows that the phase formed is $La_{0.969}Mn_{0.93}O_3$. The calculation error can explain the altered composition of the catalyst powder as the composition of the gel itself is altered by adding too much ethylene glycol. The $La_{0.969}Mn_{0.93}O_3$ phase has a rhombohedral crystal lattice with space group $R\bar{3}c$ and cell parameters a = 5.5222A and c = 13.3317A. The targeted structure type was a perovskite. Several phases with a different composition than $La_{0.969}Mn_{0.93}O_3$ do have a perovskite type structure. The deviation from the targeted structure type may be explained by the miscalculation of the correct amount of ethylene glycol.

6.2 Pt-reference layer

The sintering temperatures were chosen out of the Hüttig and Tamman temperatures for platinum, see section 4.3, and the platinum thin film was deposited on two different support materials, α-Al$_2$O$_3$ and YSZ. Figure 5.6 and figure 5.7 show the effect of different sintering temperatures on the formation of Pt-particles on the α-Al$_2$O$_3$ (0001) and YSZ (100) surface, respectively. The behaviour of the Pt-particles below 650°C is clearly different. This is probably because the surface free energy, γ, of the two support materials is different. The surface free energy has an important impact on sintering. The surface free energy is also not only dependent on the material but also on the orientation of the crystal [73]. It is documented that the value of the surface free energy varies by several percent for different surface orientations at temperatures near the melting point of the material. The surface energy of solid materials can be found by cleavage experiments. These experiments have not been performed in this work as the nature of the particle formation has not been in focus. Some general explanations on the formation of Pt-particles are however described in the following text.

SEM images show that the spreading of the platinum thin film is different for the two surfaces below 650°C. Images shown in figure 5.7 (a) and (b) show formation of large particles on the YSZ surface, much similar to drops on a solid surface, indicating that the film does not completely wet the surface. In contrary, images shown in figure 5.6 (a) and (b) show complete wetting of the α-Al$_2$O$_3$ surface by the platinum film. The formation of platinum particles by sintering starts at 650°C for both support materials. This indicates that when the temperature is high enough, the behaviour of the platinum atoms on the surface is no longer dependent on the surface energy of the support materials, but rather on the mobility of platinum atoms. This can be compared to an energy barrier that needs to be overcome in order to form platinum particles on the surface. Both figures 5.6 (d) and 5.7 (d) also show that the particle size is not uniform. This is probably because particle growth is governed by Oswald ripening.

Figure 5.8 shows the formation of platinum particles when the film thickness is 2.5nm and 5nm and sintering temperature is 770 °C. As can be expected, the density of the formed platinum particles is higher when the thickness of the deposited film increases.
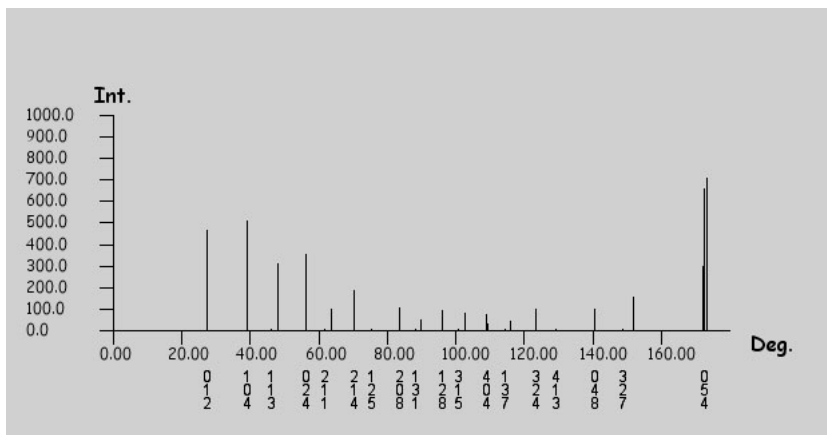
6.3 Characterisation of interface layers

6.3.1 $La_{0.969}Mn_{0.93}O_3/\alpha$-$Al_2O_3$ interface

The EDS measurements, shown in table 5.2 on page 74, show that three elements are present in the interface layer, aluminium, lanthanum and manganese. Moreover the atom% of La and Mn are similar. Only one phase that contains these three elements in addition to oxygen was found, $LaMnAl_{11}O_{19}$ with a hexagonal crystal lattice, space group P63/mmc and cell parameters a = 5.574A and c = 22.008A. This phase is indicated in the diffractogram in figure 5.10 on page 76, along with the phases $LaAlO_3$ with a rhombohedral crystal lattice, space group R3m and cell parameter a = 3.789A and $La_{0.951}Mn_{0.951}O_3$ with a rhombohedral crystal lattice, space group R$\bar{3}$c. $La_{0.951}Mn_{0.951}O_3$ was indicated to check if some of the peaks could be explained by the presence of the catalyst that has not reacted with the support. This, however, is not the case. There should, for example, be observable peaks at $2\theta \approx 26.5°$ and $2\theta \approx 47°$. Peaks explained by the phase $LaMnAl_{11}O_{19}$ are shifted to the left towards higher d-values. This also apllies to peaks from $La(AlO_3)$. There could be several reasons for this as explained in section 5.3.1. The $La(AlO_3)$ phase should have an observable peak at $2\theta \approx 27.5°$, which is not found in the diffractogram. It is however believed that a modified perovskite $LaAlO_3$ could have been formed. Figure 6.1 shows simulated powder diffraction pattern of $LaAlO_3$ and $LaAl_{0.5}Mn_{0.5}O_3$ using Jems Software. The simulated patterns show that the d-values do not change much when Al is substituted with Mn. This means that also a modified perovskite $LaAl_{1-x}Mn_xO_3$ is possibly formed at the interface.

The interface was also studied with TEM. The diffraction patterns are not obtained with kinematic conditions. A diffraction pattern of Al_2O_3 along the [1 $\bar{1}$ 0] zone axis was also modelled with Jems and is shown in figure 6.2 (a). The figure shows that the (003) reflection has very low intensity, while the intensity of the (003) reflection in the acquired diffraction pattern, figure 4.9 on page 57, has a relatively high intensity. This indicates dynamic scattering. Figure 6.2 (b) shows the simulated diffraction pattern of the $La_{0.969}Mn_{0.93}O_3/\alpha$-$Al_2O_3$ interface along the [1 $\bar{1}$ 0] zone axis. The table d-values of $LaMnAl_{11}O_{19}$ according to the planes observed in the diffraction pattern of the interface layer are d_{002} = 11.004A, d_{110} = 2.787A and d_{112} = 2.702A. These d-values lie between the d-values calculated for L=42cm and L=50cm, table 5.3 on page 75.

These results combined indicate that the phase formed at the $La_{0.969}Mn_{0.93}O_3/\alpha$-

(a)
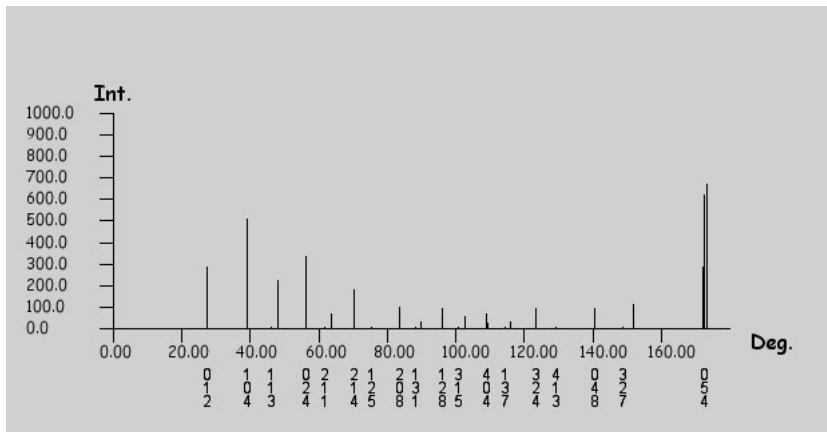
(b)

Figure 6.1: Powder diffraction patterns of **(a)** $LaAlO_3$ and **(b)** $LaAl_{0.5}Mn_{0.5}O_3$ simulated with the Jems Software.
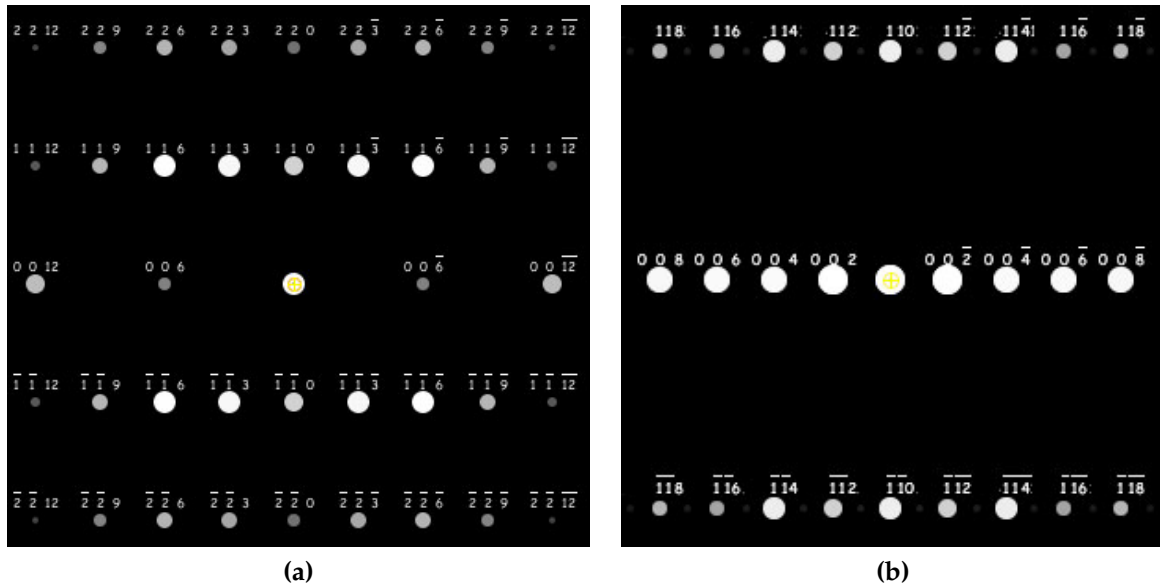
Figure 6.2: Diffraction patterns along the [1 $\bar{1}$ 0] zone axis of **(a)** α-Al$_2$O$_3$ and **(b)** La$_{0.969}$Mn$_{0.93}$O$_3$/α-Al$_2$O$_3$ interface simulated with the Jems Software.

Al$_2$O$_3$ interface is LaMnAl$_{11}$O$_{19}$ and possibly also a modified perovskite LaAl$_{1-x}$Mn$_x$O$_3$. The latter was, however, not observed in the TEM. EDS measured at two different boundary positions showed that the elemental composition did not vary by more than a few atom% throughout the interface layer. This indicates that all the catalyst layer has interacted with the support, i.e. both diffusion of La and Mn into the α-Al$_2$O$_3$ support, as well as diffusion of Al into the La$_{0.969}$Mn$_{0.93}$O$_3$ catalyst. The thickness of the interface layer is estimated to $\approx$50-100μm.

6.3.2 Co-Mn-O/α-Al$_2$O$_3$ interface

The XRD of the Co-Mn-O/α-Al$_2$O$_3$ interface layer is shown in figure 5.13 on page 78. A reference was not used during the measurement, so three possible phases are indicated in the diffractogram; MnCo$_2$O$_4$ with a cubic crystal lattice, space group Fd$\bar{3}$m and cell parameter a = 8.28A, CoCo$_2$O$_4$ with a cubic crystal lattice, space group Fd$\bar{3}$m and cell parameter a = 8.0837A and (Mn$_{0.89}$Al$_{0.11}$)Al$_2$O$_4$ with a cubic crystal lattice, Fd$\bar{3}$m space group and cell parameter a = 8.181A. All three phases have a cubic crystal lattice with space group Fd$\bar{3}$m and all three can potentially described the diffraction peaks of the interface layer by a left of right displacement. Some differences can be revealed by a more detailed inspection of the diffractogram. Both MnCo$_2$O$_4$ and CoCo$_2$O$_4$ have peaks at 2θ $\approx$44$°$ and 2θ $\approx$45$°$ respectively. No peak is observed in the diffraction pattern at these angles. MnCo$_2$O$_4$ and CoCo$_2$O$_4$ have also peaks at 2θ $\approx$21.5$°$ and 2θ $\approx$22$°$ with intensities similar to the (Mn$_{0.89}$Al$_{0.11}$)Al$_2$O$_4$ peak at

$2\theta \approx 65°$. A peak at $2\theta \approx 22°$ is not observed in the interface layer pattern, but is observed at $2\theta \approx 65°$. Moreover, the $(Mn_{0.89}Al_{0.11})Al_2O_4$ has a low intensity peak at $2\theta \approx 57°$. A formation of a low intensity peak is indicated in the interface layer pattern although the signal-to-noise ratio is poor. The peak at $2\theta \approx 46.5°$ is a background peak from Blu Tack which was used to attach the sample to the sample holder. The peak at $2\theta \approx 72.5°$ is also a background peak, but in this case, from the α-Al_2O_3 support.

The XRD results indicate that the phase formed at the Co-Mn-O/α-Al_2O_3 interface is galaxite with the composition $(Mn_{0.89}Al_{0.11})Al_2O_4$. However, EDS data, table 5.4 on page 78, show that also Co is present in the interface layer. The content of Mn and Co is measured to 14.54 atom% and 15.71 atom%, respectively, suggesting that the amount of Mn and Co in the interface phase is similar. Figure 6.3 shows a simulated powder diffraction pattern of $(Mn_{0.89}Al_{0.11})Al_2O_4$ and $(Mn_{0.44}Co_{0.45}Al_{0.11})Al_2O_4$ using Jems Software. The simulated patterns show that the position of the peaks in the diffractogram is not very much affected by Co substitution of Mn in the galaxite $(Mn_{0.89}Al_{0.11})Al_2O_4$.

D-values calculated from the TEM diffraction patterns do not match those of $(Mn_{0.89}Al_{0.11})Al_2O_4$. D-values closest to those in table 5.5 on page 79 are $d_{220} = 2.89A$, $d_{311} = 2.46A$ and $d_{400} = 2.05A$. The deviation from the values in table 5.5 is considered to be too large, also none of the planes (220), (311) and (400) are perpendicular to each other and none are a sum of the other two. Calibrated camera lengths were used in the calculation, so that the deviation from the true value should be smaller than that in the diffraction pattern from the $La_{0.969}Mn_{0.93}O_3$/α-Al_2O_3 interface layer. D-values of $MnCo_2O_4$ and $CoCo_2O_4$ are similar to those of $(Mn_{0.89}Al_{0.11})Al_2O_4$ for the same planes. The largest deviation is 0.04A, meaning that the diffraction pattern does not correspond to these phases either. Moreover, the calculated d-values do not match those of the support, α-Al_2O_3.

XRD results support formation of galaxite with the composition $(Mn_{0.89}Al_{0.11})Al_2O_4$. EDS results also show that the phase contains Co. Figure 6.3 shows that the substitution of Mn with Co does not change the d-values substantially. Unfortunately, TEM results are not in compliance with the XRD results. It is at this point unclear which phase the diffraction pattern is describing. However, XRD results combined with EDS present evidence that the phase formed at the Co-Mn-O/α-Al_2O_3 interface is a cobalt substituted galaxite with the composition $(Mn_{0.89}Al_{0.11})Al_2O_4$. EDS measured at both sides of the Pt-reference show that the elemental composition did not
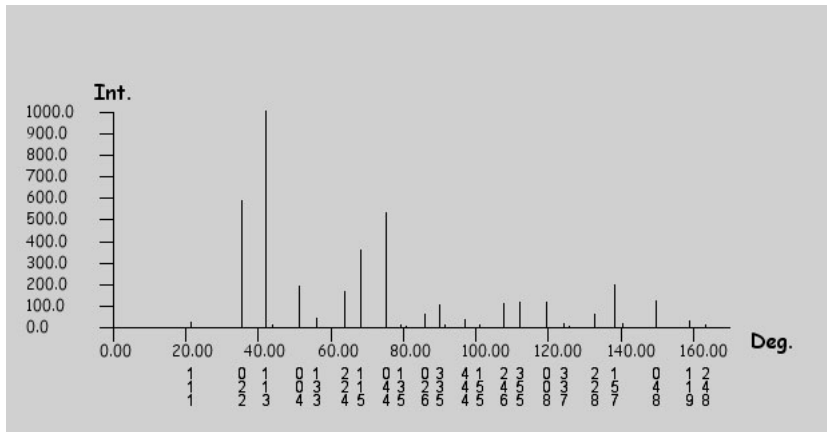
(a)
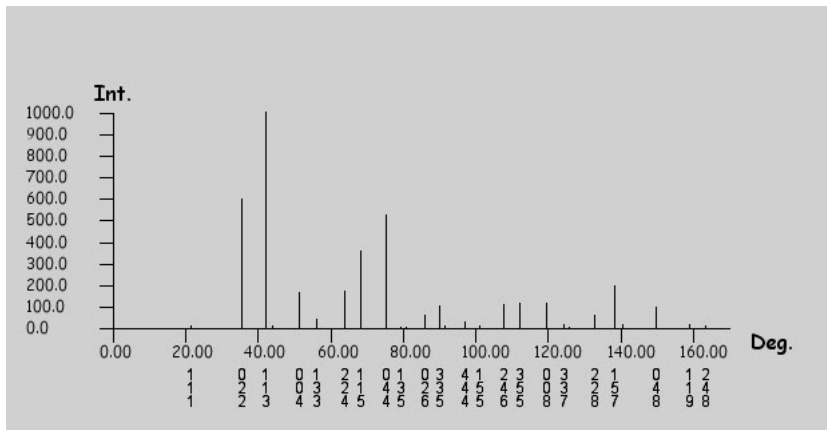
(b)

Figure 6.3: Powder diffraction patterns of **(a)** $\left(Mn_{0.89}Al_{0.11}\right)Al_2O_4$ and **(b)** $\left(Mn_{0.44}Co_{0.45}Al_{0.11}\right)Al_2O_4$ simulated with the Jems Software.

vary by more than a few atom%. This indicates both diffusion of Mn and Co into the α-Al$_2$O$_3$ support, as well as diffusion of Al into the Co$_{3-x}$Mn$_x$O$_4$ catalyst. The thickness of the interface layer is estimated to $\approx$5-8μm. This is substantially thinner that that of the La$_{0.969}$Mn$_{0.93}$O$_3$/α-Al$_2$O$_3$ interface ($\approx$50-100μm). This can be explained by a more severe interaction taking place at the La$_{0.969}$Mn$_{0.93}$O$_3$/α-Al$_2$O$_3$ interface, but the density of the catalyst powder in the catalyst ink should also be taken into account. During catalyst preparation extra amounts of the solvent trichloroethylene than that indicated in tables 4.3 and 4.4 on page 53 was added. The extra amount of tricholoethylene added to 5.11g of Co-Mn-O powder was 6.9g, while the extra amount added to 20.15g of La$_{0.969}$Mn$_{0.93}$O$_3$ powder was 7.31g. This means that a larger relative amount of solvent was used during Co-Mn-O ink preparation leading to a lower amount of catalyst deposited on the α-Al$_2$O$_3$ surface. EDS data suggest that all the deposited catalyst had interacted with the α-Al$_2$O$_3$ support, meaning that the Co-Mn-O/α-Al$_2$O$_3$ interface layer could have been thicker if a larger amount of catalyst was initially deposited.

6.4 Particle downsizing and polymer adsorption

6.4.1 Downsizing of Al$_2$O$_3$ particles

Figures 5.15 - 5.18 show the α-Al$_2$O$_3$ particle size measured by laser diffraction after various milling steps and analysed by Fraunhofer approximation and Mie theory. The Fraunhofer approximation is evidently easier to use since no optical property information is required. However, the theory can sometimes lead to significant errors. In general, the Fraunhofer approximation can only be used if the particles are large compared to the wavelength of light or if the ratio of the refractive indexes of the dispersed and continuous phase is different from 1 [74]. In addition, the theory is likely to give errors if [75]:

1. The particles are transparent (absorption coefficient < 0.2). In this case the Fraunhofer approximation will tend to give inaccurate results for particle sizes < 50μm. On the other hand, if the absorption is high (absorption coefficient > 0.2) good results can be obtained down to 2μm.

2. The particle size distribution contains particles that are smaller than 2μm. Here, the Fraunhofer approximation will lead to an over- or underestimation of the fine particle regions.

In the case of the measurements on the α-Al$_2$O$_3$ particles, figure 5.15 shows that the particle size is much larger than the wavelength of the laser light (633nm). The refractive index of the α-Al$_2$O$_3$-particles is 1.76. The powder was dispersed in water with refractive index of 1.33. The ratio between the these two refractive indexes is 1.32 clearly different from 1. The general requirements of the Fraunhofer approximation are therefore met.

The Mie theory is in general always correct if the optical information required is known. In this work, the absorption coefficient of the powder was not known, but was assumed to be very low. The absorption coefficient was therefore set to 0.01. It is not believed that this estimation has led to errors in the measurements.

Even though the particles can be defined as transparent, there is good consistency between the diameter at 10%, 50% and 90% values as analysed by Mie and Fraunhofer theory, see figures 5.15-5.17, even though the particle size is <50μm. However, there are discrepancies regarding the particle size distributions. The difference is largest in figure 5.17 showing the particle size measured after 24h of ball milling with a dispersant. This is believed to be because the Fraunhofer approximation is in general more inaccurate than the Mie theory when the particles become small. Otherwise, both under- and overestimation of the fine particle region (0.1μm-1.0μm) is observed when comparing the results obtained by Fraunhofer approxmation to the Mie theory, figure 5.15 and 5.16 respectively.

In this work, both theories have their uncertainties. The absorption coefficient used in the Mie theory is estimated, while the Fraunhofer approximation is inaccurate in the fine particle region which is of interest here. It is not believed that this has had a significant impact on the assessment of the downsizing effect of the α-Al$_2$O$_3$ particles as the method of particle size measurement was changed from laser diffraction to dynamic light scattering.

Figure 5.19 - 5.22 show the change in the particle size and particle size distribution when the slurry was milled in a planetary mill. Finally, a unimodal particle size distribution with a Z-average of 257.7nm is obtained after 48h of milling in a ball mill, followed by 6h of milling in a planetary mill and adjusting the pH to 2.22. There are no particular uncertainties in these measurements.

Table 5.6 on page 90 shows that the measured BET surface area during milling increases. The BET surface area of α-Al$_2$O$_3$ particles was 5.18m^2/g prior to the milling, 5.79m^2/g after 48h of ball milling, 18.8m^2/g after additional 6h of milling in a planetary mill and 30.4m^2/g after additional pH adjustement. The increase in the BET surface area show that new surface is created during each milling step, as opposed to just re-agglomeration of agglomerated particles.

6.4.2 Polymer adsorption

Initially, concentrations between 1-5mg/g (PAA/α-Al$_2$O$_3$) were tested. The tested concentrations were based on the work done by Chen *et al.* on adsorption of PAA on the α-Al$_2$O$_3$ surface [76]. The α-Al$_2$O$_3$ powder they used had a specific surface area of 6.4 m^2/g, the dispersion contained a 30vol% solid-loading and the molecular weight of the polymer was 5000. Full saturation of the α-Al$_2$O$_3$ particle surface was achieved for the concentration of 4mg/g. As table 5.6 on page 90 shows the α-Al$_2$O$_3$ particles used in this work had a surface area of 5.18 m^2/g, the dispersion contained a 10vol% solid-loading and the molecular weight of the polymer was 2000. A lower polymer concentration was expected in order to achieve full saturation of the polymer surface.

The adsorption of PAA on the surface of α-Al$_2$O$_3$ particles was first studied by TGA. It was believed that the polymer that was not adsorbed, and hence still present in the liquid, would be reduced at a certain temperature leading to a sharp weight drop in the TGA graph. This was however not observed, see figure 5.23. At this point there could be two reasons for this, either all the polymer is adsorbed or the unadsorbed polymer is retained on the filter. TGA measurements of the 2.5wt% PAA solution, see figure 5.24, led to the conclusion that TGA is not a suitable method to measure the amount of adsorbed polymer. A gradual decline, rather than a sharp drop, is observed in the TGA graph. This is probably because the polymer weight is not constant. Further analysis of the polymer adsorption continued by measuring the refractive index of the liquid. Calibration curves of both PAA and PEI systems were obtained out of the prepared standard solutions. The calibration curves are shown in figure 5.25 and 5.26 and show that the measurement of refractive index provide a method sensitive enough to detect the low concentrations of the polymers. Moreover, table 5.7 shows that PAA is not retained on the filter. The refractive index of the initial polymer concentrations (1-5mg/g) as well as concentrations 10, 20 and 30mg/g were measured. In the same experiment, the refractive index of water was measured to 1.3324. Table 5.8 shows that the refractive index or the liquid for polymer concentrations of 1-10mg/g is 1.3324, meaning that there is no polymer in the liquid i.e. all the polymer is ad-

sorbed. The refractive index of the solutions with concentrations 20 and 30mg/g is 1.3325. The uncertainty in the measurement is ± 0.0001, so this does not necessarily lead to the conclusion that the α-Al$_2$O$_3$ particle surface is becoming saturated.

The polymer concentrations tested here are far higher than those tested by Chen *et al.* even when the specific surface of the particles as well as vol% loading is lower [76]. This can be explained by the difference in the molecular weights of the polymer. Polymer adsorption is a complex process and several polymer conformations on the surface are possible. These include for example tail, loop, flat and spherical conformations [53]. The change in conformation of the polymer on the surface of α-Al$_2$O$_3$ particles will have a significant impact on the polymer concentration needed to achieve saturation of the particle surface.

The main focus of this part of the work was to find the polymer concentration of PAA and PEI at which the surface of the α-Al$_2$O$_3$ is saturated. Even though this is not accomplished, a good method on how future experiments can be planned is outlined. Out of the experience with this work, it also seems as filtering is not necessary to separate the powder from the liquid. Centrifugation is much more efficient, 5min at 3000rpm should be sufficient for particles of similar size as used in this work. Omitting the filtering may simplify eventual future experiments. It is also important to note that Chen *et al.* have shown that the conformation of the adsorbed polymer on the particle surface, and thus the amount of polymer adsorbed, is dependent on the pH [76]. This may be of significance if future experiments include polymer adsorption on downsized α-Al$_2$O$_3$ particles stabilized by lowering the pH.

Chapter 7

Conclusion

The experimental work of this thesis includes several parts. First, two catalyst were synthesised each by a different method (coprecipitation and sol-gel method). The XRD results of the catalyst synthesised by the coprecipitation method showed that the catalyst powder contained two phases. A cobalt-rich phase, $Co_{3-x}Mn_xO_4$, with a cubic crystal lattice assigned by the space group $Fd\bar{3}m$ and a manganese rich phase, $Mn_{3-x}Co_xO_4$, with a body-centered tetragonal crystal lattice assigned by the space group I41/amd. For simplicity, the powder is assigned as Co-Mn-O which is meant to indicate that more than one phase is present. The catalyst synthesised by the sol-gel method was found to contain one phase, $La_{0.969}Mn_{0.93}O_3$ with a rhombohedral crystal lattice assigned by the $R\bar{3}c$ space group and cell parameters a = 5.5222A and c = 13.3317A.

It was found that a reference layer of small platinum particles, which would mark the original catalyst-support interface, could be formed by deposition of a 5nm platinum layer on single crystals of YSZ and α-Al_2O_3 and sintering at 770° for 4h. A catalyst ink formed from the synthesised catalyst powders was made, painted on the single crystals and annealed.

XRD, EDS and TEM results show that the phase formed at the $La_{0.969}Mn_{0.93}O_3/\alpha$-$Al_2O_3$ interface is $LaMnAl_{11}O_{19}$ with a hexagonal crystal lattice, space group P63/mmc and cell parameters a = 5.574A and c = 22.008A. XRD and EDS results also support formation of a a modified perovskite $LaAl_{1-x}Mn_xO_3$ with a rhombohedral crystal lattice and space group R3m. The platinum reference layer could not be identified in the SEM images of the $La_{0.969}Mn_{0.93}O_3/\alpha$-$Al_2O_3$ sample, probably due to poor contrast between Pt and La. EDS measurements at two boundary positions, one close to the pure α-Al_2O_3 support and one close to the catalyst surface, show that there is diffusion of La and Mn into the α-Al_2O_3 support and diffusion of Al into the catalyst. The thickness of the $La_{0.969}Mn_{0.93}O_3/\alpha$-$Al_2O_3$ interface layer is estimated to $\approx$50-100μm.

XRD and EDS results of the Co-Mn-O/α-Al_2O_3 interface layer show that the phase formed is a cobalt substituted galaxite with the composition $(Mn_{0.89}Al_{0.11})Al_2O_4$ with a cubic crystal lattice, $Fd\bar{3}m$ space group and cell parameter a = 8.181A. This was not

supported by TEM. The Pt-reference layer was identified on SEM images. EDS measurements on both sides of the reference layer show that there is a diffusion of Co and Mn into the α-Al$_2$O$_3$ support as well as diffusion of Al into the catalyst. The thickness of the Co-Mn-O/α-Al$_2$O$_3$ interface layer is estimated to $\approx$5-8μm.

Downsizing of α-Al$_2$O$_3$ particles has revealed that the particles start to agglomerate after wet milling. This can be prevented if pH is lowered to approximately 2.3. The surface of oxide particles in acidic environments is negative, leading to stabilisation by electrostatic effects. BET results show that the specific surface area of the α-Al$_2$O$_3$ was 5.18m^2/g prior to the milling, 5.79m^2/g after 48h of ball milling, 18.8m^2/g after additional 6h of milling in a planetary mill and 30.4m^2/g after additional pH adjustement. The increase in the BET surface area show that new surface is created during each milling step, as opposed to just re-agglomeration.

TGA proved to be a too insensitive method to measure polymer adsorption of PAA on the α-Al$_2$O$_3$ particles. It is shown that measurements of the refractive index provide the correct sensitivity. The adsorption experiments are not completed in this work, but a good methodology is outlined for eventual further work.

Chapter 8

Further work

The project motivation is described in section 1.4. Unfortunately, it has not been possible to finish the project within the scope of this master thesis. The catalyst coated YSZ single crystals are prepared, but still need to be analysed. Preliminary sample preparation for SEM has shown that YSZ is a more brittle material than α-Al$_2$O$_3$, making it more difficult to polish the samples. Adjustments to the sample preparation method used for catalyst coated α-Al$_2$O$_3$ single crystals will have to be made.

The main objective of the project is to identify the effectiveness of a barrier layer that can prevent/minimize catalyst-support interactions under high temperature conditions. Before the barrier layer can be deposited, polymer adsorption on α-Al$_2$O$_3$, YSZ and the selected barrier material powders needs to be investigated. A good methodology on the downsizing of α-Al$_2$O$_3$ particles is established in this work. The method is general to all oxide particles and can be used if the YSZ particles also need to be downsized. Due to the amount of work that remains it is recommended that manufactured powders, both YSZ and barrier material, with the desired particle size are obtained. The polymer concentrations in the solutions used to carry out polymer adsorption of oxide particles is low. This work has shown that refractive index measurements provide a method sensitive enough to measure the polymer that has not been adsorbed by the particles. It is important that the single crystal surface and the surface of the barrier layer particles have opposite charges at a common pH. This can be analysed by zeta potential measurements of the powder particles after polymer adsorption. Once opposite charges are generated, the single crystals can be dip-coated into a dispersion containing the barrier material particles. The idea is that a monolayer of barrier particles will form after sintering. This can be investigated by SEM. Catalyst inks were made in this work. There should be enough ink left for the coating of single crystals with a barrier layer. The samples should, of course, be annealed in the same was as the samples analysed in this work.

It is recommended to divide the rest of the work into two projects. Since it takes some time to find a good sample preparation method for TEM samples and it also takes time to become familiar with the instrument, it is recommended that one project should only include TEM characterization of catalyst-support and catalyst-barrier-support in-

terface layers. The other project should include the work that needs to be done in order to deposit the barrier layer on the single crystals and possibly also the analysis of the interface layers by SEM and XRD. Moreover, another reference marker than Pt-particles should be used for the samples with the $La_{0.969}Mn_{0.93}O_3$ catalyst since the reference layer could not be identified by SEM analysis due to poor contrast between Pt and La. The effectiveness of a barrier layer will be hard to identify if the position of the original catalyst-support interface is not known.

Appendix A

TGA methods

Method 1:

- Temperature range: 30-1100°C

- Hold: 30min at 1100°C

- Heating rate: 1°/min

- Airflow: 50ml/min

Method 2:

- Temperature range: 30-500°C

- Heating rate: 4°/min

- Airflow: 50ml/min

Method 3:

- Temperature range: 30-600°C

- Heating rate: 4°/min

- Airflow: 50ml/min

Method 4:

- Temperature range: 25-700°C

- Heating rate: 1°/min

- Airflow: 50ml/min

Method 5:

- Temperature range: 30-1100°C

- Heating rate: 4°/min

- Airflow: 50ml/min

Bibliography

[1] P. Forster, V. Ramaswamy, P. Artaxo, T. Berntsen, R. Betts, D.W. Fahey, J. Haywood, J. Lean, D.C. Lowe, G. Myhre, J. Nganga, R. Prinn, G. Raga, M. Schulz, and R. Van Dorland. Changes in atmospheric constituents and in radiative forcing. in: Climate change 2007: The physical science basis. Contribution of working group 1 to the fourth assessment report of the Intergovernmental Panel on Climate Change. Technical report, Intergovernmental Panel on Climate Change, 2007.

[2] A.R. Ravishankara, J.S. Daniel, and R.W. Portmann. Nitrous oxide (N_2O): The dominant ozone-depleting substance emitted in the 21st century. *SCIENCE*, 326:123–125, October 2009.

[3] J. Pérez-Ramírez, F. Kapteijn, K. Schöffel, and J. A. Moulijn. Formation and control of N_2O in nitric acid production: Where do we stand today? *Applied Catalysis, B: Environmental*, 44:117–151, 2003.

[4] Mary Howe-Grant, editor. *Kirk-Othmer Encyclopedia of chemical technology*. 4th edition.

[5] D. Waller. Yara´s 51-y de-N_2O catalyst. DECHEMA, Frankfurt, Germany, 04.06.2008.

[6] Umicore Platinum Engineered Materials. Mks: Low & medium pressure converters. http://www.pem.umicore.com/en/03_ChemicalIndustries/03_ProductPortfolio/01_MKS/00_MKS.htm. Visited 24.09.2012.

[7] E .Fareid, G. Kongshaug, L. Hjornevik, and O. Nirisen. Ep0359286, 1990.

[8] Helmut Knözinger and Karl Kochloefl. *Heterogeneous Catalysis and Solid Catalysts*. Wiley-VCH, 2005.

[9] Peter Atkins and Julie de Paula. *Atkins' Physical Chemistry*. Oxford University Press, 7th edition, 2002.

[10] Gerhard Ertl, Helmut Knözinger, Ferdi Schüth, and Jens Weitkamp, editors. *Handbook of Heterogeneous Catalysis*. Wiley-VCH, 2nd edition, 2008.

[11] H.S. Taylor. A theory of the catalytic surface. *Proceedings of the Royal Society of London series A*, 108(745):105–111, May 1925.

[12] P.G. Menon and T.S.R. Presada Rao. Surface enrichment in catalysis. *Catalysis Reviews - Science and Engineering*, 20(1):97–120, 1979.

[13] G.J. Hutchings. Promotion in heterogeneous catalysis: a topic requiring a new approach? *Catalysis letters*, 75(1-2):1–12, 2001.

[14] David Waller. Protective barrier coatings between catalysts and ceramic support structures. Project description for master thesis, 2011.

[15] ECVV. Ceramic honeycomb. `http://www.ecvv.com/product/1041672.html`. Visited 24.09.2012.

[16] ECVV. Ceramic foam filter. `http://www.ecvv.com/product/1041668.html`. Visited 24.09.2012.

[17] C.N Hinshelwood and R.E. Burk. The homogeneous decomposition of nitrous oxide. *Proceedings of the Royal Society of London series A*, 106:284–291, 1924.

[18] C.N. Hinshelwood and C.R. Prichard. A comparison between the homogenous thermal decomposition of nitrous oxide and its heterogeneous catalytic decomposition on the surface of platinum. *Journal of Chemical Society*, 127:327–336, 1925.

[19] C.N. Hinshelwood and C.R. Prichard. The catalytic decomposition of nitrous oxide on the surface of gold: a comparison with the homogeneous reaction. *Proceedings of the Royal Society of London series A*, 108:211–215, 1925.

[20] F. Kapteijn, J. Rodriguez-Mirasol, and J.A. Moulijn. Heterogeneous catalytic decomposition of nitrous oxide. *Applied Catalysis, B: Environmental*, 9:25–64, 1996.

[21] E.R.S. Winter. Decomposition of nitrous oxide on rare-earth sesquioxides and related oxides. *Journal of Catalysis*, 15:144–152, 1969.

[22] E.R.S. Winter. Decomposition of nitrous oxide on metallic oxides. Part II. *Journal of Catalysis*, 19:32–40, 1970.

[23] E.R.S. Winter. Decomposition of N_2O on oxide catalysts. III: The effect of O_2. *Journal of Catalysis*, 34:431–439, 1974.

[24] E.R.S. Winter. Catalytic decomposition of nitric-oxide by metallic oxides. II: The effect of oxygen. *Journal of Catalysis*, 34:440–444, 1974.

[25] T. Yamashita and A. Vannice. N_2O decomposition over manganese oxides. *Journal of Catalysis*, 161:254–262, 1996.

[26] R.M. Dell, F.S. Stone, and P.F. Tiley. The decomposition of nitrous oxide on cuprous oxide and other oxide catalysts. *Transactions of the Faraday society*, 49:201–209, 1953.

[27] C.B. Amphlett. The catalytic decomposition of nitrous oxide in a large excess of oxygen. *Transactions of the Faraday society*, 50:273–278, 1954.

[28] A. Cimino, R. Bosco, and V. Indovina. Decomposition of nitrous oxide upon nickel oxide-magnesium oxide solid solutions. *Journal of Catalysis*, 5:271–278, 1966.

[29] A. Cimino, V. Indovina, and F. Pepe. Catalytic activity of nickel ions in magnesium oxide for decomposition of nitrous oxide. *Journal of Catalysis*, 14:49–54, 1969.

[30] A. G. Keenan and R. D. Iyengar. Decomposition of nitrous oxide on chromia-alumina catalysts. *Journal of Catalysis*, 5:301–306, 1966.

[31] A. Cimino and F. Pepe. Activity of cobalt ions dispersed in magnesium-oxide for decomposition of nitrous-oxide. *Journal of Catalysis*, 25:362–377, 1972.

[32] T. A. Egerton, F. S. Stone, and J. C. Vickerma. α-Cr_2O_3-Al_2O_3 solid-solutions. II: The catalytic decomposition of nitrous-oxide. *Journal of Catalysis*, 33:307–315, 1974.

[33] T. A. Egerton, F. S. Stone, and J. C. Vickerma. α-Cr_2O_3-Al_2O_3 solid-solutions. I: Formation and stability of adsorbed oxygen. *Journal of Catalysis*, 33:299–306, 1974.

[34] A. Cimino and V. Indovina. Acitity of Mn^{3+} and Mn^{4+} ions dispersed in MgO for N_2O decomposition. *Journal of Catalysis*, 17:54–70, 1970.

[35] L.G. Tejuca, J.L.G. Fierro, and J.M.D. Tascon. Structure and reactivity of perovskite-type oxides. *Advances in catalysis*, 36:237 – 328, 1989.

[36] T. Nitadori, T. Ichiki, and M. Misono. Catalytic properties of perovskite-type mixed oxides (ABO_3) consiting of rare earth and 3d transition metals. The roles of A- and B-site ions. *Bulletin of the Chemical Society of Japan*, 61:621–626, 1988.

[37] J. Wang, H. Yasuda, K. Inmaru, and M. Misono. Catalytic decomposition of dinitrogen oxide over perovskite-related mixed oxides. *Bulletin of the chemical society of Japan*, 68:1226–1231, 1995.

[38] R.S. Drago, K. Jurczyk, and N. Kob. Catalyzed decomposition of N_2O on metal oxide supports. *Applied Catalysis, B: Environmental*, 13:69–79, 1997.

[39] S. Tuti, F. Pepe, D. Pietrogiacomi, and V. Indovina. Decomposition of nitrous oxide on CoO_x/ZrO_2, CuO_x/ZrO_2 and FeO_x/ZrO_2 catalysts. *Reaction Kinetics and Catalysis Letters*, 72:35–42, 2001.

[40] G. Centi, G. Cerrato, S. D'Angelo, U. Finardi, E. Giamello, C. Morterra, and S. Perathoner. Catalytic behavior and nature of active sites in copper-on-zirconia catalysts for the decomposition of N_2O. *Catalysis Today*, 27:265–270, 1996.

[41] H.C. Zeng, J. Lin, W.K. Teo, J.C. Wu, and K.L. Tan. Monoclinic ZrO_2 and its supported materials $Co/Ni/ZrO_2$ for N_2O decomposition. *Journal of Materials Research*, 10:545–552, 1995.

[42] Z. Liu, M.D. Amiridis, and Y. Chen. Characterization of CuO supported on tetragonal ZrO_2 catalysts for N_2O decomposition to N_2. *Journal of Physical Chemistry*, 109:1251–1255, 2005.

[43] M. Lo Jacono, M. Schiavello, and A. Cimino. Structural, magnetic and optical properties of nickel oxide supported on η-aluminas and γ-aluminas. *Journal of Physical Chemistry*, 75:1044–&, 1971.

[44] M. Lo Jacono, A. Cimino, and G.C.A. Schuit. Magnetic and spectroscopic investigations of cobalt-alumina and cobalt-molybdenum alumina. *Gazzetta Chimica Italiana*, 103:1281–1295, 1973.

[45] M. Lo Jacono, M. Schiavello, D. Cordischi, and G. Mercati. Characterization of manganese ions supported on aluminas and their catalytic activity for N_2O decomposition. *Gazzetta Chimica Italiana*, 105:1165–1176, 1975.

[46] V.A. Sadykov, L.A. Isupova, I.A. Zolotarskii, L.N. Bobrova, A.S. Noskov, V.N. Parmon, E.A. Brushtein, T.V. Telyatnikova, V.I. Chernyshev, and V.V. Lunin. Oxide catalysts for ammonia oxidation in nitric acid production: Properties and perspectives. *Applied Catalysis, A: General*, 204:59–87, 2000.

[47] Ø. Nirisen, K. Schöffel, D. Waller, and D. Øvrebø. US20110110835 A9, 2011.

[48] D. Waller. Preparation of oxide-based catalyst active phases. 2012.

[49] Ian M. Campbell. *Catalysis at surfaces*. Chapman and Hall Ltd, 1988.

[50] Ulrich Schubert and Nicola Hüssing. *Synthesis of Inorganic Materials*. Wiley-VCH, 2nd edition, 2005.

[51] Martin Lok. *Synthesis of Solid Catalysts*. Wiley-VCH, 2009.

[52] A.C. Pierre and G.M. Pajonk. Chemistry of aerogels and their application. *Chemical Reviews*, 102:4243–4266, 2002.

[53] Finn Knut Hansen. Lecture notes KJM5500: Surface and nano chemistry. 2012.

[54] Stian Svelle. Lecture notes KJM5500: Surface and nano chemistry. 2012.

[55] Richard Tilley. *Understanding Solids - The Science of Materials*. WILEY, 2010.

[56] David B. Williams and C. Barry Carter. *Transmission Electron Microscopy*. Springer, 2nd edition, 2009.

[57] Arne Olsen. The theory and practice of analytical electron microscopy in materials science. 2008.

[58] Y.V. Golikov. Phase diagram of the Co-Mn-O system. *Inorganic Materials*, 24:975–979, 1988.

[59] R.D. Shannon and C.T.Prewitt. Effective ionic radii in oxides and fluorides. *Acta Crystallographica. Section B, Structural Crystallography and Crystal Chemistry*, 25:925–946, 1969.

[60] A.J.C. Wilson and E.Prince, editors. *International Tables for Crystallography, Volume C: Mathematical, Physical and Chemical Tables*. Kluwer Academic Publishers, 2nd edition, 1999.

[61] R.D. Shannon. Revised effective ionic radii and systematic studies of interatomic distances in halides and chalcogenides. *Acta Crystallographica. Section A, Crystal Physics, Diffraction, Theoretical and General Crystallography*, 32:751–767, 1976.

[62] Praewpilin Kangvansura. Effects of preparations: the Pechini, Schiff Base complex and coprecipitation on structure and properties of $LaCoO_3$ perovskite oxidative catalyst. Master's thesis, Kasetsart University, 2007.

[63] J.A. Moulijn, A.E. van Diepen, and F. Kapteijn. Catalyst deactivation: Is it predictable? What do we do? *Applied Catalysis, A: General*, 212:3–16, 2001.

[64] D. Waller. Personal correspondance, February 2013.

[65] James S. Reed. *Principles of ceramic processing*. Wiley Interscience, 2nd edition, 1995.

[66] X. Liu and C.T. Prewitt. High-temperature X-ray diffraction study of Co_3O_4: Transition from normal to disordered spinel. *Physics and Chemistry of Minerals*, 17:168–172, 1990.

[67] J.L. Gautier, S. Barbato, and J. Brenet. Ionic repartition in the manganese cobaltite. *Comptes Rendus de l'Academie des Sciences. Serie II*, 294:427–430, 1982.

[68] J.A. Alonso, M.J. Martinez-Lope, M.T. Casais, J.L. MacManus-Driscoll, P.S.I.P.N. de Silva, L.F. Cohen, and M.T. Fernandez-Diaz. Non-stoichiometry, structural defects and properties of LaMnO$_3$+delta with high delta values (0.1<=delta<=0.29). *Journal of Materials Chemistry*, 7:2139–2144, 1997.

[69] M. Gasperin, M.C. Saine, A. Kahn, F. LaVille, and A.M. Lejus. Influence of M^{2+} ions substitution on the structure of lanthanum hexaaluminates with megneto-plumbite structure. *Journal of Solid State Chemistry*, 54:61–69, 1984.

[70] S.A. Fedulov, Y.N. Venevtsev, and D.F. Dzhmukhadze. *Krystallografiya*, page 408, 1962.

[71] H. Taguchi, S.I. Matsu-ura, M. Nagao, and H. Kido. Electrical properties of perovskite-type La(Cr$_{1-x}$Mn$_x$)O$_{3+d}$. *Physica B: Condensed Matter (Amsterdam, Netherlands)*, 270:325–331, 1999.

[72] Therese Stokkan. Structural investigation of a Ni-Nb-O phase by electron diffraction. Master's thesis, University of Oslo, 2011.

[73] The Landolt-Bornstein Database. Surface free energy and surface stress. `http://www.springermaterials.com/docs/pdf/10783464_10.html`. Visited 3.6.2013.

[74] G. B. J. de Boer, C. de Weerd, D. Thoenes, and H. W. J. Goossens. Laser diffraction spectrometry: Fraunhofer diffraction versus Mie scattering. *Particle & Particle Systems Characterization*, 4:14–19, 1987.

[75] Malvern. Using Mie theory and the Fraunhofer approximation. `http://www.malvern.com/labeng/technology/laser_diffraction/mie_theory_fraunhofer.htm`. Visited 11.05.2013.

[76] H. Y. T. Chen, W. C. J. Wei, K. C. Hsu, and C.S. Chen. Adsorption of PAA on the α-Al$_2$O$_3$ surface. *Journal of American Ceramic Society*, 90:1709–1716, 2007.